Semiconductor Quantum Dots: Intraband Electronic, Optical and Carrier Dynamical Properties

PhD Thesis

The University of Leeds
School of Electronic and Electrical Engineering
&
Institute of Microwaves and Photonics

Nikola Prodanović MSc

January 2014

*Supervised by:
Dr. Dragan Indjin, Prof. Paul Harrison and Dr. Zoran Ikonić*

Acknowledgments

I would like to gratefully acknowledge the excellent supervision of Dr Dragan Indjin, Dr Zoran Ikonić and Professor Paul Harrison. Without them, my PhD work would be impossible as they stood as the constant support during the entire period of my PhD studies from application for funding to the process of writing and submission of this thesis. Their academic support and advices were of great importance enabling me to overcome all obstacles I encountered in reading the literature, writing publications and presentations and solving the cutting edge scientific issues regarding the physics of semiconductor nanostructures. Special thanks to Dr Dragan Indjin and Dr Zoran Ikonic and their families for making me feel like I am at home and providing me valuable friendships.

The work presented in this thesis would be impossible without the strong theoretical background in physics, mathematics and programming. I am grateful to all my teachers from Faculty of Physics and Faculty of Electrical Engineering, University of Belgrade. Special thanks to Professor Vitomir Milanović, Faculty of Electrical Engineering, who encouraged me to pursue a PhD in the field of nanostructures at Leeds and who collaborated with us on the work regarding the bound states in the continuum in quantum rods.

Thanks to Dr Nenad Vukmirovic, Institute of Physics, University of Belgrade who provided me detailed insight in the electronic, optical and transport properties calculations methods for semiconductor nanostructures. Thanks to Dr Vukmirovic are also due to collaboration with us on work regarding the electronic and optical properties of quantum rods and transport properties of colloidal quantum dot supercrystals. For latter, Dr Vuk-

Abstract

Brief fabricational and applications surveys on semiconductor quantum dots and the subsequent motivation for further development of theoretical modeling are presented. In order to study the electronic structure of quantum dots, $\mathbf{k} \cdot \mathbf{p}$ models are introduced. Both the 8 band $\mathbf{k} \cdot \mathbf{p}$ model and the effective mass model were used in order to study electronic structure of quantum rods. Existence of bound state in continuum in quantum rods is demonstrated. The vibrational structure and electron–phonon interaction in semiconductor quantum dots was studied via bulk models for self assembled quantum dots and continuum models for colloidal quantum dots. The concept of polarons due to very strong electron–longitudinal optical phonon interaction was demonstrated for single self assembled quantum dot and for supercrystal of colloidal quantum dots. Lattice anharmonicity is also considered as a main mechanism enabling the non-radiative relaxation process of the polarons in self assembled quantum dots.

Optical properties of such 3D confinement structures are modeled using dipole Hamiltonian approximation and properly incorporated into $\mathbf{k} \cdot \mathbf{p}$ model formalism within the framework of linear response theory. Radiative and non-radiative lifetimes in self assembled quantum dots were studied and correlation between them was established.

Transport properties of colloidal quantum dot supercrystals were also studied within the framework of linear response theory. Variational polaron theory is introduced in order to examine formation of polarons dependent on temperature, interdot coupling strength and strengths of electron–phonon interactions. It was found that small polaron formation occurs at room tem-

perature for possible interdot couplings. It was also found that small polaron formation narrows the bands and localizes the carriers inside each dot in the supercrystal. Available experimental data on the issue were discussed by using the results of the model.

Contents

Publications Related to the Thesis

Journal Publications

Papers in Peer Reviewed Journals

1. N. Prodanovic, N. Vukmirovic, Z. Ikonic, P. Harrison and D. Indjin, Importance of Polaronic Effects for Charge Transport in CdSe Quantum Dot Solids, Journal of Physical Chemistry Letters, 5, p. 1335, 2014.

2. N. Prodanovic, V. Milanovic, Z. Ikonic, D. Indjin and P. Harrison, Bound states in continuum: Quantum dots in a quantum well, Physics Letters A, 377, p. 2177, 2013.

3. N. Prodanovic, Z. Ikonic, D. Indjin and P. Harrison, Relationship between electron-LO phonon and electron-light interaction in quantum dots, Physical Review B, 85, p. 195435, 2012.

4. N. Prodanovic, N. Vukmirovic, D. Indjin, Z. Ikonic, P. Harrison, Electronic states and intraband terahertz optical transitions in InGaAs quantum rods, Journal of Applied Physics, 111, p. 073110, 2012.

Papers in Conference Proceedings Issues of Peer Reviewed Journals

1. N. Prodanovic, Z. Ikonic, D. Indjin, P. Harrison, Electron-LO phonon and electron-photon interactions analogy in semiconductor quantum dots, Journal of Physics: Conference Series, 367, p. 012008, 2012, preceded by poster presentation on TMCS III Conference, Leeds(UK), 2012 and published through regular peer reviewing process.

2. N. Prodanovic, N. Vukmirovic, D. Indjin, Z. Ikonic, P. Harrison, Theoretical modeling of InGaAs quantum rods: Terahertz intraband absorption and its dependence on rod height, Journal of Physics: Conference Series, 242, p. 012012, 2010, preceded by poster presentation on TMCS II Conference, York(UK), 2010 and published through regular peer reviewing process.

Conference Poster Presentations

1. N. Prodanovic, Z. Ikonic, D. Indjin, P. Harrison, Tailoring of Intraband Luminescence and Lifetime properties of Quantum Dots, QD2012 Quantum dot Conference, Santa Fe (New Mexico), Book of Abstract M 76, 2012.

2. N. Prodanovic, N. Vukmirovic, D. Indjin, Z. Ikonic and P. Harrison, Intraband optical properties of self-assembled InGaAs quantum rods and its dependence on rod height, ITQW Conference, Badesi(Sardinia, Italy), 2011

3. N. Prodanovic, N. Vukmirovic, D. Indjin, Z. Ikonic, P. Harrison, Intraband optical properties of self-assembled columnar quantum dots,

QD2010 Quantum dot Conference, Nottingham (UK), 2010.

List of Commonly Used Symbols

e_0	Electronic charge
E	Energy
E_F	Fermi energy
E_G	Band gap energy
E_i, E_f, E_m, E_n	Energy of the stationary electronic state
n_i, n_f	electron population corresponding to Fermi-Dirac distribution
ϵ_0	Permitivitty of vacuum
ϵ_r	relative permitivitty
$\boldsymbol{E}$	Electric field
h	Plank's constant over 2π
$\boldsymbol{k}, \boldsymbol{q}$	Wave vectors of electron, photon or phonon
k_B	Boltzmann's constant
T	Temperature
β	$\frac{1}{k_B T}$

m^* Effective mass

m_0 Free electron mass

t Time (variable)

x, y, z Cartesian co-ordinates

x_μ, x_ν, x_i, x_j Cartesian co-ordinates

p_μ, p_ν, p_i, p_j Cartesian momentum components

ω Frequency of phonon or photon

List of Principal Abbreviations

SAQD	Self Assembled Quantum Dots
CQD	Colloidal Quantum Dots
MBE	Molecular Beam Epitaxy
MOCVD	Metalorganic Chemical Vapour Deposition
QD	Quantum Dot
QCL	Quantum Cascade Laser
QDIP	Quantum Dot Infrared Photodetector
LO	Longitudinal Optical
LA	Longitudinal Acoustic
NC	Nanocrystal
NS	Nanocrystal Solid (CQD Supercrystal)
FCF	Fröhlich Coupling Function

List of Figures

List of Tables

Chapter 1

Introduction

1.1 Semiconductor Quantum Dots

In recent decades significant progress has been made in the fabrication of
semiconductor dot structures with carrier band confinement in all three
spatial directions based on III-V and II-VI compounds. These technological
breakthroughs enabled new fields of fundamental solid state physics and
many new technological fields relating applications of these structures.

There are three well defined technological means for fabrication of quan-
tum dots and consequently three big different groups of quantum dots.
Those are self-assembled quantum dots, colloidal nanocrystals and electro-
statically defined quantum dots. The main focus of this thesis will be on
the former two groups.

1.2 Fabrication Technology

1.2.1 Basic Fabrication Methods

The most prominent nano-size heterostructures are self-assembled quantum dots(SAQD) grown by a well established technological procedure called Stranski-Krastanov growth. Stranski-Krastanov growth consists of heterostructural epitaxy between materials with different lattice constants. During the growth of a layer of one material on a top of another, the formation of nanoscale islands takes place [8] due to lattice constant mismatch (see Fiq. 1.1). This effect takes place if the width of the layer (so called wetting layer) is larger than a certain critical thickness. Two mostly used experimental techniques for epitaxial nanostructure growth are Molecular Beam Epitaxy (MBE) and Metalorganic Chemical Vapour Deposition (MOCVD) [9, 10].

InAs/GaAs SAQDs will be of the important interest in this thesis. Such quantum dots are composed of GaAs bulk-like matrix which completely surrounds an InAs island with optional additional Ga content in the island. The zincblende crystal structure of the entire structure remains approximately valid. The crystal sites of In-rich island stretch a bit forming the strain field, but coherent crystal structure with the low level of defect remains. This effectively means that SAQD is still condensed matter system, but with the inhomogeneous distribution of band edges in space. InAs conduction band is lower in energy then of surrounding GaAs bulk matrix, while the opposite holds for valence band offset. As a result, this composition acts as a confining potential for electrons in the conduction band and holes in the valence band due to lower energetic position of conduction and valence band for electrons and holes respectively in the dot material, i.e. InAs in compar-

ing with surrounding material, i.e. GaAs. The fact that quasi-free carriers in bulk GaAs are now confined in all directions in space to several tens of nanometers, causes their quantized behavior, i.e. formation of discrete energy spectrum states below energy barrier of the dot. It is worth mentioning that above the effective energy barrier, occurance of free bulk states takes place and carriers "captured" by the dot confinement can be "ionized" into the continuum.
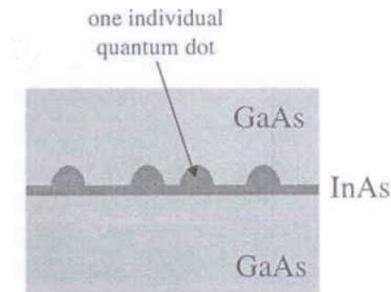
Figure 1.1: Schematic figure of SAQDs. InAs islands reside on the In-rich wetting layer surrounded by GaAs bulk.

Beside SAQDs fabricated by sophisticated deposition process, it is possible to synthesize quantum dots by crystal nucleation in colloidal solutions. The dots obtained this way are called colloidal nanocrystals(CN) or colloidal quantum dots(CQD) [11, 12].

The synthesis of CQDs takes place in three-component solutions composed of organic surfactants, precursors, and solvents. Precursor compounds contain material for dot nucleation. Solution medium is heated to a sufficiently high temperature, when the precursors chemically transform into monomers. Nucleation takes place when monomers reach a high enough supersaturation level and the nanocrystal growth starts. The temperature is a very sensitive parameter of nucleation process and must be high enough to allow for rearrangement and annealing of atoms while being low enough

to allow crystal growth. Monomer concentration is also a very sensitive parameter. High enough monomer concentration enables relatively small critical size (the size where nanocrystals neither grow nor shrink) resulting in even growth of nearly all particles. In this regime, smaller particles grow faster than large ones (since larger crystals need more atoms to grow than small crystals) and thus size monodispersivity can be obtained. When the monomer concentration is depleted during growth, the critical size becomes larger than the average size present and nucleation becomes very inhomogeneous.

Typical CQDs are made of binary alloys such as CdSe, CdS, InAs, and InP or ternary alloys such as $CdSe_xS_{1-x}$. These quantum dots can contain as few as 100 to 100,000 atoms within the quantum dot volume, with a diameter of 2 to 10 nanometers. These nanocrystals usually reside within the insulating dielectric matrix giving the full confinement to the carriers inside.
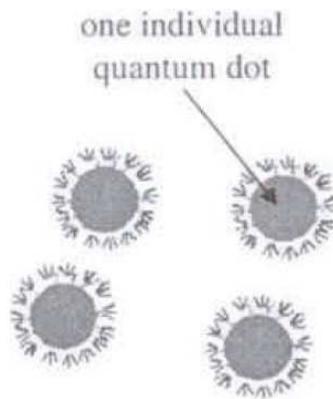
Figure 1.2: Schematic figure of CQDs. Each nanocrystal is usually of the spherical shape and is surrounded by the ligands, which play role of linker molecules enabling the electronic coupling between the two adjacent dots.

Finally, another group of quantum dots, which will not be considered

in this thesis, is introduced. One can fabricate quantum dots by additional confinement to the two dimensional electron gas in specific semiconductor heterostructure. This additional confinement can be done laterally by electrostatic gates, or vertically by etching techniques [13, 14] (see Figs. 1.3 and 1.4). By changing the applied potential at gates or by applying external magnetic field it is possible to change the properties of this type of quantum dots, sometimes termed as electrostatic quantum dots. These quantum dots are known so far as the best candidates for practical realization of quantum qubits [15, 16, 17]. Qubits are based on the spins of two electrons in two coupled electrostatically defined quantum dots. Coupling between these two dots is tuned by gating and thus spins of two separated electrons can interact via tunable exchange interaction.
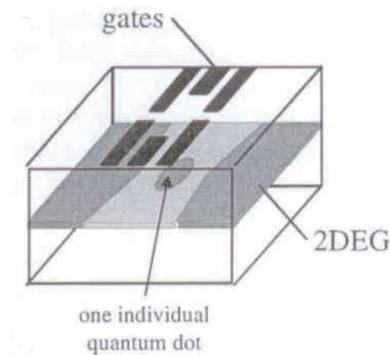
Figure 1.3: Schematic figure of the electrostatically defined quantum dot by the gating technique. The basis of this structure is the 2D electron gas confined in the growth direction. Additional confinement in the lateral directions is reached by the electrostatical gating.

1.2.2   Fabrication Modifications

Regarding the motivation side of the work done in this thesis, crucial question can arise "Why is it important to theoretically study quantum dots"? Indeed, if quantum dots were heterostructures with extremely variational
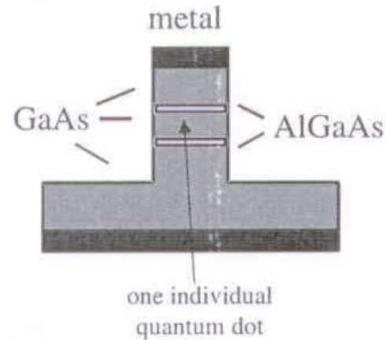
Figure 1.4: Schematic figure of the electrostatically defined quantum dot where the additional lateral confinement for 2D electron gas is obtained by the physical etching of the structure .

and uncontrollable fabricational outcome then it would be pointless to put so much effort in their theoretical modeling. If it was possible to control and modify the outcome of their growth then the great space for their modeling and engineering would be created, thus justifying theoretical study effort.

Basic fabrication processes of quantum dots has been briefly presented in section 1.2.1. In the last decade, several modifications of these growth processes emerged leading to various types of self assembled and colloidal nanocrystals and certain level of their geometrical and compositional tunability. Some of the state of the art modifications based on SAQDs are following.

- **Post-growth annealing of SAQDs**

    After completed fabrication process it is possible to thermally anneal self-assembled quantum dots. Post growth annealing details are given in, e.g. [18, 19, 20]. The main result is diffusion of In into surrounding GaAs matrix and thus spatially increased, energetically reduced, graded and tunable confinement.

- **Quantum posts**

After forming of InAs islands on GaAs substrate which is regular step in fabrication of InAs/GaAs SAQDs [8] it is possible to deposite thin layers alternating superlattice of InAs and GaAs above it. Due to possible strain issues, In in the supperlatice diffuses above the In islands, thus forming In rich tubes above each self-assembled In island. The whole structure is then regularly capped with GaAs matrix and overall outcome is quantum rod structure, i.e. elongated quantum dot. Details of fabrication are given in [1, 21, 22]. By controlling the growth parameters, thickness of layers in superlattice, and their rate, it is possible to precisely tune In content in the tube and its height. Additional growth control by using different arsenic sources has been reported as well[23, 24].

Figure 1.5: TEM image of quantum rods normal to growth direction. Image taken from Ref. 1.

- **Quantum rings**

  Quantum rings are also derived from SAQDs. Starting from self-organized InAs dots, the crucial step for the ring formation is a short annealing phase after the dots have been covered by a thin GaAs layer [25, 26]. Confinement in this nanostrucutures is stronger than that in dots because of their altered shape. It has been recently shown [27] that these structures can exhibit very good intraband detecting properties.

- **Growth-kinetics control**

  By changing the growth kinetics during the capping of InAs islands with GaAs, it is possible to tune the dimensions of InAs self-assembled quantum dots. One has to modify the growth sequence during the capping of InAs islands in order to tune the thickness and lateral dimensions of the quantum dots while keeping the wetting layer thickness constant [28].

Some modified and more complex structures based on CQDs are following

- **Core-shell CQDs**

  In order to passivate the surface states in conventional CQDs one can apply the approach where additional layer of the same type, but distinct semiconductors can be grown spherically around the initial CQD. In such a way, so called core-shell CQDs can be fabricated. Those nanostrucures have better luminescence properties [29] since surface states responsible for decoherence and non-radiative recombinations are removed. Depending on the band gap ratio of core and shell material these structures are divided in two types. In type 1 structures the conduction (valence) band edge in the core is below (above) the values in the shell, so the core tends to confine both electrons and holes. In type 2 alignment only one of the two types of carriers is confined to the core.

- **CQD supercrystal**

  It is possible to arrange CQDs in superlattice formation in self-assembled manner during nucleation process. [30, 31] With previously explained

monodispersivity in Sec. 1.2.1 it is possible to create artificial solids with sites consisted of CQDs. In order to obtain good transport properties of these supercrystals, three main directions in technology development are fabrication of monodispersed systems, enhanced interdot coupling and uniform high level doping. Even though technology went far in development, great challenge still remains in obtaining the CQD supercrystal with satisfying geometrical monodispersivity and interdot coupling [32].
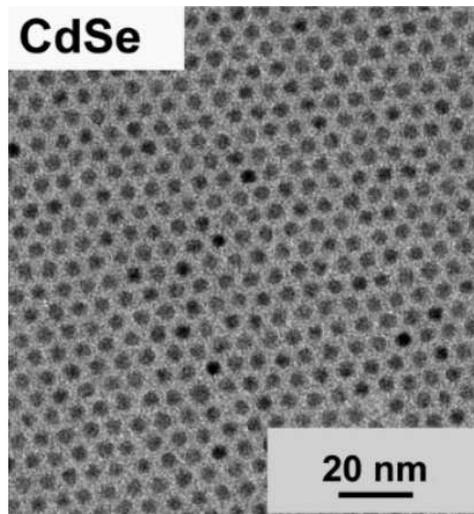
Figure 1.6: TEM image of CdSe CQD supercrystals. Image taken from Ref. 2.

1.3 The Nature of Carriers in Quantum Dots

Carriers in any condensed matter system define optoelectronic properties of such system. Quantum dots provide confinement for carriers in all three spatial dimensions giving rise to the atomic-like discrete spectrum. This can be very useful in optoelectronic applications since semiconductor technology is already very well developed while discreteness of the spectrum may pro-

vide very interesting features for possible optoelectronic applications. All optoelectronic applications are physically based on interaction of external electromagnetic field and charge carriers inside the considered system. The term "carrier" in quantum dots may refer to electrons, holes, excitons and even polarons as a carriers of charge. Undoped dot has all the electrons in valence band in thermodynamical equilibrium. Only few electrons from valence band can be thermally or optically excited providing electrons in conduction band and leaving holes in valence band. Electrons and holes act as carriers, but they also interact mutually by Coulomb forces forming excitons.

By suitable experimental setup, for example see Ref. 33 for SAQDs and Ref. 2 for CQDs, it is possible to dope quantum dots with controllable numbers of electrons in conduction band per dot. In this case, it is possible to induce conduction band transitions, i.e. intraband transitions in which only electrons are involved. In this manner, carriers are electrons, or if they interact strongly with phonons, polarons. Polaron is in some way complex particle consisting of phonons and electrons. Quantum mechanically it is described in the Hilbert space derived as the direct product of electron fermionic and phonon bosonic space.

The artificial atom picture of quantum dot spectrum is good only for explaining the "macroatom" effects in quantum dots. For many purposes such as dominant optical transitions, this analogy with atoms is very useful, but, as it will become apparent later in the thesis, a quantum dot is actually a genuine condensed matter system, with many interesting properties that are all ultimately related to the fact that we have a strong confinement in a crystalline matrix. In other words, one can also say that in quantum dots, the primary effect is a confining small volume effect, but most of the properties

of a quantum dots come from its crystalline nature. In particular, the latter is responsible for specific features in the optical characteristics of quantum dots as well. The most important consequence of its crystalline nature is that electrons and holes are strongly affected by interaction with phonons. Due to various types of interactions between electrons and phonons [34] carrier physics requires different picture than that of a simple atomic-like, and it is subject of state of the art research.

1.4 Applications

The applications of semiconductor quantum dots are manifold and difficult to account for, but still dividable in engineering applications on one hand and fundamental research applications on the other hand. Confinement properties of quantum dots resemble those of atoms and thus quantum dots are often called artificial atoms which provides the basis for variety of fundamental research regarding confined interacting fermions [35], their spin [16, 17], cavity electrodynamics [36] etc...

One of the most exciting aspects of quantum dot engineering application is the usage of the quantum dot state (spin state [15, 16, 17], exciton [37] or charged exciton) as a qubit in quantum information processing. Coherent control of an exciton state in a single dot selected from an ensemble of self-assembled quantum dots has been achieved [37]. This result appears promising, although the control of a larger number of quantum dot qubits is not feasible yet, mainly due to the difficulty of controlling qubit-qubit interactions.

Truly, the main application of quantum dots is in optoelectronics. Transitions of the carriers between discrete levels and discrete and continuum levels of quantum dots enable efficient absorption and emission of photons

together with possible bias controlled harvesting and thus provide excellent basis for utilizing the dots as active media in detecting and lasing operations.

1.4.1 Interband Optolelectronics of SAQDs

Interband radiative transition is absorption or emission of a photon which in return creates or annihilates an electron-hole pair(see Fig. 1.7). During the process, an electron changes its state between the valence and the conduction band. This effect exists in bulk semiconductor materials and was utilized extensively in the field of optoelectronics for operation of semiconductor emitting diodes, lasers, detectors and photovoltaics.

Up to date, the most important application of quantum dots is in quantum dot based interband lasers. The short research history on this very important subject follows.

The highest probability for radiative processes comes from the carriers near band edge. The confining effect of low dimensional heterostructures increases density of states near the band edge which gives the advantage to these structures in comparison to bulk materials [38]. The difference becomes more distinct at higher temperatures where carriers are thermally excited into energetically higher states, thus degrading the radiative transition probabilities [39]. The increased density of states near the band edge clearly suppresses this effect, and as a consequence, concentrates injected carriers near the bottom of the conduction band and the top of the valence band. Mentioned effect is fully exploited for the case of delta function density of states which occurs in quantum dots as full 3D confining structures. The influence of dimensionality on the threshold current was first studied by Arakawa and Sakaki [40] and later by Asada *et al.* [41]. They have predicted that its temperature sensitivity is much smaller for highly confined
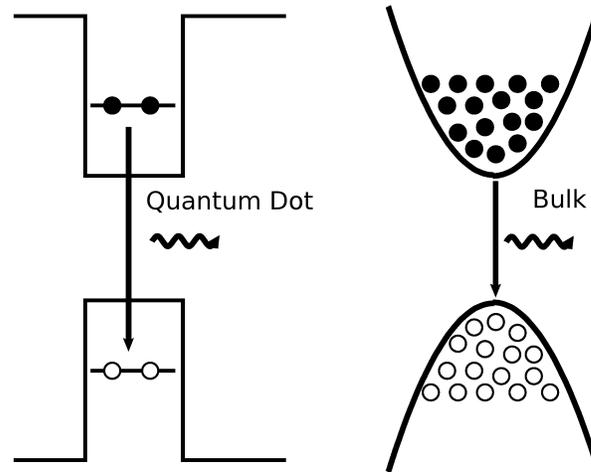
Figure 1.7: Schematic figure of the interband transitions in the semiconductor nanostructures. Dominant transitions in quantum dots (left Figure) are between bound states with discrete spectrum whereas dominant transitions in quantum wells (right Figure) are between quasibound states with continuum spectrum.

structures and is nearly temperature independent in the case of three dimensionally confined structures - quantum dots. These predictions were confirmed experimentally by placing a quantum well laser in a magnetic field [42], mimicking the effect of additional quantum confinement. Finally, discovery of Stranski-Krastanov growth mode enabled fabrication of high density ensembles of relatively uniform quantum dots, with low defect densities and consequently led to the demonstration of interband quantum dot lasers [43].

Beside laser devices, other interesting interband transitions based devices are optical amplifiers [44] and single photons emitters for quantum cryptography [45].

1.4.2 Intraband Optoelectronics of SAQDs

In order to access longer wavelengths, one has to use transitions within the same band. These transitions are called intraband transitions. Low dimensional nanostructures exhibit intraband transitions which makes them advantageous in comparison to bulk semiconductor materials. Therefore, in the last two decades, semiconductor nanostructures, such as quantum wells, wires and dots have been recognized as sources and detectors of electromagnetic radiation in the mid- and far-infrared region of the spectrum [46, 47, 48]. Many applications arise by using this far-infrared and
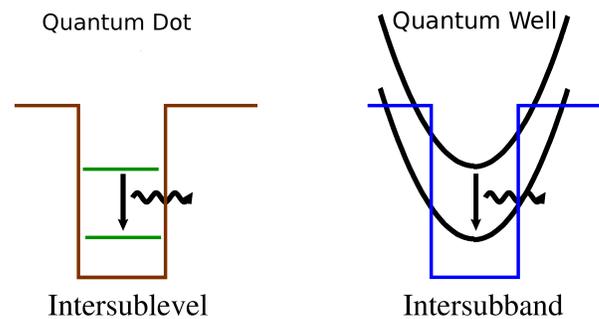
Figure 1.8: Intraband transitions in quantum dots (left Figure) and quantum wells (right Figure). Transitions in quantum dots are between fully descrete states. Transitions in quantum wells are between subbands, most prominently between band edges of the subbands.

terahertz part of the radiation spectrum. Atmosphere is transparent for electromagnetic radiation at two atmospheric windows, namely at $3 - 5\mu$m and $8 - 13\mu$m. These atmospheric windows enable space optical communications, remote sensing and detection. Vibrational modes of many molecular compounds in the $3 - 17\mu$m part of the spectrum enable their detection. This can be used in order to measure pollution, monitor industrial processes, de-

tect hidden explosives [49]. Vast numbers of entities like the human body are very emissive in terahertz region which can be utilized in night vision technologies. Engineering areas of medical imaging, astronomy and food quality control [50] can also utilize devices for efficient terahertz detection.

One dimensional confinement based systems, such as quantum cascade lasers (QCL), are, up to now, most advanced systems used as active media for devices based on intraband transitions. Regarding the quantum dots, significant progress has been made in their utilization in quantum dot infra-red photodetectors (QDIPs). QDIPs comprising III-As self-assembled quantum dots have become a very important technology for the detection of mid- and far-infrared electromagnetic radiation [51].

Unfortunately, intraband emission in quantum dots has not been accessed in the desired strength. Up to now, the devices based on quantum wells still exhibit best performance [52]. The main obstacle in operation of quantum well-based emitters is electron-phonon interaction which destroys both coherence and population inversion during the operation on higher temperatures. Quantum well subbands allow reduced, but still continual density of states which increases the effect of the electron-phonon interaction. On the other hand, higher temperature, up to 225 K, lasing operations were observed in quantum well based QCLs in strong magnetic fields [53, 42]. This was understood as experimental evidence that a system with truly discrete states should have a lower threshold current as magnetic field converts intersubband states into discrete Landau states. From the commercial point of view it is necessary to avoid the use of high magnetic fields because of extremely bulky and expensive setup and have a system with truly discrete states. Examination of SAQDs as potential candidates for effective intraband lasing will be done in this thesis.

Firstly, it was thought that due to the discrete nature of the electronic structure and the nearly constant energy of LO phonons, the so-called phonon-bottleneck would occur [54] providing long non-radiative lifetimes important for obtaining the population inversion. However, a great amount of experimental data showed the absence of this effect [55, 56]. Non-radiative lifetime in QDs is still higher than in conventional QCLs.

Magneto-optical experiments in [57, 58] showed that QDs behave like complex condensed matter systems where electrons and phonons interact strongly via polar Fröhlich coupling, thus forming quasiparticles, so-called polarons. Therefore, the simple picture of weak electron–phonon interaction was not appropriate [59, 60].

The most prominent theoretical justification for a short lifetime of excited carriers in QDs has been presented in [56, 61], where the lattice anharmonicity perturbation enables the energy exchange between different polaron modes, thus enabling relaxation towards the thermodynamical equilibrium. In other words, polarons decay due to relatively fast LO phonon decay [62, 33] and relaxation times of the order of hundred of picoseconds were reported [63, 55]. This is still two orders of magnitude larger than in quantum wells and hence several theoretical proposals were made for inter-sublevel quantum dot cascade laser. They are either 2-level systems utilizing the ground-first excited state transition for lasing [64, 65, 66, 67], or 3-level systems [68] with the lasing transition between higher excited states in the QDs.

Experimentally, lasing has not been observed yet, but there have been several reports on the observed intraband photoluminescence based on the s-p like transitions in the quantum dot cascades [69, 70, 71, 72]. Room temperature intraband photoluminescence was observed in Ref. 73. In [69, 71]

it was suggested that the dominant transition observed in the PL spectra is the transition between s-like and p-like states, which was based on numerical calculation of electronic states and optical matrix elements within the dipole approximation. This resonant s-p like transition requires a detailed investigation in terms of the radiative and non-radiative transition strengths. In order to obtain lasing, the strength of the radiative transition has to overcome population inversion losses due to non-radiative transitions. Therefore, the theoretical description of radiative and non-radiative relaxation processes is crucial, and it would be convenient to provide a theoretical insight which incorporates both, non-radiative and radiative transitions. This issue will be addressed in the fourth chapter of this thesis.

1.4.3 Optoelectronics of CQDs

Solution processing fabrication of CQDs described in Sec. 1.2.1 stands as relatively very cheap technology [2] and that fact casts CQDs in research focus regarding its optoelectronics applications. Beside cheap fabrication process, CQDs also exhibit enhanced luminescence due to descrete nature of carriers[74] and core-shell CQDs exhibit even better luminescence than conventonal CQDs [2].

Even though CQDs are very often used in fundamental research due to greater monodispersivity of dots when compared to SAQDs, technological applications acquire increasing interest of the scientific community in the last decade. CQD are reported as the basis for many potential optoelectronic devices such as light emitters, detectors, solar cells and electronic transistors.

Due to very good luminescence properties, light emitting diodes(LED) based on CQDs have been demonstrated [75, 76]. The architecture of CQD based LED consists of quantum dot thin film layer sandwiched between

two heavily doped layers called hole and electron transport layer. Metallic contacts are added on a top of each doped layer and current flows by tunneling through CQD layer where injection of electron-hole pairs occurs by capturing of tunneling pairs into confining potential of a CQD.

Efficent luminescence means efficient absorption and thus CQD can be utilized as the basis for the photodetecting device. Even more, CQD based on narrow bandgaps materials such as PbSe or InAs can be used in fabrication of photodetectors in infra-red region of spectrum. Up do now, infrared photodetectors are very expensive since silicon cannot support infra-red region and cheap colloidal processing technology opens new routs towards obtaining the cheap and effective infra-red photodetector devices. The most prominent architecture of such device [2, 77] consists of lithographically defined contacts on a top of semiconductor bulk and thin film layer of CQDs deposited between the contacts (see Fig. 1.9). Applications of CQDs as active mediums of photovoltaics devices has been reported as well [78] and this field undergoes extensive research activities. Many configurations containing all inorganic CQDs active mediums or hybrid active mediums with other materials such as polymer solar cells have been reported [2]. It is also believed that effect of increased carrier multiplication in CQDs can be utilized in these devices [79] which would significantly increase efficiencies of solar cells even above Shockley-Queisser limit [2]. Applications of CQDs in production of novel memory type devices has been reported as well [80]

The device architecture, similar to one presented for CQD-based photodetectors, can also be used for novel field effect transistor(FET) devices (see Fig. 1.9). Thin film of CQDs is deposited between two electrodes and third electrode can be added on top or bottom of the film parallel to it [81, 82, 2]. Up to now, the main issue regarding functionality of this
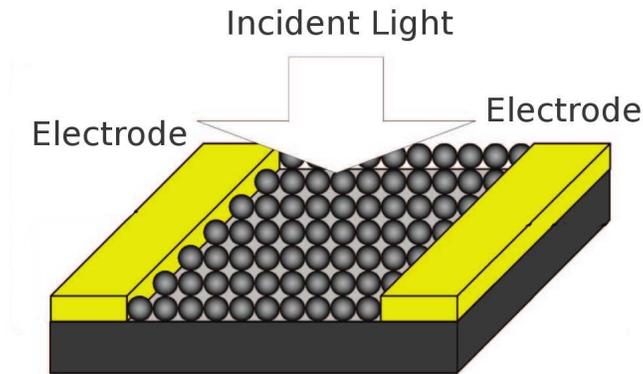
Figure 1.9: CQD-based photodetector. Thin film of CQDs is deposited on semiconductor substrate between two electrodes. Similar configuration holds for CQD-based field effect transistors with additional gating electrode put on top or bottom of presented configuration.

configuration is good electronic transport between the CQDs which is required for efficient operation of all these devices. This issue will be examined in this thesis as well and the main idea relies on the ability that thin CQD films can be fabricated in the form of supercrystals of CQDs as explained in Sec. 1.2.2. Initially, these structures exhibited very low conductivity, but increased interdot coupling by using shorter ligands and doping techniques enabled observable conductivity with corresponding mobility of the order of 10^{-2}cm^2/(Vs) (see Ref. 83). Conductivity in this configuration decreased with decreasing temperature indicating activated electron mobility. It was suggested [83] that Mott's variable range hopping [84, 85, 83, 32] is the transport mechanism at low temperatures in these disordered, doped and weakly coupled CdSe NCs.

A strong effort has been put in order to achieve higher electron mo-

bilities and band-like transport. In order to improve transport properties, three main directions in technology development are: fabrication of monodispersed systems, enhanced interdot coupling and uniform high level doping. Even though technology went far in development, great challenges still remain in obtaining the CQD supercrystals with satisfactory geometrical monodispersity and interdot coupling [32, 2]. Up to now, the upper limit of electron mobility has become of the order of ten $cm^2/(Vs)$ (Refs. 6, 7, 86). Such relatively high values of mobility and the decrease of mobility with increasing temperature, were considered as a signature of band transport in these materials.

Numerous effects act detrimentally when band transport in realistic NSs is concerned, such as the effects of disorder [32] (nanocrystal size nonuniformity, irregularities in the spatial arrangement, nonuniform doping, etc), traps and the electron-phonon interaction. While the effects of disorder and traps can be removed at least in principle by the fabrication of high-quality structures, the electron-phonon interaction is intrinsic to the material and cannot be removed. Despite this, very little is known about the strength of the electron-phonon interaction and its effect on transport properties in NSs. In an ideal NS, if the electron-phonon interaction in the NC were much weaker than electronic coupling between the NCs, the system would exhibit band transport where the electron-phonon interaction acts as a scattering mechanism that determines the value of the electron mobility. In the opposite limit, if the electron-phonon interaction were much stronger than the electronic coupling between the NCs, the formation of small polarons – quasiparticles consisting of an electron in the NC dressed by phonons – would take place. In that case, the electronic coupling between the NCs acts as a perturbation that allows small polarons to hop from one NC to

another and such a transport regime is called small polaron hopping. All these issues will be examined in detail in the last section of the thesis.

1.5 Thesis Outline

This thesis will concentrate on theoretical modeling of optoelectronic properties within the conduction band of quantum dots since there is large potential application ground to be utilized based upon it. Detailed physics of carriers has to be determined in order to achieve, at least theoretically, main quantities regarding intraband physics, such as carrier radiative lifetimes, coherence lifetimes, non-radiative lifetimes, mobilities of carriers, etc... Theoretical knowledge of all physical processes in conduction band of quantum dots will provide information on practical feasibility of quantum dots as active media for a range of optoelectronic and electronic applications which require transport of carriers through conduction band or intraband radiative absorption or emission. Beside applications, studying of the intraband physics in quantum dots may contribute as well to fundamental knowledge regarding condensed matter physics.

When it comes to optoelectronic applications and experimental studies, electrons in conduction band are the most important particles in all condensed matter systems responsible for the interaction with THz and infrared radiation and for the conductivity of the system. They carry the charge which interacts with external electromagnetic field. Therefore, the second chapter of the thesis will be dedicated to the study of electronic quantum mechanical intraband spectra in quantum dots. Empirical methods for calculation of electronic structure based on envelope function formalism will be introduced. Few simple model examples will be presented in order to derive general conclusions on electronic structure of 3D confined structures

and it dependence on quantum dot geometrical parameters. The scientific contribution to the second chapter will be examination of the intraband electronic structure of quantum rods, novel heterostructures based on SAQDs. Motivation for that lies in ability to control certain geometrical and compositional parameters of quantum dots which was not possible before them. By controlling those parameters, one can study dependence of various physical properties as a function of controllable geometrical and compositional parameters. Such engineering ability may also provide a good basis for novel applications.

Beside electrons, quantized lattice vibrations, i.e. phonon spectra of quantum dots coexists with electrons and influences its optoelectronic properties mainly through electron-phonon interaction. Therefore, the third chapter deals with phonon spectra of quantum dots and electron-phonon interaction. Various models will be presented, namely bulk-like phonon models for SAQDs and confined phonon models for CQDs. In addition, electron-phonon interaction within each model will be discussed. The exact treatment of electron-phonon interaction leads to the concept of polaron and such concept will be introduced in the third chapter as well. It turns out that polaronic picture of carriers inside the quantum dots is required together with lattice anharmonicity in order to explain carrier relaxation dynamics observed in experiments. The scientific contribution to this chapter are theoretical examination of confined phonon modes and intraband electron-phonon interaction in CQDs. Such consideration revealed strong electron-phonon interaction which strongly influences transport properties of CQD spercrystals considered in the fifth chapter.

Optoelectronic properties of any condensed matter system are studied by applying electromagnetic field to the system and measuring the response.

Therefore, well defined theoretical approach of calculation of responses due to applied fields has to be established in order to explain experimentally measured responses and to further model considered system for potential applications. The fourth and the fifth chapter are dedicated to the optical and transport properties of quantum dots respectively. These properties will be modeled perturbatively with respect to the external electromagnetic perturbation within the framework of the linear response theory. The scientific contribution in the fourth chapter is derived relation between non-radiative lifetime between first excited and ground states in quantum dot due to electron-phonon interaction and optical transition strength between excited and ground states. Such relation provides additional testing possibilities in the proposed intraband polaronic picture in quantum dots. It also connects non-radiative lifetime to the radiative lifetime, both of which are very important quantities for lasing. In the fifth chapter, polaronic modeling of CQD supercrystals is presented. The formation of polarons was studied as a function of temperature and the electronic interdot coupling and mobilities of such polarons were calculated. Conclusions on the nature and regimes of transport were drawn which is the main scientific contribution of the fifth chapter.

Chapter 2

Electronic Structure

Electrons in any condensed matter system are charge carriers and as such they are responsible for the interaction of the condensed matter system with external electromagnetic field. More complex particles such as polarons have their electronic component interacting with the same field. Therefore, it is of crucial importance to develop models for obtaining the electronic spectra in quantum dots. For rough estimation of optoelectronic properties it is enough to consider only electronic degrees of freedom and to omit phonons from consideration.

This chapter deals with methods of obtaining the eigenstates of electrons and holes residing in semiconductor quantum dots. Typical dimensions of quantum dots are hundreds of angstroms which gives the estimation that quantum dot contains $\sim 10^6$ nuclei and even a larger number of electrons interacting among each other with long range Coulomb forces. Therefore, applying the full many body Hamiltonian to the problem is clearly impossible and some other smarter and efficient methods should be applied.

Fortunately, there is a wealth of theoretical methods that have been applied to the calculation of the electronic structure of bulk semiconductors,

many of which can be appropriately extended to quantum dots. All these theoretical methods can be divided into empirical methods and ab initio methods. Ab initio examples are density functional theory and tight binding method. Some empirical methods are empirical pseudopotential method, density patching method and envelope functions methods. This thesis will focus on envelope functions methods, namely effective mass envelope function method and $\boldsymbol{k} \cdot \boldsymbol{p}$ envelope functions method.

The idea of the $\boldsymbol{k} \cdot \boldsymbol{p}$ method and the effective mass method is to exploit the fact that carriers of interests in semiconductors mainly occupy valence and conduction band around Γ-point. The main idea is to form an effective Hamiltonian for carriers in conduction and valence band by taking into account exact electron Bloch functions at Γ-point and to perturbatively treat nearby states with different wavevectors. Historically, $\boldsymbol{k} \cdot \boldsymbol{p}$ models were introduced in order to study electron wavefunction of bulk electrons, approximately in vicinity of Γ-point. Considered Bloch wavefunctions at Γ-point should be taken from all bands where carrier could reside. Using of the envelope wavefunctions creates space for the extension of the $\boldsymbol{k} \cdot \boldsymbol{p}$ method to the case of semiconductor nanostructures. This method has therefore often been applied in quantum dot electronic structure calculations [87, 88, 89, 90, 91]. While possibly limited in the description of some subtle effects, the $\boldsymbol{k} \cdot \boldsymbol{p}$ method can inherently incorporate the effects of band mixing, strain, piezoelectricity, as well as the influence of external fields, keeping a lower computational cost compared to atomistic methods. Family of these methods is chosen to be the main tool of tackling the electronic structure problems in quantum dots. Since the main subject of this thesis is intraband physics of quantum dots, one band approximation will be satisfactory choice in most cases, especially due to polaronic nature of states in conduction band

which substantially increases computational demands. In addition, one band effective mass model is also used for description of electrons in CQDs [92].

The calculation of electronic states in quantum rods presents the main contribution of this chapter. Quantum rods are complex heterostructures containing height controllable quantum dot embedded with the quantum well. Electron states in the conduction band are also expected to exhibit mixture between the dot and the well states and that is the main reason why we have chosen to study them. Eight band $\boldsymbol{k} \cdot \boldsymbol{p}$ method will be introduced in case of quantum rod's electronic structure due to compositional complexity and originality of these structure. One band effective mass model will be used in order to demonstrate one very exotic feature of quantum rods. The existence of the bound dot state in the continuum appeared from 8 band $\boldsymbol{k} \cdot \boldsymbol{p}$ consideration and one band effective mass model was used in order to prove that such state is entirely due to confinement interplay of the dot and the surrounding well.

This chapter is organized as follows. Firstly, envelope functions models are introduced. Some simple cases such as infinite quantum dot and quantum well are studied with effective mass model. The conclusions from this study will serve to explain results of the 8 band $\boldsymbol{k} \cdot \boldsymbol{p}$ simulation for quantum rods. Finally, effective mass model will be used to explain the existence of the bound state in the continuum in quantum rods.

2.1 Envelope Functions Methods

2.1.1 One-band Effective Mass Model

One-band effective mass model will be derived here by using standard derivation procedure from [47]. This model represents the simplest form of enve-

lope functions models.

The full Hamiltonian of an electron in a homogeneous semiconductor [93] is

$$\hat{H} = \frac{\hat{\boldsymbol{p}}^2}{2m_0} + V_0(\boldsymbol{r}) + \hat{H}_{\text{so}}, \tag{2.1}$$

where $\hat{\boldsymbol{p}}$ is the momentum operator, $V_0(\boldsymbol{r})$ the periodic crystal potential (including nuclei, core electrons and self-consistent potential of valence electrons), and

$$\hat{H}_{\text{so}} = \frac{\hbar}{4m_0^2 c^2} \left[\nabla V_0(\boldsymbol{r}) \times \hat{\boldsymbol{p}} \right] \cdot \boldsymbol{\sigma}, \tag{2.2}$$

is the spin-orbit interaction Hamiltonian arising from relativistic corrections to Schrödinger equation. Spin factor $\boldsymbol{\sigma}$ is a vector of Pauli matrices

$$\sigma_x = \begin{bmatrix} 0 & 1 \\ 1 & 0 \end{bmatrix}, \sigma_y = \begin{bmatrix} 0 & -i \\ i & 0 \end{bmatrix}, \sigma_z = \begin{bmatrix} 1 & 0 \\ 0 & -1 \end{bmatrix}. \tag{2.3}$$

The wavefunction of an electron in a periodic potential, i.e. bulk semiconductors, can be expressed as

$$\Psi_{n\boldsymbol{k}}(\boldsymbol{r}) = u_{n\boldsymbol{k}}(\boldsymbol{r}) e^{i\boldsymbol{k}\cdot\boldsymbol{r}}, \tag{2.4}$$

where $\boldsymbol{k}$ is the wave vector from the first Brillouin zone and $u_{n\boldsymbol{k}}(\boldsymbol{r})$ is a periodic function, a so called Bloch function.

Heterostructures are consisted of several domains, of which each is filled with corresponding homogeneous semiconductor material. If one denotes each coordinate domain counted by index μ as D_μ then the Hamiltonian becomes

$$\hat{H} = \frac{\hat{\boldsymbol{p}}^2}{2m_0} + \hat{V}_0^\mu(\boldsymbol{r}) + \hat{H}_{\text{so}}^\mu \text{ for } \boldsymbol{r} \in D_\mu \tag{2.5}$$

where $\hat{V}_0^\mu(\boldsymbol{r})$ is the periodic crystal potential of the semiconductor of the

domain μ. The spin-orbit interaction term $\hat{H}_{\text{so}}$ is defined via $\hat{V}_0^{\mu}(\boldsymbol{r})$.

However, even though corresponding semiconductors are different, they are usually very similar, at least in the lattice type they posses. In such way, entire heterostructure can be seen as a single bulk with the different physical parameters depending on the coordinate. In heterostructures, the wavefunction of the electron is not periodic any longer, but can be expanded in the eigenfunctions of the Hamiltonian of bulk semiconductor of the dominant domain in the heterostructure. This is justified due to the similarity of the different materials inside the heterostructure.

$$\Psi(\boldsymbol{r}) = \sum_n \int_{\text{FBZ}} \chi_{n,\boldsymbol{k}} e^{i\boldsymbol{k}\cdot\boldsymbol{r}} u_{n\boldsymbol{k}}(\boldsymbol{r}) \mathrm{d}^3\boldsymbol{k}, \tag{2.6}$$

where integration goes over the first Brillouin zone.

Approximately, only a finite number of bands in summation (2.6) can be included in formalism. Model is called one-band if only conduction band Bloch function in Γ-point is included or multi-band if Bloch functions from lower bands in Γ-point are included.

For intraband physical process, it is enough to consider only the one-band model. Furthermore, in heterostructures as well as in bulk electrons reside usually at the point $\boldsymbol{k} = 0$. This implies that electron wavefunction slowly varies in space containing waves $e^{i\boldsymbol{k}\cdot\boldsymbol{r}}$ with small values of $\boldsymbol{k}$. In such small range of possible values of $\boldsymbol{k}$, one can assume that Bloch function $u_{0\boldsymbol{k}}$ does not depend on $\boldsymbol{k}$. One then gets

$$\Psi(\boldsymbol{r}) = u_0(\boldsymbol{r}) \int_{\text{FBZ}} \chi(\boldsymbol{k}) e^{i\boldsymbol{k}\cdot\boldsymbol{r}} \mathrm{d}^3\boldsymbol{k} = \psi(\boldsymbol{r}) u_0(\boldsymbol{r}), \tag{2.7}$$

where the function $\chi(\boldsymbol{k})$ represents Fourier transform of the envelope function $\psi(\boldsymbol{r})$

In order to form a differential equation for envelope function, one has to examine how heterostructure Hamiltonian (2.5) acts on the envelope function. By straightforward insertion one gets

$$\hat{H}\Psi(\boldsymbol{r}) = \int_{\mathrm{FBZ}} E_c\left(\boldsymbol{k}, \boldsymbol{r}\right) \chi\left(\boldsymbol{k}\right) e^{i\boldsymbol{k}\cdot\boldsymbol{r}} u_0(\boldsymbol{r}) \mathrm{d}^3\boldsymbol{k}. \tag{2.8}$$

Using the crystal eigenenergies $E_c\left(\boldsymbol{k}, \boldsymbol{r}\right)$ in the last expression is justified since the original wavefunction of the bulk semiconductor is $u_{n\boldsymbol{k}}(\boldsymbol{r})e^{i\boldsymbol{k}\cdot\boldsymbol{r}}$ and not the approximation $u_{n0}(\boldsymbol{r})e^{i\boldsymbol{k}\cdot\boldsymbol{r}}$. Also, the dependence on the coordinate $\boldsymbol{r}$ is retained in the crystal eigenenergies to account for the heterostructure inhomogeneity. Furthermore, crystal eigenenergies can be expanded in Taylor series around $\boldsymbol{k} = 0$ and expressed in terms of effective masses as $E_c\left(\boldsymbol{k}, \boldsymbol{r}\right) = E_{c0}(\boldsymbol{r}) + \frac{\hbar^2}{2m^*(\boldsymbol{r})}k^2$ which gives

$$\hat{H}\Psi(\boldsymbol{r}) = E_{c0}(\boldsymbol{r})u_0(\boldsymbol{r})\psi_0(\boldsymbol{r}) + \frac{\hbar^2}{2m^*(\boldsymbol{r})}u_0(\boldsymbol{r})\int_{\mathrm{FBZ}} k^2\chi_{\boldsymbol{k}}e^{i\boldsymbol{k}\cdot\boldsymbol{r}}\mathrm{d}^3\boldsymbol{k} \tag{2.9}$$

where m^* represents effective mass of electron in conduction band. By using the rule for Fourier transform of the function derivative one gets

$$\hat{H}\psi_0(\boldsymbol{r}) = E_{c0}(\boldsymbol{r})\psi_0(\boldsymbol{r}) - \frac{\hbar^2}{2m^*(\boldsymbol{r})}\nabla^2\psi_0(\boldsymbol{r}), \tag{2.10}$$

Finally, the eigenproblem for envelope function in one band approximation can be written as

$$-\frac{\hbar^2}{2m^*(\boldsymbol{r})}\nabla^2\psi_0(\boldsymbol{r}) + E_{c0}\left(\boldsymbol{r}\right)\psi_0(\boldsymbol{r}) = E\psi_0(\boldsymbol{r}), \tag{2.11}$$

which represents Schrödinger equation for envelope function. Since the effective mass $m^*(\boldsymbol{r})$ generally depends on coordinates, one has to modify Eq. (2.11) in order to achieve Hermicity of the effective Hamitlonian. This

can be done in the following manner

$$-\hbar^2 \nabla \frac{1}{2m^*(\boldsymbol{r})} \nabla \psi_0(\boldsymbol{r}) + E_{c0}(\boldsymbol{r}) \psi_0(\boldsymbol{r}) = E \psi_0(\boldsymbol{r}), \qquad (2.12)$$

Eigensolutions and eigenenergies of an electron in conduction band of heterostructure are obtained using the equation (2.12). For more complicated physics of interband transitions it is necessary to include more bands in expansion (2.6).

2.1.2   8 Band $\boldsymbol{k} \cdot \boldsymbol{p}$ Model

The presented derivation of the envelope function formalism relies upon expansion of the crystal eigenenergies around $k = 0$ point introducing the effective mass. Effective mass model can also be seen as the simplest form of the $\boldsymbol{k} \cdot \boldsymbol{p}$ models. (The difference is still that $\boldsymbol{k} \cdot \boldsymbol{p}$ method does not "a priori" use the empirical effective mass parameter) In this section, $\boldsymbol{k} \cdot \boldsymbol{p}$ formalism will be derived without introducing any phenomenological parameters such as effective mass. The aim of this section is to explain mathematical and quantum mechanical background of the $\boldsymbol{k} \cdot \boldsymbol{p}$ models. Detailed information on the models can be found elsewhere in the literature (e.g. Refs. [93, 94]). The derivation procedure is original compared to standard ones found in literature.

In order to study full excitonic features of semiconductors, one has to include all valence bands and conduction band into account. Even if one is only interested in electrons from the conduction band, one can consider valence bands as well since there always exists an admixture of valence Bloch wavefunctions in an electron state in the conduction band.

As already stated, general electron wave function in a heterostructure can

be expanded in wavefunctions of the Hamiltonian (see Eq. (2.6)) together with additional approximation that Bloch wavefunction does not depend significantly on the wavevector $\boldsymbol{k}$ around $\boldsymbol{k} = 0$ point:

$$\Psi(\boldsymbol{r}) = \sum_n \int_{\mathrm{FBZ}} \chi_{n,\boldsymbol{k}} e^{i\boldsymbol{k}\cdot\boldsymbol{r}} u_{n0}(\boldsymbol{r}) \mathrm{d}^3\boldsymbol{k} = \sum_n \psi_n(\boldsymbol{r}) u_{n0}(\boldsymbol{r}), \qquad (2.13)$$

where $\psi_n(\boldsymbol{r})$ are envelope wavefunctions corresponding to the band n. Functions $\chi_{n,\boldsymbol{k}}$ are obviously Fourier components of the corresponding envelope functions. It has been pointed out in Ref. [95] that (2.13) is an exact representation of the eigenfunction $\Psi(\boldsymbol{r})$ if the same u_i functions are used throughout the whole heterostructure, although corresponding spectrum and effective masses will be left to vary in space. This practically means that one electron Hamiltonian (2.1) acts with different energy eigenvalues on the Bloch function at Γ-point depending on the coordinate inside the heterostructure. All these assumptions were made as well in the previous section. However, for the case in the previous section, the approximation that $u_{n\boldsymbol{k}}(\boldsymbol{r})e^{i\boldsymbol{k}\cdot\boldsymbol{r}}$ can be replaced with $u_{n0}(\boldsymbol{r})e^{i\boldsymbol{k}\cdot\boldsymbol{r}}$ has been done after acting of the Hamiltonian on the assumed wavefunction (Eq. (2.8)) and the crystal eigenenergies were approximated. Here, this approximation has been already made and the aim is to obtain the effective acting of the Hamiltonian to the approximated wavefunction in order to avoid using of the effective mass as input parameter.

Wavefunction (2.13) consists of linear combination of the products of the slow varying envelope function factor and fast varying Bloch factor. The aim is to derive differential equations for envelope functions by acting with Hamiltonian (2.5) upon wavefunction (2.13) and then projecting obtained equation onto each Bloch function $u_{n0}(\boldsymbol{r})$. Projection on each Bloch

function $u_{n0}(\boldsymbol{r})$ means multiplying with conjugate of $u_{n0}(\boldsymbol{r})$ and integrating over the unit cell. Only fast varying factors similar to $u_{n0}(\boldsymbol{r})$ will follow this integration while the slow envelope function factors will remain in the equation and obtained equation would represent the equation for envelope functions.

By acting with Hamiltonian (2.5) upon wavefunction (2.13) one obtains:

$$\hat{H}\Psi(\boldsymbol{r}) = \sum_n \left[\left(\frac{\hat{p}^2}{2m_0} u_{n0}(\boldsymbol{r}) \right) \int_{\mathrm{FBZ}} \chi_{n,\boldsymbol{k}} e^{i\boldsymbol{k}\cdot\boldsymbol{r}} \mathrm{d}^3\boldsymbol{k} + \right. \tag{2.14}$$

$$+ \left(V_0(\boldsymbol{r}) + \hat{H}_{\mathrm{so}} \right) u_{n0}(\boldsymbol{r}) \int_{\mathrm{FBZ}} \chi_{n,\boldsymbol{k}} e^{i\boldsymbol{k}\cdot\boldsymbol{r}} \mathrm{d}^3\boldsymbol{k} -$$

$$- \frac{\hbar^2}{2m_0} u_{n0}(\boldsymbol{r}) \int_{\mathrm{FBZ}} (ik)^2 \chi_{n,\boldsymbol{k}} e^{i\boldsymbol{k}\cdot\boldsymbol{r}} \mathrm{d}^3\boldsymbol{k} -$$

$$\left. - \frac{\hbar}{m_0} (\hat{\boldsymbol{p}} u_{n0}(\boldsymbol{r})) \cdot \int_{\mathrm{FBZ}} i\boldsymbol{k}\chi_{n,\boldsymbol{k}} e^{i\boldsymbol{k}\cdot\boldsymbol{r}} \mathrm{d}^3\boldsymbol{k} \right],$$

where spin-orbit coupling term acting on envelope function factor has been omitted since it is proportional to k and for small values of k it is much weaker then spin-orbit coupling term acting on Bloch factor. Integrals over the first Brillouin zone are becoming envelope functions and corresponding derivatives (due to the properties of Fourier transform):

$$\int_{\mathrm{FBZ}} \chi_{n,\boldsymbol{k}} e^{i\boldsymbol{k}\cdot\boldsymbol{r}} \mathrm{d}^3\boldsymbol{k} = \psi_n(\boldsymbol{r}) \tag{2.15}$$

$$\int_{\mathrm{FBZ}} i\boldsymbol{k}\chi_{n,\boldsymbol{k}} e^{i\boldsymbol{k}\cdot\boldsymbol{r}} \mathrm{d}^3\boldsymbol{k} = \boldsymbol{\nabla}\psi_n(\boldsymbol{r})$$

$$\int_{\mathrm{FBZ}} (ik)^2 \chi_{n,\boldsymbol{k}} e^{i\boldsymbol{k}\cdot\boldsymbol{r}} \mathrm{d}^3\boldsymbol{k} = \nabla^2\psi_n(\boldsymbol{r}).$$

Eq. (2.14) can be projected on each Bloch function $u_{m0}(\boldsymbol{r})$. The projection means multiplying the entire Eq. (2.14) by $u_{m0}(\boldsymbol{r})^*$ and integrating over the unit crystal cell. Slow varying envelope function can be considered as nearly constant over single unit cell and integration is done only over fast varying

factors.

This is analogous to the case of solving the linear numerical problems (such as differential equations or differential equations eigenproblems) by wavefunction expansion method or method of moments, where wavefunctions are considered as vectors and corresponding linear numerical problem is seen as obtaining the matrix form representation of the differential equation within the chosen wavefunction basis.

Here situation is more complex as the operator (2.5) considered lives in the space which is formed as the direct product of the space formed by fast varying functions $u_{n0}(\boldsymbol{r})$ and slow varying enevelope functions $e^{i\boldsymbol{k}\cdot\boldsymbol{r}}$ respectively. This step can be then seen as the direct representation of the operator (2.5), but only in the factor space defined by fast varying functions $u_{n0}(\boldsymbol{r})$.

Slow varying envelope functions can be considered as constant over the unit cell and integration goes only over fast varying functions such as Bloch factors, potential $V_0(\boldsymbol{r})$ and $\hat{H}_{\mathrm{so}}$. In order to proceed further, the following identity will be used:

$$\langle u_{m0}|\,\frac{\hat{p}^2}{2m_0} + V_0(\boldsymbol{r})\,|u_{n0}\rangle = \delta_{mn}E_{n0}(\boldsymbol{r}) \tag{2.16}$$

where $E_{n0}(\boldsymbol{r})$ is the Bloch eigenenergy of the $n-th$ band in the Γ-point. Since heterostructure potential has its periodicity dependent on the coordinate domain D_μ, $E_{n0}(\boldsymbol{r})$ is varying over the domains correspondingly.

Each projection gives one coupled equation for envelope functions $\psi_n(\boldsymbol{r})$. The total number of equations is then the same as the number of unknown envelope functions, i.e. the number of included bands.

After choosing the bands for state expansion, the whole eigenproblem

reduces to the $Z \times Z$ (where Z is total number of included bands) system of linear differential equations for envelope functions. Matrix Hamiltonian of such system is:

$$h_{mn} = \left(E_{n0}(\boldsymbol{r}) - \frac{\hbar^2}{2m_0}\nabla^2 \right) \delta_{m,n} - \tag{2.17}$$
$$- \frac{i\hbar}{m_0} \langle u_{m0}| \hat{\boldsymbol{p}} |u_{n0}\rangle \cdot \nabla + \langle u_{m0}| \hat{H}_{\text{so}} |u_{n0}\rangle .$$

In order to study full excitonic features of quantum dots the natural choice is to include the highest states in the valence band and the lowest states in the conduction band. For zincblende crystals such as InAs and GaAs that are mostly of interest here, the valence structure consists of three bands: light hole band, heavy hole band and spin-split-off band. When combined with spin degrees of freedom, there are total 8 bands included in the formalism. One can in principle work in this basis, although it is more usual to work in the basis of the total angular momentum operator $|JJ_z\rangle$ that diagonalizes the Hamiltonian at $\boldsymbol{k} = 0$. Matrix elements $\langle u_{m0}| \hat{H}_{\text{so}} |u_{n0}\rangle$ and $\langle u_{m0}| \hat{\boldsymbol{p}} |u_{n0}\rangle$ are calculated by using the crystal symmetry properties of the homogeneous semiconductor and detailed expressions can be found in Ref. 93.

As well as in the one band case, one must to perform some kind of modification of explained method in order to make Hamiltonian (2.17) hermitian. That can be done similarly as in Eq. (2.12) by rearrangement of envelope function operators. Many of the existing quantum dot electronic structure calculations [89, 87] use heuristic, symmetrical arrangement of operators

$$f(\boldsymbol{r})\nabla_i \nabla_j \to \frac{1}{2} \left(\nabla_i f(\boldsymbol{r})\nabla_j + \nabla_j f(\boldsymbol{r})\nabla_i \right), \tag{2.18}$$
$$f(\boldsymbol{r})\nabla_i \to \frac{1}{2} \left(\nabla_i f(\boldsymbol{r}) + f(\boldsymbol{r})\nabla_i \right).$$

Finally, 8 band $\boldsymbol{k} \cdot \boldsymbol{p}$ models is formulated as diagonalization of the 8×8 operator matrix for envelope functions. Eigensolution of such matrix is corresponding vector where each dimension represents the space of one envelope function. Thus, one deals with system of multiple differential equations eigenproblem. The detailed form of matrices for the basis of the total angular momentum operator $|JJ_z\rangle$ that diagonalizes the Hamiltonian at $\boldsymbol{k} = 0$ are given in Ref. 93.

2.1.3 Influence of Strain and Löwdin Correction

The theory presented in section 2.1.2 can be further extended to account for additional effects that in specific circumstances can greatly affect electronic structure. The important one is strain field arising from lattice mismatch of dot and bulk region. Second one is inclusion of additional bands in perturbative manner.

Strain is caused by the displacement of constituent atoms from their equilibrium positions. Microscopic potential for electrons inside the condensed matter system changes accordingly. Strain can be induced by lattice mismatch during the growth of heterostructures with different lattice constant or arises due to lattice vibrations. Nevertheless, one has to theoretically incorporate and model the effect of displacement field on microscopic potential for carriers.

Displacement field defines the strain tensor components as

$$e_{ij} = \frac{1}{2}\left(\frac{\partial u_i}{\partial x_j} + \frac{\partial u_j}{\partial x_i}\right). \tag{2.19}$$

where u_i is $i-th$ Cartesian component of the displacement field and x_i is just the $i-th$ Cartesian component of the coordinate.

In order to incorporate strain effects due to lattice mismatch in $\boldsymbol{k}\cdot\boldsymbol{p}$ model one has to find the strain distribution in semiconductors heterostructures. The most efficient way to do that is to use finite element method to minimize total elastic energy as described in [96]. Once the strain distribution and strain components are obtained, one can incorporate them in $\boldsymbol{k}\cdot\boldsymbol{p}$ by using the theory described in [90, 97] which is here briefly summarized. A case of the strain homogeneous in space will be assumed. Crystal potential of the strained crystal is denoted as $V_{\overleftrightarrow{e}}(\boldsymbol{r})$ and that of unstrained crystal as $V(\boldsymbol{r})$. The periodicity of the crystal under the strain is still present, but with a different deformed unit cell. Basis vectors of deformed unit cell are related to the original basis vectors by [90]:

$$\boldsymbol{a}'_i = \sum_j (\delta_{ij} + e_{ij})\boldsymbol{a}_j. \tag{2.20}$$

A point that was located at $\boldsymbol{r} = \sum_i x_i \boldsymbol{a}_i$ can be expressed via new coordinates of the deformed basis vectors $\boldsymbol{r} = \sum_i x'_i \boldsymbol{a}'_i$. The relation between the old and new coordinates is then

$$x_i = \sum_j (\delta_{ij} + e_{ij})x'_j. \tag{2.21}$$

or in matrix notation:

$$\boldsymbol{r} = \boldsymbol{r}' + \overleftrightarrow{e} \cdot \boldsymbol{r}' \tag{2.22}$$

The relationship between momentum operators in old and new coordinates is then up to terms linear in strain

$$\hat{p}_i = \sum_j (\delta_{ij} - e_{ij})\hat{p}'_j. \tag{2.23}$$

The transformed strained potential has the form:

$$V'_{\overleftrightarrow{e}}(\boldsymbol{r}') = V_{\overleftrightarrow{e}}(\boldsymbol{r}' + \overleftrightarrow{e} \cdot \boldsymbol{r}') \tag{2.24}$$

Returning the notation from $\boldsymbol{r}'$ to $\boldsymbol{r}$ one obtains the potential $V_{\overleftrightarrow{e}}(\boldsymbol{r} + \overleftrightarrow{e} \cdot \boldsymbol{r})$ which now has the same periodicity as unstrained crystal potential $V(\boldsymbol{r})$. Bloch's theorem can now be applied only if the transformed potential and momentum are used in Hamiltonian (2.1), notated with old coordinates if one wishes. The real crystal potential $V_{\overleftrightarrow{e}}(\boldsymbol{r} + \overleftrightarrow{e} \cdot \boldsymbol{r})$ is up to terms linear in strain then given by [97]:

$$V_{\overleftrightarrow{e}}(\boldsymbol{r} + \overleftrightarrow{e} \cdot \boldsymbol{r}) = V(\boldsymbol{r}) + \sum_{ij} V_{ij}(\boldsymbol{r})e_{ij}, \tag{2.25}$$

where

$$V_{ij}(\boldsymbol{r}) = \frac{1}{2 - \delta_{ij}} \lim_{\overleftrightarrow{e} \to 0} \frac{V_{\overleftrightarrow{e}}(\boldsymbol{r} + \overleftrightarrow{e} \cdot \boldsymbol{r}) - V(\boldsymbol{r})}{e_{ij}} \tag{2.26}$$

The factor in front of the limit is due to identical terms arising from exchanging the indexes i and j. The exact derivation of this perturbation term is given via considerations based on microscopic approach and crystal point group symmetry properties and is given in Ref. [97]. New strained $\boldsymbol{k} \cdot \boldsymbol{p}$ envelope function matrix in old coordinate notation reads as [90]:

$$h'_{mn} = h_{mn} + D^0_{mn} + D^1_{mn}, \tag{2.27}$$

where

$$D^0_{mn} = -\sum_{ij} e_{ij} \left\langle u_{m0} \left| \frac{\hat{p}_i \hat{p}_j}{m_0} \right| u_{n0} \right\rangle + \sum_{ij} e_{ij} \left\langle u_{m0} \left| V_{ij}(\boldsymbol{r}) \right| u_{n0} \right\rangle \tag{2.28}$$

and

$$D_{mn}^1 = -i\frac{\hbar}{m_0}\sum_{ij}e_{ij}\langle u_{m0}|\hat{p}_j|u_{n0}\rangle\nabla_i. \tag{2.29}$$

The terms that couple the strain to the spin-orbit interaction have been neglected as is exclusively done in the literature [91, 89].

The finite number of chosen bands included in the $\boldsymbol{k}\cdot\boldsymbol{p}$ model is clearly an approximation. Not included bands may influence the model and a smart way of their inclusion should be applied. Bare increasing of the number of included bands increases computational cost significantly and cannot be applied. There is, however, a more attractive approach due to Löwdin [98], which allows one to perturbatively take into account the influence of the states outside the chosen manifold (so called remote bands), and at the same time keep the size of the Hamiltonian matrix at the same value. Within Löwdin's perturbation theory, the Hamiltonian U with second-order perturbative corrections due to the influence of remote bands is given by

$$U_{\alpha\beta} = H_{\alpha\beta} + \sum_r \frac{H_{\alpha r}H_{r\beta}}{E - H_{rr}}, \tag{2.30}$$

where the indices α and β refer to states within the chosen bands, and r to all other bands. The eigenvalue problem of U obviously a nonlinear problem since the energy E explicitly appears in the expression for the correction. It is convenient then to replace E with specific value. The logical choice is to replace E with E_V when indices α and β run through valence band, and with E_C when the same indices run through conduction band. When indices α and β run through both conduction and valence bands then E is replaced with $\frac{1}{2}(E_C + E_V)$ [90]. The exact matrices containing the effects of strain and Löwdin correction are given in Refs. 93 and 90.

2.2 Quantum Dot and Well with Infinite Potential Barriers

In order to obtain simplified picture of various interesting phenomena discussed in this thesis, the effective mass model will be firstly demonstrated on a three simple examples: the cuboid quantum dot, spherical quantum dot and quantum well, all with infinite potential walls.

Consider the cuboid quantum well with infinite potential walls which will be subsequently referred to as quantum box. The base of such cuboid is a square with side length a with its height denoted as d. Envelope function eigenproblem described by equation (2.12) for infinite cuboidal symmetry is solved with separation of variables. Thus, i-th eigenvector for such eigenproblem is:

$$\Psi_i\left(x,y,z\right) = \frac{2\sqrt{2}}{a\sqrt{d}}\sin\left(\frac{xn_x^i\pi}{a}\right)\sin\left(\frac{yn_y^i\pi}{a}\right)\sin\left(\frac{zn_z^i\pi}{d}\right) \qquad (2.31)$$

with energy

$$E_i = \frac{\pi^2\hbar^2}{2m^*a^2}\left(n_x^{i2} + n_y^{i2}\right) + \frac{\pi^2\hbar^2}{2m^*d^2}n_z^{i2}. \qquad (2.32)$$

For $d > a$ first excited state is with quantum numbers $n_x = 1, n_y = 1, n_z = 2$ and second and third one are degenerated due to square shape basis.

In the same manner, one band model for infinitely deep well is solved by separation of variables and eigensolutions are

$$\Psi_{k_x,k_y,n}\left(x,y,z\right) = \frac{\sqrt{2}}{a\sqrt{d}}e^{ik_xx}e^{ik_yy}\sin\left(\frac{zn\pi}{d}\right) \qquad (2.33)$$

and corresponding eigen-energies

$$E_{k_x,k_y,n} = \frac{\hbar^2}{2m^*}\left(k_x^2 + k_y^2\right) + \frac{\pi^2\hbar^2}{2m^*d^2}n^2. \qquad (2.34)$$

Quantum number n counts well boundstates as subbands with parabolic dependance of energy on k_x and k_y.

Electronic structure of colloidal nanocrystals can also be considered within the effective mass approximation. Colloidal nanocrystals are generally of spherical shape embedded in insulating dielectric which can be considered as infinite potential barrier for carriers. Therefore, Eq. (2.12) can be neatly solved in spherical coordinates. By separation of variables due to spherical symmetry, following eigenfucntions are obtained for the quantum dot of radius a and infinite well walls:

$$\Psi_{lmn}\left(\boldsymbol{r}\right) = \sqrt{\frac{2}{a^3 j_{l+1}^2\left(\alpha_{nl}\right)}} j_l\left(k_n \boldsymbol{r}\right) Y_{lm}\left(\theta, \phi\right) \tag{2.35}$$

where k_n is radial wavevector determined by the boundary condition

$$\Psi_{lmn}\left(a\right) = 0, \tag{2.36}$$

i.e. $k_n = \frac{\alpha_{nl}}{a}$ where α_{nl} is the nth zero of the spherical Bessel function of order l: j_l. $Y_{lm}\left(\theta, \phi\right)$ are spherical harmonics. Energy spectrum is given as:

$$E_{lmn} = \frac{\alpha_{nl}^2 \hbar^2}{2m^* a^2} \tag{2.37}$$

One can see, from the presented models for spherical and cuboidal quantum dot, that the ground electronic state in quantum dots resembles s atomic orbital and will be further refered to as s-like electronic state. Furthermore, first excited state in both cases resembles p orbitals and will be refered to as p-like electronic state.

2.3 Electronic Structure of Quantum Rods

2.3.1 Full Simulation for the Electronic Structure

It has been pointed out in section 1.2.2 that one of exotic modifications of quantum dots are elongated quantum dots, so called quantum rods. Quantum rods are elongated InGaAs quantum dots embedded in a InGaAs quantum well sandwiched by two GaAs bulk regions. They are roughly cylindrical in shape with relatively very large and fully controllable height-to-diameter aspect ratios. Such controllability is of great importance and allows experimental study of the electronic structure in terms of the height-to-diameter aspect ratio. This is the main reason why the electronic properties of these structures are studied by means of theoretical modeling. The exotic features such as height controllability and coexistence of the well and the dot appear very interesting for the potential applications.

A simplified model for geometric and compositional properties of these nanostructures are presented in Fig. 2.1. This structure consists of the GaAs/InGaAs quantum well of width h over the region between $-h/2$ and $h/2$. The quantum dot is positioned within the quantum well so that the bulk region is above and below the dot in the z-direction and the quantum well is surrounding the rod in the radial direction. In contrast to regular self-assembled quantum dots with typical heights of a few nanometers, quantum rods can be grown with heights up to several tens of nanometers. More details of the fabrication process have been given in section 1.2.2. The entire structure is optically active giving the combined features of dot, well and the bulk as it is obvious from PL measurements [1, 99]. The height of the rod and the width of the surrounding well are the same. This simplified model assumes that entire structure is cylindrically symmetric, even though such
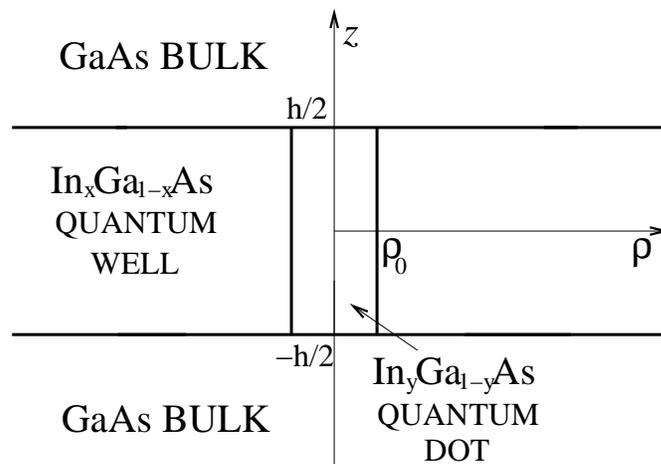
Figure 2.1: Simplified geometric model of a quantum rod. Cylindrical symmetry is assumed, so the entire structure can be depicted within the $z - \rho$ plane. Indium content of the dot region is larger than in the well region, i.e. $x < y$. The Figure has been taken from Ref. 3.

strict symmetry has not been reported. However, the general conclusions that follow do not depend on the exact shape of the rod basis. Therefore, we choose the circular shape of the basis in order to simplify theoretical consideration. The quantum rod has higher In content then the surrounding quantum well which makes the dot energetically deeper than the surrounding well.

A recent experiment on carrier capture dynamic in quantum rod structures excited by optical pump in terahertz range[100] imply that quantum rods are becoming highly attractive nanostructures for future device applications. Moreover, the most recent report[101] that charged quantum rods and their quantum well matrix can result in a perforated electron gas (perforated electron gas is 2D electron gas with electronless holes dispersed all over the 2D plain of the gas) has contributed significantly to raising interest

in these novel structures. It is therefore of great importance to develop a full theoretical description of electronic and optical properties which would enable the purpose-engineering of quantum rod structures.

Initial work in this area was focused on the calculation of energy levels and interband optical properties [1, 21, 102] as well as theoretical examinations of dominant physical effects affecting interband optical properties [103].

The electronic structure of quantum rods will be calculated using 8 band $\mathbf{k} \cdot \mathbf{p}$ envelope functions model described in 2.1.2, due to complex compositional properties that these structure exhibit. The strain distribution was found within the continuum mechanical model[87], with the calculation based on the finite element method[104]. The size of the box used in calculation of the strain distribution is significantly larger then the size of the rod and it was chosen by increasing until numerical convergence has been achieved.

Rods of cylindrical shape were considered and the cylindrical symmetry approximation [105] was introduced. In such a way, the problem was reduced from a three dimensional one to a two dimensional one. The Hamiltonian eigenvalue problem was then solved by using the orthonormal function expansion method where the basis was formed from the direct product of Bessel functions in the radial direction and the plane waves in the growth (z) direction. The cylindrical symmetry of the rods introduces a good quantum number of the $z-$component of the total quasi-angular momentum m_f which takes the half-integer values [105, 106]. The optical transition selection rules then allow only the transitions with $\Delta m_f = 0$ in the case of $z-$polarized radiation and $|\Delta m_f| = 1$ for $x-$polarized radiation.

The quantum rod material composition and geometric parameters were

taken in accordance with recent experiments from the literature. The diameter was taken to be equal to 10 nm [1]. The height of the rod was varied from 2.5 nm to 60 nm, which covers the typical range of quantum rod heights [1, 21]. The InAs/GaAs short-period superlattice, away from the quantum rod, becomes an InGaAs quantum well layer with an In composition of 16% [1] during the growth of the structure. The In content in the quantum rod is approximately 45% [1]. As it is cylindrically symmetric, i.e invariant on rotations around z - axis for any angle ϕ(polar coordinates) such structure is schematically shown in z - r plain in the upper part of Figs. 2.2 and 2.3 for rod heights of 10 nm and 60 nm. On the same figure is presented profile of conduction band edge in addition with energy of hydrostatic potential in the growth direction for $r = 0$. The position of the ground electronic state is also outlined on both figures. One can also regard this structure as quantum well with z axis as growth direction with additional deepening potential in the radial direction until $r = 5$ nm which corresponds to rod's radius.

Different bulk GaAs conduction band bottoms in Figs. 2.2 and 2.3 may seem surprising. Strain box was not taken big enough in order to relax strain completely on its edges. The reason for that is the fact that realistic structures consist of rod arrays and adjacent rods do not allow each other to relax the strain completely. Anyway, insufficient size of the strain box influences entire structure uniformly so the confinement effects are not influenced by the choice of the strain box. For that reason the position of the conduction band bottom of the entire structure with incorporated deformation potential correction due to hydrostatic strain increases with increasing the rod height.

Electronic structure diagram for rod heights of 60 nm and 10 nm is presented in Fig. 2.4. Wavefunctions module squared for number or relevant
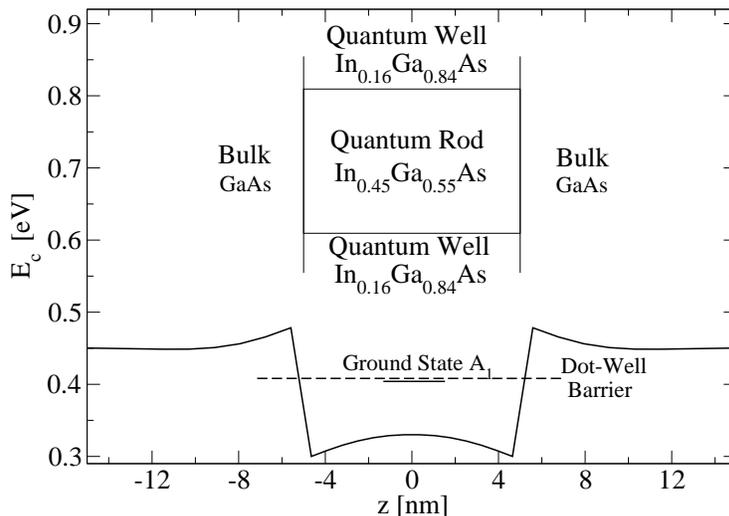
Figure 2.2: Profile of the conduction band with included additional hydrostatic strain potential for 10 nm tall quantum rod. Inset: Structural scheme in $z - r$ plain of the structure and compounds involved in building of it. Dashed line shows the approximate position of the dot-well barrier in radial direction. The Figure has been taken from Ref. 4.

states are also presented in same diagram for both structures. As already stated, the relative position of the ground electronic state denoted as A_1 is marked on the Figs. 2.2 and 2.3 so one can estimate the depth of the ground state in the dot.

Analyzing the quantum well potential deepened with quantum rod, all electronic states can be seen as bound, (quasi-bound) and free states in classical manner for the quantum well. Energy of the quasi bound states is lower than barrier in growth direction and energy of free states is higher than the same barrier.

Numerical simulation was executed in the subspace defined with basis functions which form Hilbert space in closed box and thus solutions are completely discrete. Such a situation can be regarded as approximation if
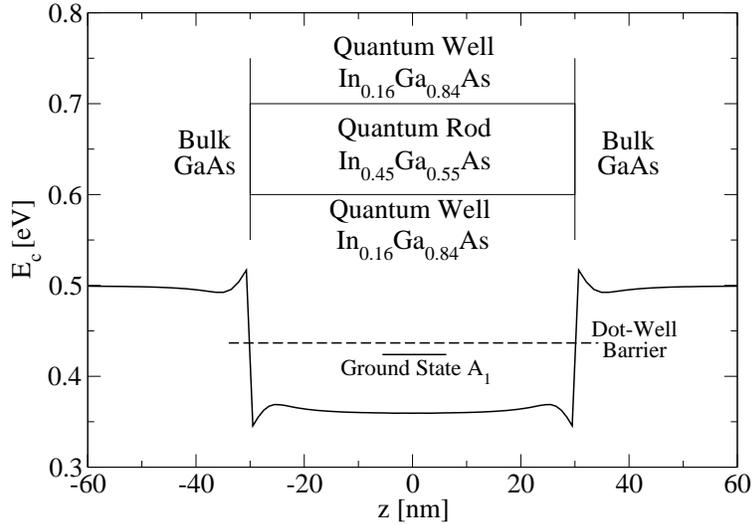
Figure 2.3: Profile of the conduction band with included additional hydrostatic strain potential for 60 nm tall quantum rod. Inset: Structural scheme in $z - r$ plain of the structure and compounds involved in building of it. Dashed line shows the approximate position of the dot-well barrier in radial direction. The Figure has been taken from Ref. 4.

we are dealing with continual spectra as we certainly are, in this case free states above barrier and quasi bound subbands in the well. All bound states can be further distributed in three subgroups. The first subgroup consists of localized states inside the dot whose existence is tailored by the dot. Those states are labeled with A on Fig. 2.4. The energy of the ground electronic state A_1 slightly approaches the bottom of the bulk conduction band of the dot material with increasing the dot height as shown on Figs. 2.2 and 2.3. This is expected since increased dot size toward the bulk limit should bring the ground state to the conduction band bottom value. However, this effect is not that strong as expected from Eqs. (2.32). The reasons for that might be non-infinite realistic barrier, some kind of combined effect of the growth and lateral direction confinement or simply just insufficient precision of the
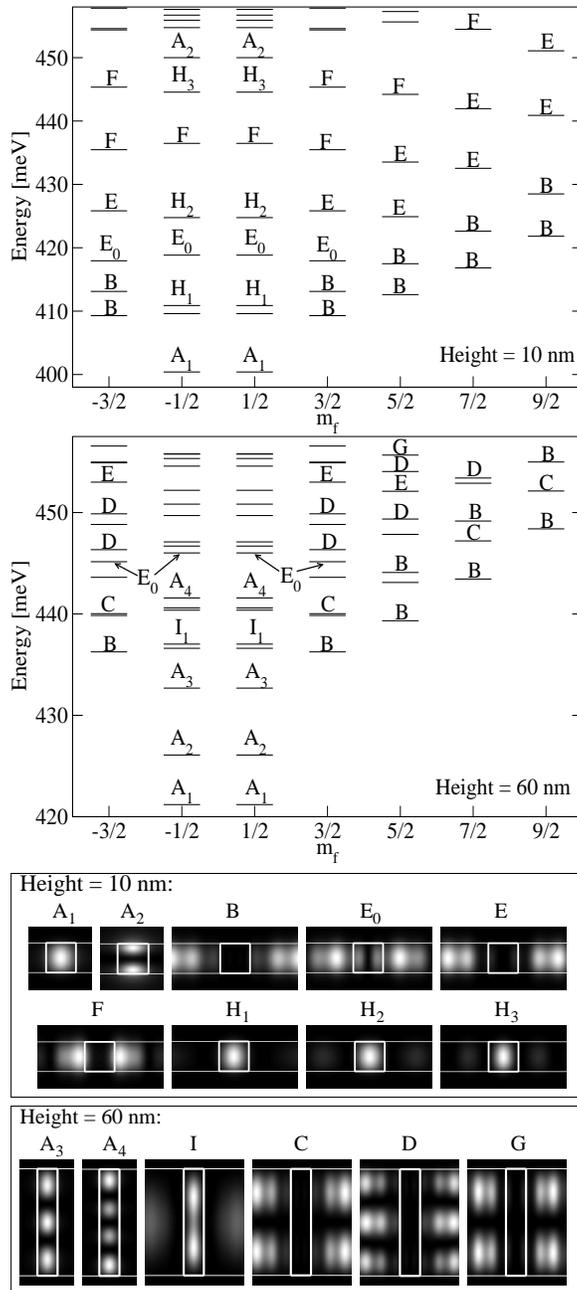
Figure 2.4: Energy diagrams for the quantum rods with 10 nm height(upper digram) and 60 nm lower diagram. Different types of the states have different labels. Lower part of the figure depicts some types of the states appearing in the quantum rods. States with same label are the same type of state regardless for which height they are depicted. Label A holds for completely bound states to the dot. States partially localized to the dot are labeled with I and H. Well states, i.e. states entirely delocalized into the well are labeled with B, C and D. Well states partially extending over the dot are labeled with E, F and G. The Figure taken from Ref. 4

numerical model.

The energy of A-states does not have to be lower than dot - well barrier in radial direction. In fact, states like A_4 for 60 nm height rod and state A_2 for 10 nm height rod are so high above dot-well barrier that some pure well states (which will be introduced in next paragraphs) are below them. As it will be shown later, these are so called bound states in the continuum. Reasons why those states exist even for energies higher then the barrier is due to additional confinement in z - direction. Dot - well barrier in radial direction is about 2 times lower then barrier in growth direction because In content in the dot is 3 times smaller then in the well, but the strain induced hydrostatic potential is higher in the well region than in bulk. Those states behave like bound states in the infinite dot described by Eq. (2.31). By increasing n_z in those equations increases the number of nodes along the growth direction which is in agreement with the shapes of dot states. Quantum number m_f from 8 band $\boldsymbol{k} \cdot \boldsymbol{p}$ model plays the similar role to quantum numbers n_x and n_y for envelope function quantum box model.

For taller rods energy difference between those bound states decreases, also in agreement to Eq. (2.32). It can be also seen from Fig. 2.4. For 60 nm rod height states A_1, A_2, A_3 are in order with energy differences of about 5 meV. For 10 nm rod height the first excited bound state A_2 is far from the ground state A_2 and it even exceeds not just the radial dot-well energy barrier, but the ground well state (which will be be introduced later).

Third state A_3 does not exist for 10 nm rods height as number of bound states in the well and the dot is reduced by decreasing the height of the dot, i.e. width of the well. However, there are some "bound" states labeled on Fig. 2.4 with H for 10 nm tall rod and with I for 60 nm tall rod. Some of those states are somewhat delocalized outside the dot but they still should

be regarded as dot tailored states. Some of those states are with no nodes like H states or one node like I states in the growth direction which confirms the order of their quantization. It may be that these states are hybrid states arising from the dot states above the dot-well-barrier. Since those states are surrounded by the well subband continuum then coupling of the dot state to the continuum may produce these slightly delocalized H and I states. Since initial electronic Hamiltonian solved was fully Hermitian, all states are expected to be orthogonalized. H and I states are partially localized to the dot and at first glance one might think that orthogonality between these states and A states is not satisfied. However, H and I states have different orbital quantum number for azimuth coordinate from A states. Since the quantum number m_f corresponds to total angular momentum composed of orbital and spin angular momentums then states H and I have orbital quantum number 1 which in combinations with spin quantum number $-\frac{1}{2}$ gives value $m_f = \frac{1}{2}$. A states have orbital quantum number 0 which in combination with spin quantum number $\frac{1}{2}$ gives the same value $m_f = \frac{1}{2}$. Even though A and H states have the same value of m_f and the similar look in radial direction they are orthogonal since their azimuth angle dependences and spins are different.

The second subgroup appears for energies much higher than dot well barrier in radial direction and lower then dot-bulk barrier in the growth direction, and those states are completely delocalized outside the rod (labels B, C and D) They are tailored by the well and will be referred to further as well states. Those states are, actually, quantum well quasibound states behaving like plane waves in the radial direction and can be distributed into subbands according to Eq. (2.33) and Eq. (2.34). Among the well states it is possible to recognize states from the same subband which have similar look

i.e. same number of nodes in the growth direction and similar wave behavior in the radial direction. In such manner, in Fig. 2.4, B denotes the first subband with no nodes in growth direction, C denotes the second subband with one node in the growth direction, and D denotes the third subband with two nodes in the growth direction. All those states are behaving like plane waves in radial direction. Fig. 2.4 shows that by increasing the quantum number m_f it is possible to observe certain parabolic subband. That is in full analogue to the simple infinite well wave in the radial (x or y) direction and its parabolic dependence of subbands when quantum numbers k_x and k_y increase.

As for the dot states, energy differences between quantum well states within different subbands with same m_f are decreased by increasing the rod's height, Eq. (2.34). There is also a larger number of subbands in the well. This causes more complicated situation in states ordering for taller rods. The density of states increases and thus interlacing of states from different subbands increases as clearly seen in Fig. 2.4.

The states which are mainly delocalized but extending to the dot as well form the third subgroup of bound states, denoted as mixed states. For example, one of those states is marked in Fig. 2.4 as E_0-state. Similar to them, more delocalized states are denoted as E, F and G which also form bands as states B, C and D. Their behavior in the radial direction is different. States E, F and G are not homogeneous waves in radial direction though they are delocalized. Furthermore, increasing the height of the rod has no consequence in decreasing of the energy separation between those quasi-subbands and other bands. Consequently, energy of those subbands does not depend strongly on the height of the structure or on the width of the well. The state E_0 behave as ground states for E quasi-subband,

therefore those bands are tailored both by the quantum rod and quantum well. States F_0 and G_0 as ground states for subbands F and G could be added on the diagram, but they are not marked on the Fig. 2.4 as their exact nature is less clear.

To conclude, by varying the height of the quantum rod structure, it is possible to tune the energy difference of all bound states in the way those differences are adjustable in quantum well or quantum dot separately. The energy separation between consecutive dot bound states is decreasing by increasing the rod height. The same phenomena occurs for energy difference between consecutive well states with same m_f, but from different subbands. The described phenomena has an impact on the order of the states as well as on frequency tunability of absorption spectra of growth direction polarized incident radiation. This will be more elaborated in section 4.7.

The main conclusion is that electronic spectra in conduction band of the quantum rods is extremely complex showing features of the pure quantum dot, pure quantum well and mixed states. There is vast number of hybrid states partially delocalized in the well and partially localized in the dot. Such states promise as very exotic for potential applications in optoelectronics since their boundness may increase the strength of the optical transitions while maintaining free carrier component important for efficient transport.

2.3.2 Bound States in the Continuum in Quantum Rods

If one takes closer look on the Fig. 2.4 one can notice that energies of some pure dot states marked with A lie above the energies of well states B. This exotic case means that fully localized state has an energy higher then some delocalized states which form the continuum.

Generally, semiconductor quantum dots exhibit full 3D confinement for

carriers, giving a few bound integrable states with a discrete spectrum below the barrier, and free non-integrable states with continuum spectrum above the barrier (for SAQDs). Quantum dots are often referred to as "artificial atoms" due to their discrete part of spectrum and discrete optical resonances arising from transitions between bound orbital states. Both atoms and SAQDs can be ionized, when electrons gain sufficient energy to escape the binding potential, and subsequently occupy free states - in vacuum in the case of atoms or bulk in the case of SAQDs.

However, boundness and discreteness of an orbital state in quantum dots do not come necessarily together. As stated above, quantum rods, exhibit bound excited state with an energy embedded in the continuum of other free electronic states, above the ionization threshold. This is a so called bound state in continuum (BIC). There are various types of BIC reported since the foundation of quantum mechanics, but none of them were reported for atomic or condensed matter systems. In what follows, a few BIC reported are listed.

The first prediction originates back to 1929 when von Neumann and Wigner showed such a possibility by mathematical construction of a bounded potential accommodating a BIC [107]. This issue was revitalized by Stillinger and Herick [108] pointing out, 46 years later, that a BIC could occur in some specific molecular systems. The first artificial semiconductor nanostructure accommodating the bound state above ionization threshold, was reported in Ref. [109]. This bound state was argued to be a consequence of Bragg reflection due to the superlattice. Even though above the barrier, this state wasn't surrounded by a continuum of states and it was strictly speaking a quasibound state with free motion in the lateral direction. Some theoretical proposals and proofs for the BIC existence were reported for

more complex quantum mechanical systems. For example, coupled system of electrons and nuclei in molecules [110] was considered. BIC, as an quantum mechanical interference effect can occur in various abstract models. Some examples of theoretical abstract systems that support BIC were reported in Refs. [111, 112, 113, 114, 115, 116]. Experimentally, only photonic crystal systems with the BIC were reported [117, 118]. A theoretical design of one-dimensional photonic heterostructure, supporting the BIC was provided in Ref. [119].

One can expect that the quantum rod would accommodate bound states only below the quantum well barrier in the radial direction. However, due to bulk confinement in the z-direction, bound states could also appear with energies above the well barrier where also well continuum states are present giving the BIC. Such a situation resembles the one from Ref. [109] where a bound state occurs above the barrier of a superlattice, but it isn't surrounded by continuum states because the state itself is an impurity state in the superlattice, spaced from the continuum superlattice bands. Also, such a BIC is strictly speaking a quasibound state. The main aim here is to prove that in the case of a quantum rod, such state above the barrier is indeed surrounded by the continuum and is indeed bound for a wide range of parameter space. This has to be done by using some simple model in order to determine the originating nature of the BIC existence.

Existence of the BIC in quantum rods is purely due to the interplay of the combined well and dot confinement. In order to prove this statement, consider the idealized quantum rod structure presented in Fig. 2.1. The quantum rod is considered isolated from the other quantum rods. We assume cylindrical symmetry of the entire structure, and the value of the embedding bulk barrier is set to infinity. The assumption of infinitely high bulk walls

does not affect the general conclusion since the same conclusion follows from the full 8-band $\boldsymbol{k} \cdot \boldsymbol{p}$ model where the values for all barriers in the structure were taken with precise offsets and included strain effects. Now it becomes clear that this simplified model of realistic quantum rods presents the 3D generalization of the 2D potential constructed by Robnik et al. [120] in order to obtain the BIC, with the quantum well as escaping channel. However, it was pointed out in the same reference that existence of BIC in such potential is sensitive to perturbation, especially the one which might break the parallel geometrical shape of escaping channel. That should not be a problem in this case, since the existence of quality quantum well seems very probable, and the walls of quantum well escaping channel can be considered parallel to the infinity.

The simplest approach to confinement effects on electron wavefunction is to consider one spinless electron single-band envelope function equation in polar coordinates:

$$\left(\frac{\hbar^2}{2} \nabla \frac{1}{m_e(\boldsymbol{r})} \nabla + E_c(\rho) + E_c^z(z) \right) \Psi(\boldsymbol{r}) = E\Psi(\boldsymbol{r}) \qquad (2.38)$$

where

$$E_c(\rho) = \begin{cases} 0 & \text{for } \rho < \rho_0 \\ U_b & \text{for } \rho > \rho_0 \end{cases}$$

and

$$E_c^z(z) = \begin{cases} 0 & \text{for } -\frac{h}{2} < z < \frac{h}{2} \\ \infty & \text{for } z < -\frac{h}{2} \text{ or } z > \frac{h}{2} \end{cases}$$

Values of the effective mass $m_e(\boldsymbol{r})$ are m_d and m_w in the dot and the well respectively. In the bulk, where the value of the potential is set to infinity, the value of the effective mass is unnecessary. The potential offset between

dot and the well region is U_b. Parameters ρ_0 and h are the radius and the height of the QR. Due to infinite bulk barrier and cylindrical symmetry, one can separate the variables of the wavefunction $\Psi\left(\mathbf{r}\right) = \Phi\left(\phi\right) Z\left(z\right) R\left(\rho\right)$. Furthermore, the solutions for $\Phi\left(\phi\right)$ and $Z\left(z\right)$ are $\Phi_l\left(\phi\right) = \frac{1}{\sqrt{2\pi}} e^{il\phi}$ and $Z_n\left(z\right) = \sqrt{\frac{2}{h}} \sin\left(\frac{n\pi}{h}\left(z + \frac{h}{2}\right)\right)$ where we introduce good quantum numbers l and n, integer and positive integers respectively. The remaining Schrödinger-like equation in the radial direction reads:

$$-\frac{\hbar^2}{2} \frac{1}{\rho} \frac{\mathrm{d}}{\mathrm{d}\rho} \frac{\rho}{m_e\left(\rho\right)} \frac{\mathrm{d}}{\mathrm{d}\rho} R_{nl}\left(\rho\right) + \tag{2.39}$$
$$+ \left(E_c\left(\rho\right) - E + \frac{\hbar^2}{2m_e\left(\rho\right)} \left(\frac{n^2\pi^2}{h^2} + \frac{l^2}{\rho^2}\right)\right) R_{nl}\left(\rho\right) = 0$$

Eq. (2.39) can be rewritten as

$$\rho^2 \frac{\mathrm{d}^2 R\left(\rho\right)}{\mathrm{d}\rho^2} + \rho \frac{\mathrm{d}R\left(\rho\right)}{\mathrm{d}\rho} + \left((k_{d/w}^n)^2 \rho^2 - l^2\right) R\left(\rho\right) = 0 \tag{2.40}$$

where the radial wavenumber depends on quantum number n only and is defined as
$$(k_{d/w}^n)^2 = \frac{2m_{d/w}}{\hbar^2} \left[E - E_{c,d/w} - \frac{\hbar^2 n^2 \pi^2}{2m_{d/w} h^2}\right]. \tag{2.41}$$

Subscripts d and w refer to the dot and well domain, respectively. All material parameters are constant within each of these regions. For a fixed n, the wavenumber squared for the dot region $(k_d^n)^2$ is positive in the range of energies $E > \frac{\hbar^2 n^2 \pi^2}{2m_d h^2}$. However, the wavenumber squared for the well region $(k_w^n)^2$ is negative in energy interval $E < U_b + \frac{\hbar^2 n^2 \pi^2}{2m_w h^2}$.

Therefore, the solution for an energy in the interval $\frac{\hbar^2 n^2 \pi^2}{2m_d h^2} < E < U_b +$

$\frac{\hbar^2 n^2 \pi^2}{2 m_w h^2}$ reads

$$R_{nl}(\rho) = \begin{cases} C_1 J_l(k_d^n \rho) & \text{for } \rho < \rho_0 \\[2mm] C_2 K_l(\kappa_w^n \rho) & \text{for } \rho > \rho_0 \end{cases} \tag{2.42}$$

where the standard Bessel function notation was used. New wavenumber

$$\left(\kappa_{w/d}^n\right)^2 = -\left(k_{w/d}^n\right)^2 \tag{2.43}$$

was introduced which is positive real number for the considered energy interval. The Bessel function of the second kind Y_l and modified Bessel function of the first kind I_l are absent from the solution due to their divergent behavior in corresponding domains. Boundary conditions at $\rho = \rho_0$ are the continuity of radial wavefunction and continuity of its derivative divided by effective mass, and lead to homogeneous system of linear equations in C_1 and C_2 which has a solution if

$$\frac{\kappa_w^n}{m_w} J_l\left(\rho_0 k_d^n\right) \frac{\mathrm{d}}{\mathrm{d}\rho}\left(K_l\left(\rho_0 \kappa_w^n\right)\right) = \frac{k_d^n}{m_d} K_l\left(\rho_0 \kappa_d^n\right) \frac{\mathrm{d}}{\mathrm{d}\rho}\left(J_l\left(\rho_0 k_d^n\right)\right) \tag{2.44}$$

By solving this transcendent equation one obtains the discrete energy spectrum for fixed n and l and those solutions are numbered with index j. The Eq. (2.44) has to be solved in the energy range $\frac{\hbar^2 n^2 \pi^2}{2 m_d h^2} < E < U_b + \frac{\hbar^2 n^2 \pi^2}{2 m_w h^2}$, but further narrowing of this range exists for $l \neq 0$. Taking into account the condition that energies of discrete levels have to be above the minima of effective potential one can show that narrowed energy range for solving the Eq. (2.44) is $\frac{\hbar^2}{2 m_d}\left(\frac{n^2 \pi^2}{h^2} + \frac{l^2}{\rho_0^2}\right) < E < U_b + \frac{\hbar^2 n^2 \pi^2}{2 m_w h^2}$.

Each discrete energy defines the radial wavenumbers $k_{w/d}^{nj}$ and $\kappa_{w/d}^{nj}$ which do not depend explicitly on l (only implicitly, via the solutions for discrete

spectrum). The corresponding radial wavefunctions are

$$
R_{nlj}(\rho) = \begin{cases} C_1 J_l\left(k_d^{nj}\rho\right) & \text{for } \rho < \rho_0 \\ C_1 \dfrac{J_l\left(k_d^{nj}\rho_0\right)}{K_l\left(\kappa_w^{nj}\rho_0\right)} K_l\left(\kappa_w^{nj}\rho\right) & \text{for } \rho > \rho_0 \end{cases}
\tag{2.45}
$$

where the C_1 is determined by normalization.

For the remaining range of energies, i.e. $E > U_b + \frac{\hbar^2 n^2 \pi^2}{2m_w h^2}$ the spectrum is continual and for each energy the corresponding radial wavefunction is

$$
R_{nlE}(\rho) = \begin{cases} C_1 J_l\left(k_d^n \rho\right) & \text{for } \rho < \rho_0 \\ C_2 J_l\left(k_w^n \rho\right) + C_3 Y_l\left(k_w^n \rho\right) & \text{for } \rho > \rho_0 \end{cases}
\tag{2.46}
$$

By using the same boundary and normalization condition one can obtain the constants C_1, C_2 and C_3. There are infinitely many continuum states for any energy counted by quantum number l, in contrast to discrete part of the spectrum where boundary conditions do not allow solutions to exist for values of quantum number l higher than some critical value. Such upper bound to the quantum number l depends also on quantum number n. For increasing value of n, the upper bound of l decreases and eventually there will be no discrete states for some crucial value of quantum number n.

In order to maintain the simplicity, the existence of the BIC by considering only the case with $l = 0$ and $n = 1, 2$ will be demonstrated. The effective potential for the last eigenproblem in Eq. 2.39 is the expression given in brackets. The effective potential for $n = 1$ is $U_{\text{eff}}(\rho) = E_c(\rho) + \Delta U(\rho)$, where $\Delta U(\rho) = \hbar^2 \pi^2 / 2m_e(\rho) h^2$ and for $n = 2$ it is $U_{\text{eff}}(\rho) = E_c(\rho) + 4\Delta U(\rho)$. The effective potential for $l = 0$ and $n = 1, 2$ is given on Fig. 2.5. Note that the effective mass depends only on the radial coordinate since the value of the effective mass in bulk is irrelevant due to

infinite potential.

For $n = 1$ continuum states or quasi-bound well states occur for $E > U_b + \hbar^2 \pi^2 / 2 m_w h^2$. For $n = 2$ bound states might occur for $E < U_b + \hbar^2 2\pi^2 / m_w h^2$, whereas continuum states occur for $E > U_b + 2\hbar^2 \pi^2 / m_w h^2$. Therefore, the excited bound state for $n = 2$ in the well quasi-band continuum for $n = 1$ (above the ionization threshold) might occur at an energy between $U_b + \hbar^2 \pi^2 / 2 m_w h^2 < E < U_b + 2\hbar^2 \pi^2 / m_w h^2$. Note that the first bound states for $l = 0$, $n = 1, 2$ are so called s-like and p-like states.

For the fabricated rods reported in Ref. [1], the In content in the dot and the well is typically 0.45 and 0.16, respectively, and their radius was estimated to be around 5 nm. For such a structure one can extract the value of the dot-well band offset $U_b = 120$ meV, by using the strain effects included as explained in section 2.3. The height of the rods from Ref. [1] is in the range 10-40 nm.

In the following, all energies are referenced to the bottom of the conduction band of the rod material. For the typical rod height of 10 nm, the continuum for $n = 1$ starts at 182 meV, and the p-like bound state for $n = 2$ is below the $n = 2$ continuum, starting at 356 meV. The splitting between s-like ground state and p-like first excited state (which is the BIC) is 200 meV. For the same rod, but with 15 nm height, 2 additional bound states exist, for $l = 0$ and $n = 3$ and 4, which are also embedded in the continuum. There are no discrete states solutions for $l > 0$. By increasing the rod height more bound states in the continuum are obtained, since new bound states with higher values of n appear. However, the energy of all bound states gets lower with increasing the quantum rod height [4], and consequently bound states with the lowest n might sink under the $n = 1$ continuum, ceasing to be BIC. Also, by increasing the rod radius, additional states may appear

with higher value of quantum number l. These states may also become BIC.

Energy diagram of a 10 nm tall rod calculated by 8-band model is presented in Fig. 2.4. Energy diagram clearly show the existence of the BIC. The higher the rod, the higher is the excited dot state embedded in continuum. For the 10 nm tall rod, the splitting between ground state and the bound state in the continuum is 150 meV. Higher value of s-p splitting is due to infinite potential barrier in growth direction which was realistically taken to be finite in 8-band model. In this work we used one-band model with infinite barriers as a default model in order to get insight in physics arguments of the BIC existence.

Hereby, the existence of the bound state in continuum has been demonstrated as a sole consequence of combined well-dot confinement, and for a wide range of structure parameters, especially the adjustable rod height.

Consider now the general case of discrete states with quantum numbers $n = q_n$ and $l = q_l$. Such states can occur in the energy range

$$\frac{\hbar^2}{2m_d}\left(\frac{q_n^2\pi^2}{h^2} + \frac{q_l^2}{\rho_0^2}\right) < E < U_b + \frac{\hbar^2 q_n^2\pi^2}{2m_w h^2}. \tag{2.47}$$

(It is implicitly assumed that q_n and q_l are small enough so $\frac{\hbar^2}{2m_d}\left(\frac{q_n^2\pi^2}{h^2} + \frac{q_l^2}{\rho_0^2}\right) < U_b + \frac{\hbar^2 q_n^2\pi^2}{2m_w h^2}$.) We want to find the conditions for which the continuum with quantum number $n = p$ can embed the given bound state. The continuum with quantum number $n = p$ exists for energies $E > U_b + \frac{\hbar^2 p^2\pi^2}{2m_w h^2}$. Therefore, if $U_b + \frac{\hbar^2 p^2\pi^2}{2m_w h^2} < \frac{\hbar^2}{2m_d}\left(\frac{q_n^2\pi^2}{h^2} + \frac{q_l^2}{\rho_0^2}\right)$, then a bound state with quantum numbers $n = q_n$ and $l = q_l$ can occur in the continuum of quantum number p in the range of energies $\frac{\hbar^2}{2m_d}\left(\frac{q_n^2\pi^2}{h^2} + \frac{q_l^2}{\rho_0^2}\right) < E < U_b + \frac{\hbar^2 q_n^2\pi^2}{2m_w h^2}$.

On the other hand, if $U_b + \frac{\hbar^2 p^2\pi^2}{2m_w h^2} > \frac{\hbar^2}{2m_d}\left(\frac{q_n^2\pi^2}{h^2} + \frac{q_l^2}{\rho_0^2}\right)$ then bound state in the continuum occurs for energies satisfying $U_b + \frac{\hbar^2 p^2\pi^2}{2m_w h^2} < E < U_b + \frac{\hbar^2 q_n^2\pi^2}{2m_w h^2}$.
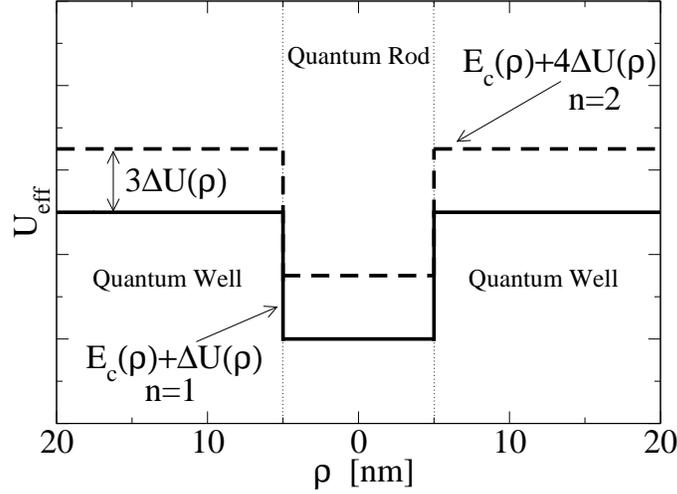
Figure 2.5: Illustration of the energy span where a BIC can occur. The effective potential U_{eff} for the remaining one-dimensional radial eigenproblem is given for $l = 0$ and $n = 1, 2$. For $n = 1$ continuum states or quasi-bound well states occur for $E > U_b + \Delta U$. For $n = 2$ bound states might occur for $E < U_b + 4\Delta U$, whereas continuum states occur for $E > U_b + 4\Delta U$. Therefore the excited bound state in the well quasi-band continuum might occur for energies in the range $U_b + \hbar^2\pi^2/2m_w h^2 < E < U_b + 2\hbar^2\pi^2/m_w h^2$. The Figure has been taken from Ref. 3.

The above consideration shows that BIC occurs for higher values of the quantum number n, i.e. BIC has at least one node in the growth direction. The quantum rod must be sufficiently tall in order to support at least two bound states (s-like and p-like) localized in the dot due to the growth confinement, i.e. with quantum number $n > 0$. With increasing quantum number n, the effective potential $U_{\text{eff}}(\rho) = E_c(\rho) + \Delta U(\rho)$ might become a barrier instead of a well, since $m_d < m_w$. Therefore, the upper bound on a value of n for which BIC exists is imposed $n < \frac{h}{\pi}\sqrt{\frac{U_b}{\hbar^2}\frac{m_w m_d}{m_w - m_d}}$ where m_w and m_d are effective masses of the well and the dot respectively. It can be concluded that confinement in the growth direction has to be stronger than

the confinement in the radial direction caused by the shallower well. At the same time, well subbands may have energies lower than the bulk barrier, opening the possibility that their energy equals the energy of the excited bound state of the dot.

In similar nanostructures, quantum dots in a quantum well (DWELL), this effect does not exist. Conventional quantum dots have very low height to diameter aspect ratio and an excited bound state is guided by the radial confinement, i.e. the excited bound states have nodes in the radial direction and there is no bound state with nodes in the growth direction. Therefore, energy of such an excited state cannot be higher than the well barrier in the radial direction. One thus concludes that quantum rods are unique semiconductor nanostructures with 3D bound state in continuum as a consequence of their distinct features: high value of height-to-diameter aspect ratio and existence of the shallower surrounding well.

In summary, it has been proven that quantum rods can accommodate the excited normalizable state, energetically embedded in the continuum of the subband of the quantum well embedding it, where the electrons can be ionized into. Also, it has been proven that existence of such states is entirely due to the interplay of two different types of confinement, namely the dot 3D confinement and the well confinement in the growth direction. It is worth noting that oversimplified picture of the ideal cylindrical symmetry assumed also plays role of the mandatory condition for the existance of the BIC. The breaking of this symmetry may cause mixing of the bound state with surroundings. In such situation, BIC cease to exist, but the state with high level of localization remains which is the most important property regarding the THz detection purposes. Any kind of external perturbation also couples BIC with surrounding continuum and breaks ideal boundness

of such state. For example phonons might play the role of one such external perturbation.

QRs are unique structures with BIC. As recently realized structures, quantum rods have not been extensively studied experimentally, and interesting dynamical features could arise due to the combined properties of bound and free states.

Chapter 3

Vibrational Structure

Condensed matter systems consist of large number of atoms arranged in the sites of underlying crystal lattices. The entire Bloch theory of bulk materials and all electronic structure models for heterostructure materials rely on the fact that constituent atoms are fixed at the sites. This, however, is not true since atoms are bound between each other by elastic forces able to move accordingly. This gives rise to the vibrational spectra of all condensed matter materials. This vibrational movement can be modeled as a large number of entangled harmonic oscillators. Quantization of these oscillator modes gives rise to the phonons. Phonons cause further physical properties of quantum dots to a great extend. Phonons in any condensed matter system influence its thermal properties such as heat conductivity [121]. However, phonons influence the optoelectronic properties of quantum dots as well, mainly through the electron-phonon interaction. The main aim of this chapter is to present models of obtaining the phonon spectra in semiconductor heterostructures and to present models of electron-phonon interaction. In this way, electron and phonons are two main types of particles in quantum dots governing their optoelectronic properties.

Standard models of vibrational structure in solids are readily divided into two big groups. The first group of models is based on microscopic consideration of ion displacements as a displacements of each ion separately $\boldsymbol{u}^{\mu}\left(\boldsymbol{R}\right)$ [121] where $\boldsymbol{R}$ is position of lattice site and superscript μ denotes position of the μ-th atom within the unit cell for lattices with the basis. Such approach is feasible only to the bulk case due to crystal symmetry of the bulk. SAQDs are embedded within the host, bulk semiconducting material of the same crystal lattice type as the dot itself. The lattice type of the entire structure remains the same and only strain could arise due to lattice constant mismatch. Therefore, bulk model for phonons can be applied to study vibrational structure of SAQDs and it is done so in this thesis.

However, when it comes to CQDs, bulk model cannot be applied since nanocrystals are usually embedded within the host insulating material, different from the semiconducting material of the nanocrystal. For such case it is better to use continuum models where ion displacement is considered as continuum field $\boldsymbol{u}^{\mu}\left(\boldsymbol{r}\right)$ which can be determined by the classical continuum mechanics and electromagnetism approach. Furthermore, continuum models are easily adjusted to the case of small nanocrystals giving the confined phonon modes.

Regardless of the model used, two main types of vibrational modes exist in solids, namely optical and acoustical modes [121]. These types of modes arise directly through the consideration of phonon modes in bulk materials [121]. Continuum models are more empirical and are adjusted to each group of modes. For optical modes of polar semiconductors one can apply dielectric continuum model and for acoustic modes of all semiconductors elastic continuum model.

The contribution of this chapter reflects in applying the continuum mod-

els in order to obtain discrete phonon spectra in CQDs. It turns out that the strength of the coupling (the strongest coupling comes from longitudinal optical phonons) is significant enough that formation of polarons takes place and that will be further studied in the last chapter.

Beside this contribution, the bulk model of phonon modes in SAQDs will be used in order to demonstrate formation of polarons in SAQDs. By using such polaron picture, one can explain the absence of the bottleneck effect predicted in SAQDs. Results of this consideration will be further used in the fourth chapter of the thesis where the connection between the non-radiative lifetime due to electron-phonon interaction and optical matrix element will be demonstrated.

3.1 Bulk Phonon Modes in SAQDs

Detailed consideration of bulk phonon modes is given in Ref. 121. Phonons in bulk are divided into acoustical and optical and each of these groups contains two branches of transversal and branch of longitudinal modes for the case of solids with diatomic basis of the unit cell which are solely considered in this thesis. Displacement for each site $\boldsymbol{R}$, basis atom μ and phonon mode with wavevector $\boldsymbol{k}$ from a branch s is given as

$$\boldsymbol{u}_{s,\boldsymbol{k}}^{\mu}(\boldsymbol{R}) = \frac{1}{\sqrt{N}} \boldsymbol{\epsilon}_s^{\mu}(\boldsymbol{k}) \, e^{i\boldsymbol{k}\cdot\boldsymbol{R}}, \tag{3.1}$$

where $\boldsymbol{\epsilon}_s^{\mu}(\boldsymbol{k})$ is polarization vector for mode with wavevector $\boldsymbol{k}$ from the branch s and N is the number primitive cells in the bulk material. Polarization vectors obey orthonormality relation:

$$\sum_{\mu} \boldsymbol{\epsilon}_s^{\mu}(\boldsymbol{k}) \cdot \boldsymbol{\epsilon}_{s'}^{\mu*}(\boldsymbol{k}) = \delta_{s,s'}, \tag{3.2}$$

and completeness relation:

$$\sum_s \epsilon_{s,i}^{\mu}\left(\boldsymbol{k}\right) \cdot \epsilon_{s',j}^{\nu*}\left(\boldsymbol{k}\right) = \delta_{i,j}\delta_{\mu,\nu}, \tag{3.3}$$

where subscripts i and j denote Cartesian components of corresponding vectors. Therefore, all modes are mutually orthonormalized:

$$\sum_{\boldsymbol{R},\mu} u_{s,\boldsymbol{k}}^{\mu}\left(\boldsymbol{R}\right) \cdot u_{s',\boldsymbol{k}'}^{\mu}\left(\boldsymbol{R}\right) = \delta_{s,s'}\delta_{\boldsymbol{k},\boldsymbol{k}'}. \tag{3.4}$$

Second quantization starts with introduction of annihilation and creation operators instead of the displacement and momentum operators of each ion:

$$\hat{\boldsymbol{u}}^{\mu}\left(\boldsymbol{R}\right) = \sum_{s,\boldsymbol{k}} \sqrt{\frac{\hbar}{2M_{\mu}\Omega_{s,\boldsymbol{k}}}}\left(\hat{a}_{\boldsymbol{k},s} + \hat{a}_{-\boldsymbol{k},s}^{\dagger}\right)\boldsymbol{u}_{s,\boldsymbol{k}}^{\mu}\left(\boldsymbol{R}\right), \tag{3.5}$$

and

$$\hat{\boldsymbol{p}}^{\mu}\left(\boldsymbol{R}\right) = -i\sum_{s,\boldsymbol{k}} \sqrt{\frac{\hbar M_{\mu}\Omega_{s,\boldsymbol{k}}}{2}}\left(\hat{a}_{\boldsymbol{k},s} - \hat{a}_{-\boldsymbol{k},s}^{\dagger}\right)\boldsymbol{u}_{s,\boldsymbol{k}}^{\mu}\left(\boldsymbol{R}\right). \tag{3.6}$$

where M_{μ} denotes mass of the μ-th ion in the polar bulk and $\Omega_{s,\boldsymbol{k}}$ denotes frequency of the bulk mode $\boldsymbol{k}$ In terms of new operators Hamiltonian reads as [121]

$$\hat{H} = \sum_{s,\boldsymbol{k}} \hbar\Omega_{s,\boldsymbol{k}}\left(\hat{a}_{s,\boldsymbol{k}}^{\dagger}\hat{a}_{s,\boldsymbol{k}} + \frac{1}{2}\right). \tag{3.7}$$

It is very difficult to entirely model the vibrational structure of bulk material in this way since the eigenproblem of the motion equation of all atoms is untrackable. Therefore, dispersion curves for frequencies $\Omega_{s,\boldsymbol{k}}$ are readily directly measured from experiments and up to date, these branches are very precisely obtained in the literature for all solids of interest. Acoustic modes have linear-like behavior, whereas optical modes are nearly constant, especially in the vicinity of Gamma point [121]. In polar semiconductors, LO

branch is split from other optical branches (transversal). This is because longitudinal propagation of the phonon wave couples with polarization field produced by the same mode. This issue will be addressed in sections regarding the continuum models.

3.1.1 Electron-Phonon Interaction in Bulk

The electron-phonon interaction can be examined within the scope of presented bulk model. However, empirical assumption is made that conducting carriers, electrons and holes, for which carrier-phonon interaction is examined are free from ions, and all other electrons from lower bands are considered as bound to ions. The exact nature of coupling will be considered later. One can write down the full Hamiltonian of the system having one conduction electron, ion with non-conductive electronic shell core and their mutual interaction [122]:

$$H = \frac{p^2}{2m_0} + H_{ph} + \sum_{\boldsymbol{R}^\mu} V_{ei}^\mu (\boldsymbol{r} - \boldsymbol{R}^\mu), \tag{3.8}$$

where the terms on the right hand side of equation are kinetic energy of electron, harmonic vibrational potential of the lattice and lattice-electron interaction respectively.

Ions are numbered with $\boldsymbol{R}^\mu$ where $\boldsymbol{R}$ accounts for each cell and μ accounts for each subcell, i.e. each type of ion in lattice with basis such as for diatomic polar compounds, materials of interest in this thesis. Two ions numbered with μ contained within that cell are positioned at $\boldsymbol{R}^\mu = \boldsymbol{R} + \boldsymbol{d}_\mu$.

As already labeled, bulk model of phonons will be used for the case of SAQDs, which are predominantly made of semiconductors with zincblende symmetry. Therefore, it will be assumed that $\boldsymbol{d}_1 = 0$, i.e. $\boldsymbol{R}^1 = \boldsymbol{R}$ and

$d_2 = \frac{a}{4}(1,1,1)$, i.e. $\boldsymbol{R}^2 = \boldsymbol{R} + \frac{a}{4}(1,1,1)$ which corresponds to statement that zinc-blende crystal structure is obtained by duplicating face-centered cubic lattice and translating the duplicate along diagonal for one fourth of that diagonal.

Exact position of each "rigid" ion is $\boldsymbol{r} = \boldsymbol{R}^\mu + \boldsymbol{u}^\mu(\boldsymbol{R})$. Potential interaction between each ion and electron can be expanded in Taylor series restricted to the second order:

$$V_{ei}^\mu \left(\boldsymbol{r} - \boldsymbol{R}^\mu - \boldsymbol{u}^\mu(\boldsymbol{R})\right) = V_{ei}^\mu \left(\boldsymbol{r} - \boldsymbol{R}^\mu\right) + \qquad (3.9)$$

$$+ \left(\boldsymbol{u}^\mu(\boldsymbol{R}) \cdot \nabla\right) V_{ei}^\mu \left(\boldsymbol{r} - \boldsymbol{R}^\mu\right) +$$

$$+ \frac{1}{2} \left(\boldsymbol{u}^\mu(\boldsymbol{R}) \cdot \nabla\right)^2 V_{ei}^\mu \left(\boldsymbol{r} - \boldsymbol{R}^\mu\right) + ...,$$

where the first term on the right hand side is periodic crystal potential which gives rise to the band electronic structure or in the case of heterostructures envelope functions band electronic structure:

$$H_e = \frac{p^2}{2m_0} + \sum_{\boldsymbol{R},\mu} V_{ei}^\mu \left(\boldsymbol{r} - \boldsymbol{R}^\mu\right), \qquad (3.10)$$

and all remaining terms represent electron – phonon interaction Hamiltonian:

$$H_{e-ph} = H_{e-ph}^{(1)} + H_{e-ph}^{(2)} + ..., \qquad (3.11)$$

where

$$H_{e-ph}^{(1)} = \sum_{\boldsymbol{R},\mu} \left(\boldsymbol{u}^\mu(\boldsymbol{R}) \cdot \nabla\right) V_{ei}^\mu \left(\boldsymbol{r} - \boldsymbol{R}^\mu\right), \qquad (3.12a)$$

$$H_{e-ph}^{(2)} = \frac{1}{2} \sum_{\boldsymbol{R},\mu} \left(\boldsymbol{u}^\mu(\boldsymbol{R}) \cdot \nabla\right)^2 V_{ei}^\mu \left(\boldsymbol{r} - \boldsymbol{R}^\mu\right). \qquad (3.12b)$$

Only linear term will be considered in the thesis whereas consideration of the

quadratic term can be done as well. However, it is expected that quadratic term is of several order of magnitudes weaker then linear term.

Linear Electron-Phonon Interaction Term

The first term on right hand side of (3.11) is linear in ion displacement. Firstly, one has to expand the electron ion interaction in Fourier series

$$V_{ei}^{\mu}\left(\boldsymbol{r} - \boldsymbol{R}^{\mu}\right) = \frac{1}{N} \sum_{\boldsymbol{q}} V_{\boldsymbol{q}}^{\mu} e^{i\boldsymbol{q}\cdot(\boldsymbol{r}-\boldsymbol{R}^{\mu})}, \tag{3.13}$$

where $V_{\boldsymbol{q}}^{\mu}$ is Fourier component of electron-ion interaction.

Putting (3.5) and (3.13) in (3.12a) and taking into account that

$$\sum_{\boldsymbol{R}} e^{i\boldsymbol{q}\cdot\boldsymbol{R}} = \begin{cases} N & \text{if } \boldsymbol{q} \text{ reciprocal lattice vector} \\ 0 & \text{if } \boldsymbol{q} \text{ not a reciprocal lattice vector}, \end{cases} \tag{3.14}$$

one obtains:

$$H_{e-ph}^{(1)} = \sum_{\boldsymbol{k},s} M_{\boldsymbol{k},s}\left(\boldsymbol{r}\right)\left(\hat{a}_{\boldsymbol{k},s} + \hat{a}_{-\boldsymbol{k},s}^{\dagger}\right) e^{i\boldsymbol{k}\cdot\boldsymbol{r}}, \tag{3.15}$$

where

$$M_{\boldsymbol{k},s}\left(\boldsymbol{r}\right) = \frac{i}{\sqrt{N}} \sum_{\boldsymbol{G},\mu} \sqrt{\frac{\hbar}{2\omega_{\boldsymbol{k},s}M_{\mu}}} \left(\boldsymbol{k}-\boldsymbol{G}\right)\cdot\boldsymbol{\epsilon}_{s}^{\mu}\left(\boldsymbol{k}\right) V_{\boldsymbol{k}-\boldsymbol{G}}^{\mu} e^{i\boldsymbol{G}(\boldsymbol{d}_{\mu}-\boldsymbol{r})}, \tag{3.16}$$

and $\boldsymbol{G}$ represents reciprocal lattice vector, i.e. $e^{i\boldsymbol{G}\cdot\boldsymbol{R}} = 1$ for each $\boldsymbol{R}$ and $\boldsymbol{G}$.

Due to product $\boldsymbol{k}\cdot\boldsymbol{\epsilon}_{s}^{\mu}\left(\boldsymbol{k}\right)$, dominant terms stem from longitudinal modes. In principle Fourier components (3.13) contain two main types of forces towards electrons: short-range and long-range electrostatic forces, i.e. $V_{\boldsymbol{k}}^{\mu} = V_{\text{short}}^{\mu}(\boldsymbol{k}) + V_{\text{long}}^{\mu}(\boldsymbol{k})$. Coefficients (3.16) are non-trackable using ab-initio physics, but one must approach problem semi-empirically. Outcome of such

approach is briefly summarized in what follows.

- **Long range forces and polar coupling to LO phonons**.

  In principle, nuclei charge causes Coulomb type of potential which acts
  on all electrons. However, realistic situation is quite more complicated.
  Non-conductive electrons bound to ion are following the nuclei in their
  movement. Thus, one conduction electron feels screened Coulomb po-
  tential which is practically zero potential for non-polar semiconductors
  such as Si or Ge. In polar compounds such as III-V compounds there
  is net charge transfer from one ion to another which gives rise to ef-
  fective dipole moment which can be felt from other remote electrons.
  Therefore, one has to consider effective Coulomb electrostatic poten-
  tial between conductive electron and ion-bound-electrons system with
  Fourier component

  $$V_{\text{long}}^{\mu}(\boldsymbol{k}) = \frac{(-1)^{\mu}\beta}{k^2} \tag{3.17}$$

  where factor $(-1)^{\mu}$ comes due to the fact that different ions within the
  same unit cell carry opposite charge. Factor β is just suitable factor
  of proportionality which carries information on microscopic nature of
  coupling beyond present scope. For example it carries information on
  geometrical structure of ion, screening effects and net charge caused
  by transfer from second ion in the primitive cell of polar compounds.

  The dominant terms in effective Coulomb electrostatic potential come
  from long wavelengths modes fro small $\boldsymbol{k}$. Therefore, Fourier compo-
  nents $V_{\text{long}}^{\mu}(\boldsymbol{k} - \boldsymbol{G})$ are assumed to be significant only for $G = 0$.

  For LO modes one can approximately write $\boldsymbol{k} \cdot \boldsymbol{\epsilon}_{\text{LO}}^{\mu}(\boldsymbol{k}) = (-1)^{\mu}k \left|\boldsymbol{\epsilon}_{\text{LO}}^{\mu}\right|$
  since different ions within the same unit cell oscillate in opposite di-
  rections. This also means that only LO modes significantly couple

to electrons via long range forces. Optical phonons are nearly dispersionless and for simplicity, a constant LO phonon energy ω_{LO} is assumed. With all that, coefficients (3.16) for the electron-LO phonon interaction via short range forces read as

$$M_{\boldsymbol{k}} = \frac{i}{\sqrt{N}} \sqrt{\frac{\hbar}{2\omega_{LO}}} \frac{1}{k} \beta \sum_{\mu} \frac{|\epsilon_{\mathrm{LO}}^{\mu}|}{\sqrt{M_\mu}} \qquad (3.18)$$

This type of interaction is readily seen as charged dipoles oscillating in opposite directions creating an effective electric field that electrons interact with. Again, only LO phonons create this potential.

Another expression for the coefficients (3.16) can be obtained from dielectric continuum model. Dielectric continuum model will be introduced later in this chapter. It can be applied to any semiconductor heterostructure and to a bulk as well. The bulk result is very well known and it is given as [123]:

$$M_{\boldsymbol{k}} = \frac{1}{k} \sqrt{\frac{e^2 \hbar \omega_{\mathrm{LO}}}{2V} \left(\frac{1}{\varepsilon_\infty} - \frac{1}{\varepsilon_{st}} \right)}, \qquad (3.19)$$

ε_∞ and ε_{st} are high frequency and static dielectric constants, respectively. This expression will be further used in the thesis.

Now it is possible to relate microscopic conductive electron-ion potential and macroscopic measurable dielectric parameters:

$$\beta \sum_{\mu} \frac{|\epsilon_{\mathrm{LO}}^{\mu}|}{\sqrt{M_\mu}} = -ie\omega_{LO} \sqrt{\frac{N}{V} \left(\frac{1}{\varepsilon_\infty} - \frac{1}{\varepsilon_{st}} \right)}. \qquad (3.20)$$

This connection can be utilized in the pseudopotential theory of solids as it gives Coulomb contribution for polar compounds to the pseu-

dopotentials for the conductive electrons in terms of experimentally measurable static and high frequency dielectric constants.

- **Short range forces and deformation potential coupling to acoustic phonons**.

Short range forces account for entire interaction except for Coulomb-like interaction between conductive electron and ion with all bound electrons. For example, Pauli exclusion principle does not allow conductive electron to approach near it due to fermionic repulsion with bounded electrons of the ion. The most important feature of short range forces is that they act repulsively onto the conductive electron in vicinity of the ion. Therefore, short range potential contains delta-like singularity near the ion. Also, those forces are approximately the same for all types of ions within the unit cell.

Since the microscopic nature of short range interactions is very complex, the Eq. (3.15) cannot be further simplified as it was done for long range Coulomb type of interaction. Instead, it is easier to observe acoustic vibrations as time varying strain field. As explained in Chapter 2 strain induces additional potential to the electrons and that is the basis for consideration of electron-acoustic phonon interaction.

Deformation potential coupling is coupling of electron with strain-disordered crystal due to phonon oscillations. Note that only acoustic phonons produce the strain similar to the strain considered in Chapter 2. Optical phonons modes have very different displacement patterns (opposite oscillations of adjacent atoms in the same unit cell) and therefore cannot be considered as time dependent strain introduced in Chapter 2. The dominant term in deformation coupling is

proportional to divergence of displacement field [124]. This can be also seen through corrections of diagonal elements of the $\boldsymbol{k} \cdot \boldsymbol{p}$ matrix due to strain (see Sec. 2.1.3). Electron-acoustic phonon coupling will be considered only within the effective mass model in this thesis. Therefore, relevant Hamiltonian correction matrix elements in Sec. 2.1.3 are those defined in Eq. (2.28), i.e. D_{cc}^0 (c denotes the conduction band). They are given as [90, 97]

$$D_{\text{cc}}^0 = E_d(e_{xx} + e_{yy} + e_{zz}) \tag{3.21}$$

where so called deformation potential coupling constant for the conduction band is defined as:

$$E_d = \left\langle u_{\text{c0}} \left| \frac{\hat{p}_i \hat{p}_i}{m_0} + \frac{\partial V_0(\boldsymbol{r})}{\partial x_i} x_i \right| u_{\text{c0}} \right\rangle \tag{3.22}$$

This expression for the coupling relies upon the assumption that strain is homogeneous. However, time dependent strain induced by the acoustic phonons is not generally homogeneous in space. However, the modes of the interest are the long wavelength phonons since they are the only ones coupling to confined carriers. Therefore, induced strain close to the confined electron can be considered as homogeneous and proposed form of coupling is then justified.

By using the expression for ion displacement for bulk phonons (3.5) together with linearly approximated dispersion curve for LA modes $\omega_{\boldsymbol{k},\text{LA}} = c_{\text{LA}}k$ and by using the alignment pattern for LA modes $\boldsymbol{k} \cdot$

$\epsilon_{LA}^{\mu}(\boldsymbol{k}) = k \left| \epsilon_{\mathrm{LA}}^{\mu} \right|$ one finally obtains:

$$M_{\boldsymbol{k}} = \sqrt{\frac{E_d^2 \hbar k}{2 \rho c_{\mathrm{LA}} V}}. \tag{3.23}$$

- **Piezoelectric coupling to acoustic phonons**.

  As already discussed, acoustic phonons can be considered as time dependent induced strain in crystals. Strain also induces piezoelectric polarization field in crystals lacking inversion symmetry. Such polarization induces electrostatic potential for carriers and that is origin of piezoelectric coupling of carriers to acoustic phonons. Within the bulk model the strength of piezoelectric coupling scales with $\sim 1/\sqrt{q}$, in contrast to deformation potential interaction where it scales as $\sim \sqrt{q}$. Therefore, for sufficiently large energy spacing (greater then 10 meV), typically present in quantum nanostructures, deformation potential coupling to acoustic phonons is much stronger than piezoelectric coupling and therefore piezoelectric coupling to acoustic phonons will be neglected in the bulk model. However, for the case of CQDs, piezoelectric field will be taken into account.

3.1.2 Formation of Polarons in SAQDs

Dynamics of carriers in QDs is of great importance for optoelectronic applications of QDs. As explained in Sec. 1.4.2, optical transitions between discrete QD levels can be used for optoelectronic applications and long non-radiative lifetime is required for radiative transition to take place. Electron–phonon interaction, if treated perturbatively does not yield agreement with finite non-radiative lifetimes of excited electrons to the experimentally measured values. However, if problem of electron-phonon interaction is treated

in strong coupling regime then formation of polarons takes place and within such picture it is possible to provide theoretical explanations of the short non-radiative lifetimes measured in experiments. In this section, simple theoretical model will be introduced in order to demonstrate formation of polarons in QDs.

In terms of vibrational structure, SAQDs can be seen as slightly disordered bulk lattice due to presence of the dot material which has the same lattice type as the surrounding bulk material. Therefore, introduced bulk model for phonons can be used in order to simulate vibrational structure of SAQDs together with electron-phonon interaction. The strongest interaction is the interaction with LO phonon modes. Electron wavefunctions of bound states in SAQDs are confined. Because of that bound electron-phonon interaction in quantum dots is significantly increased. These facts are the first indicator that electron-LO phonon interaction in SAQDs assigned to bound states cannon be treated perturbatively, but instead full diagonalization of electron-phonon Hamiltonian should be done. This gives rise to polaron bound states in SAQDs. Entire intraband physics should be then considered within the polaron picture.

As said in Chapter 1 detailed examination of non-radiative relaxation mechanisms in SAQDs is needed in order to study and design SAQDs for possible intraband lasing applications. The best way to study these properties is to take the SAQD out of thermodynamic equilibrium by light pulse and to study evolution of a excited state by pump-probe technique [61].

The main source of non-radiative transitions must come from the electron-phonon coupling. As already outlined and indicated in Chapter 1, the most recent understanding is that dominant electron-phonon interaction, i.e. Fröhlich interaction of electrons and longitudinal optical (LO) phonons

couples electrons and LO phonons strongly [125, 57] and thus polarons in SAQDs occur. Detailed theoretical demonstration of such effect follows, manly by following the Ref. 60.

The full Hamiltonian to be considered accounts for the Fröhlich coupling between electrons and LO phonons, i.e.:

$$H = H_{\mathrm{e}} + H_{\mathrm{ph}} + \sqrt{\frac{e^2 \hbar \omega_{\mathrm{LO}}}{2V} \left(\frac{1}{\epsilon_\infty} - \frac{1}{\epsilon_{st}} \right)} \sum_{ij\boldsymbol{k}} \mathcal{H}_{ij}^{\boldsymbol{k}} \hat{a}_i^+ \hat{a}_j \left(\hat{b}_{\boldsymbol{k}} + \hat{b}_{-\boldsymbol{k}}^+ \right) \quad (3.24)$$

where H_{e} is the electronic part of the Hamiltonian, H_{ph} is the phonon part of the Hamiltonian, $\hat{b}_{\boldsymbol{k}}$ and $\hat{b}_{\boldsymbol{k}}^+$ are phonon annihilation and creation operators and $\hat{a}_i$ and $\hat{a}_j^+$ are the corresponding operators for electrons. It has been argued that one has to diagonalize this full Hamiltonian in order to obtain agreement with results obtained in magneto-optical experiments [57, 58, 56].

The diagonalization procedure from Ref. 60 has been adopted here. The Hamiltonian, equation (3.24), commutes with the electron number operator $\hat{N}$ and, therefore can be solved in each subspace for a constant number of electrons. Therefore, the one-electron limitation is introduced here together with the two-level system having an s-like ground state and first p-like excited state as explained in Chap 1.

The eigenstates of the trivial case of the Hamiltonian without electron–phonon interaction is a simple uncorrelated eigenbasis formed by the direct product of a pure electronic eigenstates and pure phonon eigenstates. When it comes to the full Hamiltonian, as it has been proved in Refs. 58 and 60, only a finite number of LO modes couples with a finite number of electronic states in the non-dispersive phonon modes approximation. The limitation is introduced to a two level electronic system. Those electronic states will be further labeled with $|\psi_a\rangle$ and $|\psi_b\rangle$, or shortly $|a\rangle$ and $|b\rangle$, with energies

E_a and E_b.

For two-level electronic systems only three LO modes are considered (These modes are not bulk-like and are properly defined via expansion in bulk LO phonon modes near band edge which only significantly couple to carriers and can be also considered as non-dispersive). Their further orthonormalization [126] and proper unitary rotation gives three new modes which are coupled to a two-level system with one electron. Only one mode couples the s-p resonant transition to the classical emission or absorption of one phonon and will be denoted as B_1. The second mode couples the s-p resonant transition with the self-translation which gives rise to the Franck-Condon factors [60]. It will be denoted as $B_2^\gamma = B_2 + \gamma$ where the parameter γ represents translation. The third mode is properly translated, so it does not couple to the resonant s-p transition in the one-electron case and can be omitted from further consideration.

Further space reduction was obtained in Ref. 60 by introducing the rotating wave approximation, by choosing only the coupling states differing by the detunings $\delta_\pm = E_b - E_a \pm \hbar\omega_{\mathrm{LO}}$. The first state has the electron in state b and "certain phonon configuration". The second state has the electron in state a and the same phonon configuration, with only one additional phonon in mode B_1 and "translated" mode B_2^γ with the same occupation number. The relationship between these translated and initial modes is determined by general Franck-Condon factors. By neglecting the polaronic shifts terms, it is possible to obtain approximate analytical solution of any such 2×2 Hamiltonian. Thus, the basis considered is:

$$\left|2'\right\rangle = \left|b; n_1^0; n_2^\gamma\right\rangle,$$
$$\left|3'\right\rangle = \left|a; n_1^0 + 1; n_2^0\right\rangle.$$

where $n_1 = n_2 = 0$. We additionally take two adjacent states into account, namely the ground state a with zero phonons (i.e. uncorrelated ground state) and its coupling state b with one phonon in mode B_1 and the "translated" mode B_2^γ with the same occupation number:

$$\left|1'\right\rangle = \left|a; n_1^0; n_2^0\right\rangle,$$
$$\left|4'\right\rangle = \left|b; n_1^0 + 1; n_2^\gamma\right\rangle.$$

The superscript at the phonon modes denotes translation of the mode from the bulk one. This is relevant only for the second phonon mode since translated mode $B_2^\gamma = B_2 + \gamma$ couples to the electron in the excited state b only. Enumeration of the basis states is made to order the states according to their increasing energy, i.e. we consider the case where the detuning is $\delta_- < 0$.

The solution of this model is also given in Ref. 60 and it reads:

$$\left|1\right\rangle = \sqrt{\frac{1}{2}\left(1 - \frac{\delta_+}{R_+}\right)}\left|4'\right\rangle + \sqrt{\frac{1}{2}\left(1 + \frac{\delta_+}{R_+}\right)}\left|1'\right\rangle,$$
$$\left|2\right\rangle = \sqrt{\frac{1}{2}\left(1 - \frac{\delta_-}{R_-}\right)}\left|2'\right\rangle - \sqrt{\frac{1}{2}\left(1 + \frac{\delta_-}{R_-}\right)}\left|3'\right\rangle,$$
$$\left|3\right\rangle = \sqrt{\frac{1}{2}\left(1 + \frac{\delta_-}{R_-}\right)}\left|2'\right\rangle + \sqrt{\frac{1}{2}\left(1 - \frac{\delta_-}{R_-}\right)}\left|3'\right\rangle,$$
$$\left|4\right\rangle = \sqrt{\frac{1}{2}\left(1 + \frac{\delta_+}{R_+}\right)}\left|4'\right\rangle - \sqrt{\frac{1}{2}\left(1 - \frac{\delta_+}{R_+}\right)}\left|1'\right\rangle,$$

where $R_+ = \sqrt{\delta_+^2 + 4\left|F_n^\gamma C_{\mathrm{ab}}\right|^2}$ and $R_- = \sqrt{\delta_-^2 + 4\left|F_n^\gamma C_{\mathrm{ab}}\right|^2}$ are the Rabi splittings, while $F_n^\gamma = \langle n|n\rangle_\gamma$ is the Franck-Condon factor and C_{ab} is a

normalization constant used to normalize the mode B_1 and it reads as

$$C_{\mathrm{ab}} = \frac{e^2 \hbar \omega_{\mathrm{LO}}}{16\pi^3} \left(\frac{1}{\epsilon_\infty} - \frac{1}{\epsilon_{st}} \right) \int \mathrm{d}^3 \boldsymbol{k} \left| \mathcal{H}_{\mathrm{ab}}^{\boldsymbol{k}} \right|^2 \tag{3.25}$$

and will be further referred to as the Fröhlich coupling constant. If one assumes zero energy of the state $|1'\rangle$ the eigenenergies of this polaron model are:

$$
\begin{aligned}
E_1 &= \frac{1}{2} \left(\delta_+ - R_+ \right), \\
E_2 &= \frac{1}{2} \left(\delta_+ - R_- \right), \\
E_3 &= \frac{1}{2} \left(\delta_+ + R_- \right), \\
E_4 &= \frac{1}{2} \left(\delta_+ + R_+ \right),
\end{aligned}
$$

In conclusion to this section, the most important quantity, directly responsible for formation of the coherent polaron modes, is the Fröhlich coupling constant C_{ab}.

Therefore, the polaron problem consisting of two electron states, one electron and LO phonon modes has been solved exactly. These polaron states will be further used in order to examine carrier relaxation as polaron relaxation in SAQDs due to anharmonicity of crystal lattice.

3.1.3 Anharmonicity Driven Polaron Scattering

Phonons present quantized form of crystal lattice vibrations arising from harmonic approximation, i.e. under assumption that additional potential coming from lattice movement is proportional to squared displacements. Beyond this approximation, one can include anharmonicity terms. Anhar-

monicity forces enable energy exchange between modes, thus maintaining the thermodynamical equilibrium. The most dominant anharmonicity term considered in the literature is qubic term and it was taken into accoun perturbatively [127, 128, 129] to calculate non-equilibrium lifetimes of longitudinal optical phonons.

It is still an issue in which modes it is possible for longitudinal optical mode to decay into. In Ref. [128] possible channels are briefly summarized. Theoretically, it has been proposed in Ref. [127] that decaying occurs in two acoustical modes which is called Klemens channel. Experimentally, it has been measured in Ref. [130] that Klemens channel is not dominant one and instead of it authors introduced channel with decaying into one Brillouin zone edge optical phonon and transversal acoustical phonon. For GaN in [131] decaying into transverse optical and longitudinal acoustical has been considered.

However, there is no strong consensus in literature about the particular decaying channel. In this thesis it will be assumed that non-equlibrium longitudinal phonons decay in acoustic phonons with the aim to develop a empirical model which does not take into account detailed microscopical nature of decaying, but will only hold to account for experimental results of polaron decaying processes.

Anharmonicity of the crystal lattice can trigger the nonequilibrium polaron decaying. Referring to [129], anharmonicity perturbation Hamiltonian

is of the form

$$V_a = \frac{\Omega}{3!\sqrt{N}} \left(\frac{\hbar}{2M} \right)^{\frac{3}{2}} \times \tag{3.26}$$

$$\times \sum_{\boldsymbol{k},s,\boldsymbol{k}',s',\boldsymbol{k}'',s''} \frac{P\left(\boldsymbol{k},s;\boldsymbol{k}',s';\boldsymbol{k}'',s''\right)}{\sqrt{\omega_{\boldsymbol{k},s}\omega_{\boldsymbol{k}',s'}\omega_{\boldsymbol{k}'',s''}}} \delta_{\boldsymbol{k}+\boldsymbol{k}'+\boldsymbol{k}''} \times$$

$$\times \left(\hat{b}_{\boldsymbol{k},s} + \hat{b}^\dagger_{-\boldsymbol{k},s} \right) \left(\hat{b}_{\boldsymbol{k}',s'} + \hat{b}^\dagger_{-\boldsymbol{k}',s'} \right) \left(\hat{b}_{\boldsymbol{k}'',s''} + \hat{b}^\dagger_{-\boldsymbol{k}'',s''} \right) \tag{3.27}$$

where constants $P\left(\boldsymbol{k},s;\boldsymbol{k}',s';\boldsymbol{k}'',s''\right)$ are presenting strength of inter-modal anharmonic coupling and following [132], which extends [127] one can use

$$\left| P\left(\boldsymbol{k},s;\boldsymbol{k}',s';\boldsymbol{k}'',s''\right) \right| = \frac{2\rho\gamma}{c_a} \omega_{\boldsymbol{k},s}\omega_{\boldsymbol{k}',s'}\omega_{\boldsymbol{k}'',s''} \tag{3.28}$$

where γ is mode-averaged Gruneisen constant and c_a is mode-averaged acoustic phonon speed.

Once the polaron states are obtained it will be possible to find anharmonicity driven transition rates from one polaron state to another using Fermi golden rule and perturbation Hamitlonian (3.26).

3.1.4 Non-Radiative Polaron Lifetime

After excitation, the relaxation of non-equilibrium polarons is enabled by anharmonic perturbation of the crystal. So far, this has been the most reliable theoretical explanation of the finite excited carrier lifetime proposed in Ref. 133. This potential acts only on the phonon factor in the polaron state. Besides the zero-phonon component in the excited polaron state, there is also a one-phonon component responsible for non-radiative relaxation of the excited polaron due to crystal anharmonicity potential. Therefore, the non-radiative decay rate has to be proportional to the absolute squared value

of the weights of the relevant components:

$$\Gamma\left(E_i\right) = \frac{1}{4}\Gamma_{\mathrm{ph}}\left(E_i\right)\left(1 + \frac{\delta_+}{R_+}\right)\left(1 + \frac{\delta_-}{R_-}\right) \tag{3.29}$$

The quantity $\Gamma_{\mathrm{ph}}\left(E_i\right)$ represents the bare decay rate of phonons which would have polaron energies driven by anharmonicity potential:

$$\Gamma_{\mathrm{ph}}\left(E_i\right) = \frac{2\pi}{\hbar}\sum_j \left|\langle j|\, V_a\, |3'\rangle\right|^2 \tag{3.30}$$

The summation is performed over all possible decay channels of mode B_1 with one phonon. Detailed discussion on decay channels and the derivation of analytical expression for $\Gamma_{\mathrm{ph}}\left(E_i\right)$ can be found in Ref. 133.

It was pointed out in Ref. 61 that a strong inhibition of this mechanism occurs at lower values of the energy splitting between the electronic ground and excited states. In other words, the squared detuning δ_-^2 becomes significantly larger than the squared Fröhlich coupling constant, leading to a simplified linearized ratio of detuning and Rabi splitting:

$$1 + \frac{\delta_-}{R_-} \approx 2\frac{|F_n^\gamma C_{\mathrm{ab}}|^2}{\delta_-^2} \tag{3.31}$$

Furthermore, by using an additional approximation $\frac{\delta_+}{R_+} \approx 1$ and $F_n^\gamma \approx 1$, which holds for small values of the parameter γ, one can write:

$$\Gamma\left(E_i\right) = \Gamma_{\mathrm{ph}}\left(E_i\right)\frac{|C_{\mathrm{ab}}|^2}{\delta_-^2} \tag{3.32}$$

Therefore, the Fröhlich coupling constant is inversely proportional to the lifetime of the excited carrier in the quantum dot. It will be demonstrated in next chapter that the same Fröhlich coupling constant can be linearly

related to coordinate matrix element responsible for radiative transitions. Based on that, an expression for the ration of radiative and non-radiative lifetimes will be derived. Such parameter becomes important when it comes to exploitation of radiative transition in optoelectronics applications, particularly lasing.

3.2 Confined Phonon Modes in CQDs

Introduced bulk model can be used in the case of SAQDs since the crystal symmetry of the bulk approximately remains valid. Fabricational process of CQDs leaves them surrounded by completely different material and crystal symmetry of the entire structures remains broken. Surrounding dielectric material can also be viewed as electronically and vibrationally decoupled from the CQD. In that case, it is more plausible to use empirical models for modeling of the vibrational structure of CQDs. In Sec. 3.1.1, final expressions for electron-phonon couplings were given at the end in terms of macroscopic measurable quantities and those equations follow from the continuum models.

The main aim is to obtain the phonon spectra and electron-phonon coupling constants for CQDs by using the continuum models. Obtained phonon spectra will be further used in the fifth chapter in order to study transport properties of CQD supercrystals in terms of the phonon spectra.

3.2.1 Elastic Continuum Model

Elastic continuum model gives acoustic-like modes due to elasticity of the considered continuum system. In order to model acoustic-like modes in semiconductor materials by continuum displacement field $\boldsymbol{u}\left(\boldsymbol{r}\right)$, one applies appropriate vector differential equation to the displacement field (Note that

index μ which counts basis atoms within the unit cell is not important here since the object material is considered as one homogeneous continuum):

$$\rho\frac{\partial^2 \boldsymbol{u}}{\partial^2 t} = (c_{11} - c_{44})\,\mathrm{grad}\,\mathrm{div}\,\boldsymbol{u} + c_{44}\nabla^2\boldsymbol{u}. \qquad (3.33)$$

The equation (3.33) follows from classical mechanics of continuum elastic media [123] and relies upon elastic mechanical properties of materials,namely the mass density ρ, elastic constants c_{11}, c_{44} and corresponding Lame's constants $\lambda = c_{11} - 2c_{44}$ and $\mu = c_{44}$.

3.2.2 Acoustic Modes in Spherical CQDs

The full solution to the equation (3.33) for colloidal spherical quantum dots is given in Ref. 124. The boundary condition for the Eq. (3.33) is that displacement field vanishes at the dot-dielectric interface [124]. Such boundary condition may seem incorrect. The surface layer of atoms on each CQD is practically free and bounded to next layer of atoms positioned beneath the surface layer. Therefore, free boundary conditions seem as better choice. However, zero-field boundary condition will be adopted here as it gives far simpler mathematical treatment and it is not expected that boundary conditions affect overall results greatly. Also, coupling to acoustic-like phonons is certainly weaker than the coupling to optical-like phonons due to polar nature of CQDs.

There are two kinds of eigenmodes, namely torsional modes and spheroidal modes. Three solution counting numbers are introduced, n, l, m in accor-

dance with spherical quantum numbers. Torsional modes are given as:

$$\boldsymbol{T}_{lmn}\left(\boldsymbol{r}\right) = c_{lj}j_l\left(k^t_{lj}r\right) \times \tag{3.34}$$
$$\times \left(\frac{1}{\sin\theta}\frac{\partial Y_{lm}\left(\Omega\right)}{\partial\phi}\boldsymbol{e}_\theta - \frac{\partial Y_{lm}\left(\Omega\right)}{\partial\theta}\boldsymbol{e}_\phi\right),$$

where radial wavenumber k^t_{lj} depends only on quantum numbers l and j (superscript t refers to the torsional mode). In order to obtain possible values of k^t_{lj} one has to solve the following equation for each l:

$$k^t_{lj}aj'_l\left(k^t_{lj}a\right) - j_l\left(k^t_{lj}a\right) = 0. \tag{3.35}$$

Different solution for each l are counted by quantum number j. Coefficient c_{lj} is determined by normalization condition. For both types of modes the following normalization condition is adopted:

$$\int d^3r \boldsymbol{T}_{lmn}\left(\boldsymbol{r}\right) \cdot \boldsymbol{T}_{lmn}\left(\boldsymbol{r}\right) = \tag{3.36}$$
$$= \int d^3r \boldsymbol{S}_{lmn}\left(\boldsymbol{r}\right) \cdot \boldsymbol{S}_{lmn}\left(\boldsymbol{r}\right) = 1.$$

Spherodial modes are given as

$$\boldsymbol{S}_{lmn}\left(\boldsymbol{r}\right) = P_{lj}\left(r\right)Y_{lm}\left(\Omega\right)\boldsymbol{e}_r + \tag{3.37}$$
$$+ B_{lj}\left(r\right)\frac{\partial Y_{lm}\left(\Omega\right)}{\partial\theta}\boldsymbol{e}_\theta + B_{lj}\left(r\right)\frac{1}{\sin\theta}\frac{\partial Y_{lm}\left(\Omega\right)}{\partial\phi}\boldsymbol{e}_\phi,$$

where radial functions are defined as

$$P_{lj}\left(r\right) = p_{lj}j'_l\left(h^s_{lj}r\right) + q_{lj}\frac{l\left(l+1\right)}{k^s_{lj}r}j_l\left(k^s_{lj}r\right) \tag{3.38}$$

and

$$B_{lj}(r) = p_{lj} \frac{j_l\left(h_{lj}^s r\right)}{h_{lj}^s r} + q_{lj}\left(\frac{j_l\left(k_{lj}^s r\right)}{k_{lj}^s r} + j_l'\left(k_{lj}^s r\right)\right). \qquad (3.39)$$

For $l \neq 0$ and $m \neq 0$, coefficients p_{lj} and q_{lj} are determined by normalization condition above and by the set of linear equations:

$$p_{lj}\left[-\frac{c_{11}}{c_{44}}h_{lj}^s a j_l\left(h_{lj}^s a\right) + 2\left(l+2\right)j_{l+1}\left(h_{lj}^s a\right)\right] + \qquad (3.40)$$

$$+q_{lj}\left[lk_{lj}^s a j_l\left(k_{lj}^s a\right) - 2l\left(l+2\right)j_{l+1}\left(k_{lj}^s a\right)\right] = 0,$$

$$p_{lj}\left[-\frac{c_{11}}{c_{44}}h_{lj}^s a j_l\left(h_{lj}^s a\right) + 2\left(l-1\right)j_{l-1}\left(h_{lj}^s a\right)\right] +$$

$$+q_{lj}(l+1)\left[2\left(l-1\right)j_{l-1}\left(k_{lj}^s a\right) - k_{lj}^s a j_l\left(k_{lj}^s a\right)\right] = 0,$$

The condition that determinant of this system equals zero gives the values for radial wave numbers h_{lj}^s or k_{lj}^s which are connected via $c_{11}(h_{lj}^s)^2 = c_{44}(k_{lj}^s)^2$. For $l = m = 0$, only radial wave number h_{lj}^s and coefficient p_{lj} are relevant. Radial wave number h_{lj}^s is determined by

$$-\frac{c_{11}}{c_{44}}h_{lj}^s a j_0\left(h_{lj}^s a\right) + 4j_1\left(h_{lj}^s a\right) = 0, \qquad (3.41)$$

and coefficient p_{lj} is determined by normalization condition. Mode angular frequencies for both types of modes are determined by $\omega_{lj}^{s/t} = \sqrt{\frac{c_{44}}{\rho}}k_{lj}^{s/t}$.

3.2.3 Dielectric Continuum Model and Generalized Lyddane-Sachs-Teller relation

Optical phonon modes are strongly influenced by the polar nature of polar crystals as explained previosly in Sec. 3.1.1. Within the dielectric continuum model, different microscopic approach is used with the aim to define certain microscopical quantities depicting the polar nature of the crystal and to

relate them to the macroscopic measurable quantities. Some conclusions regarding the nature of vibrational structure in bulk will be used as starting point in macroscopic models.

Microscopically, net charge which we denote e^* is transfered from the ion of one kind to the ion of opposite kind. LO phonon modes have the adjacent atoms oscillating against each other which creates microscopical dipoles due to net charge e^*. Created polarization in return affects the oscillation of the optical mode. One considers continuum approximation where ion displacement of positive ions is denoted as $\boldsymbol{u}_+ (\boldsymbol{r})$ and of negative ions as $\boldsymbol{u}_- (\boldsymbol{r})$. It is also assumed that vibrational problem is solved for the lattice without ionic properties taking only short range elastic forces into account. Corresponding harmonic frequency to the elastic restoring force will be denoted as ω_0. We are interested in the relative ion displacement $\boldsymbol{u} (\boldsymbol{r}) = \boldsymbol{u}_- (\boldsymbol{r}) - \boldsymbol{u}_+ (\boldsymbol{r})$, i.e. we move the problem in the mass center system and accordingly introduce effective mass $\mu = \frac{m_- m_+}{m_- + m_+}$. One can show that driven oscillator microscopic equation for relative displacement reads

$$\mu \frac{d^2 \boldsymbol{u} (\boldsymbol{r})}{dt^2} = -\mu \omega_0^2 \boldsymbol{u} (\boldsymbol{r}) + e^* \boldsymbol{E}_{\text{loc}} (\boldsymbol{r}) , \qquad (3.42)$$

and equation for the macroscopic polarization field is:

$$\boldsymbol{P} (\boldsymbol{r}) = n e^* \boldsymbol{u} (\boldsymbol{r}) + n \alpha \boldsymbol{E}_{\text{loc}} (\boldsymbol{r}) , \qquad (3.43)$$

where e^* and α are charging and polarizability of electron clouds around two different adjacent atoms in dipolar semiconductor material. Local electric field $\boldsymbol{E}_{\text{loc}}$ does not equal to the macroscopic electric field around atoms $\boldsymbol{E}$. Induced microscopic polarization gives rise to the electric field $\boldsymbol{E}_{\text{near}}$ of neighboring atoms acting upon the observed atom. Such field should

be added to the macroscopic electric field $\boldsymbol{E}\left(\boldsymbol{r}\right)$. However, only part of the electric field from the neighboring atoms should be taken in account. Namely, one should subtract the electric field which comes from macroscopic, i.e. averaged polarization $\boldsymbol{P}\left(\boldsymbol{r}\right)$ because this part of the field is already taken into account through our macroscopic approach. One can show [134] that such field is given by

$$\boldsymbol{E}_P = -\frac{\boldsymbol{P}}{3\epsilon_0}. \tag{3.44}$$

One can write down the expression for local field $\boldsymbol{E}_{\mathrm{loc}}\left(\boldsymbol{r}\right) = \boldsymbol{E}\left(\boldsymbol{r}\right) + \boldsymbol{E}_{\mathrm{near}} + \frac{\boldsymbol{P}(\boldsymbol{r})}{3\epsilon_0}$. Actual electric field originating from nearby atoms is zero $\boldsymbol{E}_{\mathrm{near}} = 0$ for the case of cubic-based lattices [134]. This gives

$$\boldsymbol{E}_{\mathrm{loc}}\left(\boldsymbol{r}\right) = \boldsymbol{E}\left(\boldsymbol{r}\right) + \frac{\boldsymbol{P}\left(\boldsymbol{r}\right)}{3\epsilon_0} \tag{3.45}$$

This is so called Lorentz relation between macroscopic field $\boldsymbol{E}\left(\boldsymbol{r}\right)$ and local electric field. For the sake of better understanding of the theory, one can assume more general, but still linear relation between local electric field and macroscopic electric field

$$\boldsymbol{E}_{\mathrm{loc}}\left(\boldsymbol{r}\right) = \boldsymbol{E}\left(\boldsymbol{r}\right) + \kappa \boldsymbol{P}\left(\boldsymbol{r}\right) \tag{3.46}$$

where parameter κ measures the strength of polarization influence on the local electric field. For Lorentz relation it is $\kappa = \frac{1}{3\epsilon_0}$.

The gist of dielectric continuum model is to derive the formalism which will enable treatment of macroscopic values such as macroscopic electric field, polarization and electrostatic potential in terms of macroscopic, measurable medium parameters such as static dielectric constant $\epsilon\left(\omega = 0\right)$, dynamic dielectric constant $\epsilon\left(\omega = \infty\right)$, longitudinal and transversal frequencies

of bulk optical modes at the Brillouin zone center ω_{LO} and ω_{LO}. The model determines electromagnetic macroscopic quantities inside the medium and relates them to the displacement field, linearly as previously assumed. All microscopic parameters such as e^*, α, n and μ can be eliminated and expressed via macroscopic measurable quantities.

Beside the equations (3.42), (3.43) and (3.46) it is necessary to include Maxwell equations(in absence of external charges and currents) for macroscopic fields $\boldsymbol{E}(\boldsymbol{r})$ and $\boldsymbol{P}(\boldsymbol{r})$. It is possible to derive equation which relates $\boldsymbol{E}(\boldsymbol{r})$ and $\boldsymbol{P}(\boldsymbol{r})$ from Maxwell equations. The solutions for mentioned fields is searched in plane wave form $\sim e^{i(\boldsymbol{k}\cdot\boldsymbol{r}-\omega t)}$ Using these equations one solves eigenproblem of homogeneous system of equations for fields $\boldsymbol{u}(\boldsymbol{r})$, $\boldsymbol{E}(\boldsymbol{r})$ and $\boldsymbol{P}(\boldsymbol{r})$ in order to obtain eigenfrequencies for optical modes as done in details in Ref. [135]. Once the eigenproblem is solved it is easy to derive the expression for macroscopic relative permittivity ϵ_r from its definition

$$\boldsymbol{P}(\boldsymbol{r}) = \epsilon_0 (\epsilon_r - 1) \boldsymbol{E}(\boldsymbol{r}). \tag{3.47}$$

The detailed procedure can be found in Ref. [135] and here, only intuitive approach will be presented.

Due to Maxwell equation

$$\mathrm{div}\left(\epsilon(\omega)\boldsymbol{E}(\boldsymbol{r})\right) = i\epsilon(\omega)\boldsymbol{k}\cdot\boldsymbol{E}(\boldsymbol{r}) = 0$$

and assumed plane-wave solution only transversal ($\boldsymbol{k} \perp \boldsymbol{u}(\boldsymbol{r})$) and longitudinal ($\boldsymbol{k} \parallel \boldsymbol{u}(\boldsymbol{r})$ and $\epsilon(\omega) = 0$) modes are allowed. Eigenfrequency of longitudinal modes is conditioned by $\epsilon(\omega_{\mathrm{LO}}) = 0$, whereas all other frequencies are equal to the oscillator frequency arising from elastic force and the force due to induced polarization. In order to obtain this frequency one has to

eliminate $\boldsymbol{E}_{\text{loc}}\left(\boldsymbol{r}\right)$ and $\boldsymbol{P}\left(\boldsymbol{r}\right)$ from equations (3.42), (3.43) and (3.46) and to establish microscopic equation relating displacement field and macroscopic electric field:

$$\mu\left(\frac{d^2}{dt^2}+\omega_0^2-\frac{\kappa n(e^*)^2}{\mu\left(1-\kappa n\alpha\right)}\right)\boldsymbol{u}\left(\boldsymbol{r}\right)=\frac{e^*\boldsymbol{E}\left(\boldsymbol{r}\right)}{1-\kappa n\alpha}\tag{3.48}$$

One can see here that frequency of non-longitudinal modes, i.e. transversal modes is given as

$$\omega_{\text{TO}}^2=\omega_0^2-\frac{\kappa n(e^*)^2}{\mu\left(1-\kappa n\alpha\right)}.\tag{3.49}$$

By using the equations (3.42), (3.43) and (3.46) one can relate macroscopic electric field and polarization end extract expression for dielectric constant

$$\epsilon\left(\omega\right)=\epsilon_0+n\frac{\alpha-\frac{(e^*)^2}{\mu\left(\omega^2-\omega_0^2\right)}}{1-\kappa n\left(\alpha-\frac{(e^*)^2}{\mu\left(\omega^2-\omega_0^2\right)}\right)}\tag{3.50}$$

Now it is possible to introduce following macroscopical parameters

$$\epsilon\left(\infty\right)=\epsilon_0+\frac{n\alpha}{1-\kappa n\alpha}.\tag{3.51}$$

and

$$\epsilon\left(0\right)=\epsilon_0+n\frac{\alpha+\frac{(e^*)^2}{\mu\omega_0^2}}{1-\kappa n\left(\alpha+\frac{(e^*)^2}{\mu\omega_0^2}\right)}.\tag{3.52}$$

Longitudinal mode frequency can be related to microscopic parameters from the condition that $\epsilon\left(\omega_{\text{LO}}\right)=0$ and equation (3.50)

$$\omega_{\text{LO}}^2=\omega_0^2+\frac{n(e^*)^2}{\mu\epsilon_0}\frac{1-\kappa\epsilon_0}{1+\alpha n\left(1-\kappa\epsilon_0\right)}.\tag{3.53}$$

Dielectric constant in terms of empirical parameters reads as

$$\epsilon\left(\omega\right) = \epsilon\left(\infty\right)\frac{\omega^2 - \omega_{LO}^2}{\omega^2 - \omega_{TO}^2}, \tag{3.54}$$

which is well known generalized Lyddane-Sachs-Teller relation. One can express frequency corresponding to elastic force ω_0 in terms of empirical parameters

$$\omega_0 = \omega_{\mathrm{LO}}\sqrt{\frac{\epsilon(\infty)\left(1 + \kappa\left(\epsilon(0) - \epsilon_0\right)\right)}{\epsilon(0)\left(1 + \kappa\left(\epsilon(\infty) - \epsilon_0\right)\right)}}. \tag{3.55}$$

Maxwell equations combined with generalized Lyddane-Sachs-Teller relation provide the basis of dielectric continuum model. However, in order to obtain expressions for electron phonon coupling it is very important to keep track of microscopical parameters and their relation to macroscopic parameters.

3.2.4   LO Modes in Spherical CQDs

One can obtain confined optical modes in spherical nanocrystal by employing dielectric continuum model [136, 137, 138]. Optical modes can induce polarization inside the lattice. Dielectric continuum model is based on solving the Laplace equation for the electrostatic potential induced by that polarization:

$$\epsilon\triangle\phi = 0, \tag{3.56}$$

where ϵ is given by (3.54). Longitudinal optical(LO) modes are obtained as solutions of $\epsilon = 0$ and surface modes are obtained by setting $\triangle\phi = 0$. Obviously, frequencies of confined optical modes are the same as those of bulk ω_{LO}. In the case of LO modes, ϕ can be any function which vanishes at the boundary of the nanocrystal. It can be thus expanded in the basis

of spherical harmonics $\phi(\boldsymbol{r}) = \sum_{lmn} \phi_{lmn} j_l(k_n \boldsymbol{r}) Y_{lm}(\theta, \phi)$. Each spherical harmonic defines the mode labeled by l, m and n with frequency ω_{LO}. Values of longitudinal wavevector k_n can be obtained by setting the boundary condition $\phi(a) = 0$. Therefore, the condition $j_l(k_n a) = 0$ gives $k_n = \frac{\alpha_{nl}}{a}$ where α_{nl} is nth zero of the spherical Bessel function of order l.

Given the potential one readily obtains electric field as

$$\boldsymbol{E}(\boldsymbol{r}) = -\mathrm{grad}\left(\phi(\boldsymbol{r})\right). \tag{3.57}$$

Displacement field is proportional to the electric field and (lmn) mode of the displacement field can be written as

$$\boldsymbol{L}_{lmn}(\boldsymbol{r}) = L_{lmn}^0 \mathrm{grad}\left(j_l(k_n \boldsymbol{r}) Y_{lm}(\theta, \phi)\right). \tag{3.58}$$

Normalization constant is determined from the normalization condition

$$\int d^3 \boldsymbol{r}\, \boldsymbol{L}_{lmn}(\boldsymbol{r}) \cdot \boldsymbol{L}_{lmn}(\boldsymbol{r}) = 1, \tag{3.59}$$

calculated with the use of Green's first identity

$$1 = \left(L_{lmn}^0\right)^2 \int d^3 \boldsymbol{r}\, [\mathrm{grad}\left(j_l(k_n \boldsymbol{r}) Y_{lm}(\theta, \phi)\right)]^2 = \tag{3.60}$$

$$= -\left(L_{lmn}^0\right)^2 \int d^3 \boldsymbol{r}\, j_l(k_n \boldsymbol{r}) Y_{lm}(\theta, \phi)\, \mathrm{div}\left[\mathrm{grad}\left(j_l(k_n \boldsymbol{r}) Y_{lm}(\theta, \phi)\right)\right] =$$

$$= \left(L_{lmn}^0\right)^2 k_n^2 \frac{a^3}{2} j_{l+1}^2(k_n a).$$

Therefore normalization constant reads as $L_{lmn}^0 = \sqrt{\frac{2}{a^3}} \frac{1}{k_n j_{l+1}(k_n a)}$. Presented continuum models will be used for the case of spherical CQDs. In the last chapter, transport properties of CQD-solids will be presented. Transport for such case occurs through conduction band and approximation is

adopted that it occurs through ground s-like states. The electron wavefunction of s-like electronic state is given with Eq. (2.35) for the case of ground state. Due to spherical symmetry of the assumed electron wavefunction it turns out that only LO modes with $l = 0$ and $m = 0$ couple with electrons and thus surface modes will not be considered here and could be found elsewhere [137, 136, 138, 135].

3.2.5 Second Quantization of Phonons in CQDs

In order to examine physical properties arising due to the electron-phonon interaction, one has to switch to the second quantization formalism. Procedure is the same as it was for the bulk modes in Sec. 3.1. One starts with the proper Hamiltonian within the continuum model and then switches from displacement and momentum operators to the annihilation and creation operators.

For elastic continuum model, Hamiltonian is given as

$$H = \int \left(\frac{\rho}{2} \dot{\boldsymbol{u}}^2(\boldsymbol{r}) + \frac{c_{11}}{2} (\mathrm{div} \boldsymbol{u}(\boldsymbol{r}))^2 + \frac{c_{44}}{2} (\mathrm{rot} \boldsymbol{u}(\boldsymbol{r}))^2 \right) \mathrm{d}^3 \boldsymbol{r}, \qquad (3.61)$$

while for dielectric continuum model(only LO phonons are considered due to their dominant interaction with carriers) it is given as

$$H = \frac{\rho}{2} \int \dot{\boldsymbol{u}}^2(\boldsymbol{r}) \mathrm{d}^3 \boldsymbol{r} + \frac{\rho}{2} \omega_{LO}^2 \int \boldsymbol{u}^2(\boldsymbol{r}) \mathrm{d}^3 \boldsymbol{r}. \qquad (3.62)$$

Annihilation and creation operators can be introduced as follows:

$$\hat{\boldsymbol{u}}(\boldsymbol{r}) = \sum_{lmn} \tau_{lmn} \left(\hat{a}_{lmn} + (-1)^m \hat{a}_{l-mn}^\dagger \right) \boldsymbol{u}_{lmn}(\boldsymbol{r}), \qquad (3.63)$$

where $(-1)^m$ factor is introduced to achieve Hermicity of the Hamiltonian.

Modes $\boldsymbol{u}_{lmn}(\boldsymbol{r})$ can in general be torsional $\boldsymbol{T}_{lmn}(\boldsymbol{r})$, spherodial $\boldsymbol{S}_{lmn}(\boldsymbol{r})$ or LO $\boldsymbol{L}_{lmn}(\boldsymbol{r})$ modes. Postulating the commutation relations between displacement vector $\boldsymbol{u}$ and canonically conjugate momentum vector $\rho\dot{\boldsymbol{u}}$ one obtains

$$\tau_{lmn}^2 = \frac{\hbar}{2\rho\omega_{lmn}}. \tag{3.64}$$

The Hamiltonian is then

$$\hat{H} = \sum_{lmn} \hbar\omega_{lmn} \left(\hat{a}_{lmn}^\dagger \hat{a}_{lmn} + \frac{1}{2} \right). \tag{3.65}$$

3.2.6 Electron-Phonon Interaction for Continuum Models

It was demonstrated in Sec. 3.1 that electron-phonon interaction in bulk arises due to two different types of forces between electrons and phonons. Acoustic phonons affect electrons via short range forces and will be firstly examined in what follows.

The dominant term in deformation coupling is proportional to divergence of displacement field as explained in the Sec. 3.1.1. Note that approximation is made if one uses bulk value parameter E_d for the treatment of CQD problem, since the size of CQD is not comparable with the bulk.

Since electron-phonon deformation coupling is proportional to divergence of displacement field, i.e. $e_{xx} + e_{yy} + e_{zz}$, only longitudinal component of spheroidal modes couples to electron via deformation coupling:

$$g_{\text{def}}(\boldsymbol{r}_e) = E_d \text{div}(\boldsymbol{S}_{lmn}(\boldsymbol{r}_e)). \tag{3.66}$$

The same phonon-induced lattice strain produces piezoelectric polarization which significantly affects electron energy. CdSe nanocrystals can have zinc-blende, wurtzite and rock salt lattice type. We choose zinc-blende lattice

type and for zinc-blende crystals, induced piezoelectric polarization is given as:

$$\boldsymbol{P}_{\text{PZ}}\left(\boldsymbol{r}\right) = e_{14}\left(e_{yz}, e_{zx}, e_{xy}\right), \tag{3.67}$$

where strain tensor is defined as $e_{xx} = \frac{\partial u_x}{\partial x}$ and $e_{xy} = \frac{1}{2}\left(\frac{\partial u_x}{\partial y} + \frac{\partial u_x}{\partial y}\right)$ and e_{14} is piezoelectric constant. Electron-lattice interaction is then given as the potential energy of the electron inside the piezoelectric polarization field [134]:

$$g_{\text{piez}}\left(\boldsymbol{r}_e\right) = -\frac{e}{4\pi\epsilon}\int \mathrm{d}^3\boldsymbol{r}\nabla_{\boldsymbol{r}}\left(\frac{1}{|\boldsymbol{r}-\boldsymbol{r}_e|}\right)\cdot\boldsymbol{P}_{\text{PZ}}\left(\boldsymbol{r}\right). \tag{3.68}$$

As already indicated, continuum models will be used in order to obtain electron-phonon interaction in spherical CQDs and only s-like ground state will be considered. Taking into account the symmetry of s-like electron wavefunction it turns out that torsional modes do not couple with electron in the ground state. Spheroidal modes with $l = 0$ and $m = 0$ couple with electrons via both deformation potential and piezoelectric coupling. Spheroidal modes with $l = 2$ and $m = 0$ couple with electrons only via piezoelectric coupling. We take into account only values $j = 1, 2$ since coupling is significantly decreased with increasing the quantum number j (as shown by calculations).

LO phonons couple to carriers only via long range forces due to opposite oscillations of different ions with opposite charges within the same unit cell of a polar crystal. Macroscopically, it means that electrostatic potential introduced in subsection 3.2.4 due to induced polarization within the electric continuum model act as potential on carriers induced by LO phonon modes. Therefore, such potential can be considered as a basis for electron-LO phonon interaction. Therefore, one starts derivation from macroscopic potential defined via $-\text{grad}\left(\phi(\boldsymbol{r})\right) = \boldsymbol{E}(\boldsymbol{r})$. For LO modes permittivity is

zero and $-\epsilon_0 \boldsymbol{E}(\boldsymbol{r}) = \boldsymbol{P}(\boldsymbol{r})$ holds. Equation (3.43), therefore gives

$$\text{grad}\left(\phi(\boldsymbol{r})\right) = \frac{ne^*}{\epsilon_0(1 - \kappa n\alpha) + n\alpha} \boldsymbol{u}(\boldsymbol{r}) \tag{3.69}$$

Equations (3.51) and (3.52) give following relations

$$n\alpha = \frac{\epsilon(\infty) - \epsilon_0}{1 + \kappa\left(\epsilon(\infty) - \epsilon_0\right)} \tag{3.70}$$

and

$$\frac{n(e^*)^2}{\mu\omega_0^2} = \frac{\left(\epsilon(0) - \epsilon_0\right)\left(1 - \kappa n\alpha\right) - n\alpha}{1 + \kappa\left(\epsilon(0) - \epsilon_0\right)}. \tag{3.71}$$

Exploiting equations (3.70) and (3.71) one can transform equation (3.69) into

$$\text{grad}\left(\hat{\phi}(\boldsymbol{r})\right) = \omega_{\text{LO}}\sqrt{n\mu}\sqrt{\frac{1}{\epsilon(\infty)} - \frac{1}{\epsilon(0)}}\hat{\boldsymbol{u}}(\boldsymbol{r}) \tag{3.72}$$

For LO modes, displacement operator is given as

$$\hat{\boldsymbol{u}}(\boldsymbol{r}) = \sum_{lmn}\sqrt{\frac{\hbar}{2n\mu\omega_{\text{LO}}}}\left(\hat{a}_{lmn} + (-1)^m\hat{a}^\dagger_{l-mn}\right)\boldsymbol{L}_{lmn}(\boldsymbol{r}) \tag{3.73}$$

where

$$\boldsymbol{L}_{lmn}(\boldsymbol{r}) = L^0_{lmn}\text{grad}\left(j_l\left(k_n\boldsymbol{r}\right)Y_{lm}\left(\theta, \phi\right)\right) \tag{3.74}$$

Therefore, electron-LO phonon interaction operator is given as

$$g_{\text{polar}}(\boldsymbol{r}_e) = \sum_{lmn}L^0_{lmn}\sqrt{\frac{1}{\epsilon(\infty)} - \frac{1}{\epsilon(0)}}\sqrt{\frac{\hbar\omega_{\text{LO}}}{2}}\times \tag{3.75}$$

$$\times\left(\hat{a}_{lmn} + (-1)^m\hat{a}^\dagger_{l-mn}\right)j_l\left(k_n r_e\right)Y_{lm}\left(\theta_e, \phi_e\right)$$

where $L^0_{lmn} = \sqrt{\frac{2}{a^3}}\frac{1}{k_n j_{l+1}(k_n a)}$ has been defined previously.

For further consideration, only modes with the largest ratio of electron-

Mode Types $\rightarrow$	Acoustic Spheroidal		Acoustic Spheroidal		Acoustic Spheroidal		Acoustic Spheroidal	
Parameters [meV] $\rightarrow$	$\hbar\Omega_1$	G_1	$\hbar\Omega_2$	G_2	$\hbar\Omega_3$	G_3	$\hbar\Omega_4$	G_4
2.0 nm	3.40	-3.36	7.29	0.48	1.32	-1.29	2.60	0.86
2.5 nm	2.72	-2.49	5.83	0.49	1.05	-1.03	2.08	0.69
3.0 nm	2.27	-1.96	4.86	0.47	0.88	-0.86	1.73	0.57
3.5 nm	1.95	-1.61	4.16	0.44	0.75	-0.74	1.48	0.49
4.0 nm	1.70	-1.36	3.64	0.40	0.66	-0.64	1.30	0.43

Table 3.1: Acoustic Phonon energies $\hbar\Omega$ and electron-phonon coupling constants to the electronic ground state G in a CdSe NC for different values of the dot radius.

Mode Types $\rightarrow$	Longitudinal Optical		Longitudinal Optical	
Parameters [meV] $\rightarrow$	$\hbar\Omega_5$	G_5	$\hbar\Omega_6$	G_6
2.0 nm	24.00	43.00	24.00	7.45
2.5 nm	24.00	38.46	24.00	6.66
3.0 nm	24.00	35.11	24.00	6.08
3.5 nm	24.00	32.51	24.00	5.63
4.0 nm	24.00	30.41	24.00	5.26

Table 3.2: LO Phonon energies $\hbar\Omega$ and electron-phonon coupling constants to the electronic ground state G in a CdSe NC for different values of the dot radius.

phonon coupling and corresponding phonon energy are chosen. Selected modes and corresponding parameters are presented in Tab. 3.1 for acoustic modes and in Tab. 3.2 for LO modes. The inclusion of additional modes has no significant effect on the simulation of transport through CQD-supercrystal in the fifth chapter. At the end, one can conclude that both phonon energies and coupling strength constants decrease with the increasing of the dot radius. Decreasing of the frequency of the acoustic modes with increasing of the dot radius is expected as it mimics the limit of the bulk where acoustic modes have linear dispersion with the ground phonon mode having the zero frequency. The decreasing of the coupling is due to lesser confinement of both electron wavefunction and phonon modes and thus more inefficient overlaping in larger dots.

Chapter 4

Intraband Optical Properties of SAQDs

In Chapters 2 and 3, theoretical modeling of intrinsic properties of quantum dots have been introduced. Electrons and phonons are intrinsic particles in any condensed matter system defining most of physical properties of the system. The main aim of this thesis is to study intraband opoelectronic properties of heterestructures based on quantum dots. Therefore, modeling of optical properties plays a crucial role in description of these heterostructures and their potential applications in the field of optoelectronics.

Most of the experiments studying optical properties of quantum dots are based on measuring the absorption spectrum of incident light and measuring of luminescence spectra (if any). It is also possible to measure the evolution of the absorption spectra with the picosecond resolution which can give information on dynamical properties of the carriers. Absorption and luminescence spectrum can exhibit all types of broadening, but remarkable fact is that up to date resolution of optical experiments is very good enabling the study of the light-single quantum dot interaction. In such way, inhomoge-

neous type of broadening of absorption and emission lines due to distribution in quantum dot size can be avoided and only broadenings of homogenous type due to intrinsic properties of single quantum dot can be captured. In such way, it is possible to study influence of electron and phonon spectrum and their mutual interaction on the optical properties of quantum dots.

This chapter is organized as follows. First the modeling of the incident light is given and proper Hamiltonian is derived for the interaction between carriers and photons. Then, quantum mechanical modeling of experimentally accessible absorption and emission spectrum is presented together with the modeling of the evolution of the optically excited quantum dots.

Some of the presented models are then used to study optical properties of quantum rods which is the part of the contribution of this chapter. Polarization independent THz photodetector based on the BIC in quantum rods is then presented.

The second part of the contribution of this chapter is establishment of the connection between electron-photon and electron-phonon types of coupling. Since the electron-photon coupling is responsible for absorption spectrum of carriers and electron-phonon coupling is responsible for non-radiative lifetime of carriers then the connection between readily measurable absorption spectrum and non-radiative lifetimes can be established.

4.1 Hamiltonian and Dipole Approximation

Hamiltonian of the electron inside the electromagnetic field is given as [134]

$$\hat{H} = \frac{(\hat{\boldsymbol{p}} + e_0 \boldsymbol{A})^2}{2m_0} - e_0 \phi + V_0(\boldsymbol{r}), \qquad (4.1)$$

where $V_0(\boldsymbol{r})$ is the static potential of the considered sample structure. For the type of electromagnetic field of the radiation present in the studied sample is usually considered in the Coulomb gauge with scalar potential $\phi = 0$ and the vector potential given in the form of plane wave [134]: $\boldsymbol{A}\left(\boldsymbol{r},t\right) = \boldsymbol{A}_0 e^{i(\boldsymbol{k}\cdot\boldsymbol{r}-\omega t)}$. Alternative microscopic one-electron Hamiltonian can be obtained by introducing a new gauge transformation which transforms vector potential to $\boldsymbol{A}\left(r,t\right) = 0$ and gives rise to the electrostatic potential which can be further used for the Hamiltonian of the interaction. Such gauge transformation is the Göppert-Mayer transformation and it is obtained by using the gauge function $\Gamma(\boldsymbol{r},t) = -\boldsymbol{r} \cdot \boldsymbol{A}\left(\boldsymbol{r},t\right)$. The transformed scalar potential then reads as $\phi(\boldsymbol{r},t) = -\boldsymbol{r} \cdot \boldsymbol{E}\left(\boldsymbol{r},t\right)$ and vector potential disappears $\boldsymbol{A}\left(\boldsymbol{r},t\right) = 0$. The microscopic Hamiltonian of interaction of electrons with electromagnetic radiation is given via one-electron dipole operator $\hat{\boldsymbol{\Pi}} = -e_0\hat{\boldsymbol{r}}$ and it reads:

$$\hat{H}'(t) = -\boldsymbol{E}\left(\boldsymbol{r},t\right) \cdot \hat{\boldsymbol{\Pi}} \tag{4.2}$$

This Hamiltonian will be used further, but the final results do not depend on the choice of the gauge. The Coulomb gauge gives the interaction expressed via momentum operator and that will be demonstrated in the next chapter. However, in the later sections of this chapter, the linear relation between coordinate and momentum matrix elements will be demonstrated. Such relation is the basis of the equivalence of the two different interaction Hamiltonians arising from two different gauge transformations. Therefore, the whole presented approach that follows is gauge invariant.

One considers electric field $\boldsymbol{E}$ as a classical variable which is satisfactory approach for semiclassical modeling of induced emission and absorption with

main aim to model coefficient of loss or gain in active medium or to estimate homogeneous broadening due to intrinsic interactions. In this case, state of the system is electron state and electric field $\boldsymbol{E}$ just creates additional potential upon electrons. The equivalent approach would be without introducing the Göppert-Mayer gauge transformation and expressing the Hamiltonian in terms of the vector potential and momentum operator. Such approach will be used in the next chapter. The equivalence will be demonstrated in this chapter as well via relation of the electron coordinate and momentum matrix elements.

The wavelengths of interest will be those in the mid-infrared region of the spectrum, when the wavelength of the radiation is much larger than the size of the quantum dot. Therefore, in a certain moment of time, the dot effectively sees a constant electromagnetic field, and consequently the spatial dependence of $\boldsymbol{E}$ can be neglected: $\boldsymbol{E}\left(\boldsymbol{r}, t\right) = \boldsymbol{E}_0 e^{-i\omega t}$.

4.2   Linear Response Theory

Any condensed matter system such as quantum dots, can be described by some intrinsic Hamiltonian $\hat{H}$ accounting for electronic and vibrational degrees of freedom. When such samples are exposed to external electromagnetic field through incident radiation or applied voltages, additional Hamiltonian term linear in electromagnetic field, usually dependent on time, appears which can be considered perturbatively. Dynamic perturbation perturbates the system and thermodynamical average, i.e. expected value of random observable (operator) $\hat{B}$ changes accordingly. The change is depicted with quantity $\delta\left(\hat{B}\right)$ called response. Kubo formula for perturbation adiabatically turned on at $t_0 = -\infty$ and linear response measured at some

moment t is given by [139]

$$\delta\left(\hat{B}\right) = \frac{i}{\hbar}\int_{-\infty}^{t} dt' \left\langle \left[\hat{H}'_I\left(t'\right), \hat{B}_I\left(t\right)\right]\right\rangle, \tag{4.3}$$

where subscript I denotes operator in interaction picture, i.e. $\hat{B}_I\left(t\right) = e^{i\hat{H}t}\hat{B}e^{-i\hat{H}t}$. Angle brackets denote thermodnamic average in canonic ensemble with respect to the system Hamiltonian.

4.3 Linear Susceptibility and Absorption Lineshape

Linear susceptibility establishes linear relation between Fourier components of external electric field and induced polarization:

$$P_\nu\left(\boldsymbol{r}, t\right) = \epsilon_0 \sum_\mu \chi_{\nu\mu}(\omega)E_\mu\left(\boldsymbol{r}, t\right) \tag{4.4}$$

Linear susceptibility can be obtained following the Kubo formula (4.3). Hence, one has to apply Kubo formula for the change of expectation value of the ν-th Cartesian component of the dipole operator:

$$\delta\left(\hat{\Pi}_\nu\right) = \frac{i}{\hbar}\int_{-\infty}^{t} dt' \left\langle \left[\hat{H}'_I\left(t'\right), \hat{\Pi}_{\nu I}\left(t\right)\right]\right\rangle, \tag{4.5}$$

$$\delta\left(\hat{\Pi}_\nu\right) = -\frac{i}{\hbar}\sum_\mu \boldsymbol{E}_{0\mu}e^{-i\omega t}\int_{-\infty}^{t} dt' e^{i\omega(t-t')}\left\langle \left[\hat{\Pi}_{\mu I}\left(t'\right), \hat{\Pi}_{\nu I}\left(t\right)\right]\right\rangle. \tag{4.6}$$

Commutator expression in the last equation depends only on $t - t'$. Changing the variable of integration $t - t' \rightarrow t$ and taking into account the polarization and dipole operator are related via $\hat{P}_\nu = \frac{\hat{\Pi}_\nu}{V}$ where V is the

volume of considered system, one obtains expression for linear susceptibility

$$\chi_{\nu\mu}(\omega) = \frac{i}{\epsilon_0 V \hbar} \int_0^\infty dt e^{i\omega t} \left\langle \left[\hat{\Pi}_{\nu I}(t), \hat{\Pi}_{\mu I}(0) \right] \right\rangle. \qquad (4.7)$$

In order to obtain imaginary part of susceptibility, which further gives absorption lineshape, one examines complex conjugate expression:

$$\chi_{\nu\mu}^*(\omega) = \frac{-i}{\epsilon_0 V \hbar} \int_0^\infty dt e^{-i\omega t} \left\langle \left[\hat{\Pi}_{\nu I}(t), \hat{\Pi}_{\mu I}(0) \right]^\dagger \right\rangle \qquad (4.8)$$

Following the rules for the Hermitian adjoint of an operator product, one can easily show that

$$\left\langle \left[\hat{\Pi}_{\nu I}(t), \hat{\Pi}_{\mu I}(0) \right]^\dagger \right\rangle = \left\langle \left[\hat{\Pi}_{\mu I}(0), \hat{\Pi}_{\nu I}(t) \right] \right\rangle. \qquad (4.9)$$

Hence

$$\chi_{\nu\mu}^*(\omega) = \frac{-i}{\epsilon_0 V \hbar} \int_0^\infty dt e^{-i\omega t} \left\langle \left[\hat{\Pi}_{\mu I}(0), \hat{\Pi}_{\nu I}(t) \right] \right\rangle, \qquad (4.10)$$

and changing the time variable from t to $-t$ one obtains:

$$\chi_{\nu\mu}^*(\omega) = \frac{-i}{\epsilon_0 V \hbar} \int_{-\infty}^0 dt e^{i\omega t} \left\langle \left[\hat{\Pi}_{\mu I}(t), \hat{\Pi}_{\nu I}(0) \right] \right\rangle. \qquad (4.11)$$

Here, one assumes that μ-polarized incident radiation induces μ-polarized polarization only, i.e. the only case of interest in the last commutator expression is when $\mu = \nu$. In such case, commutator expressions from Eqs. (4.7) and (4.11) are identical. The imaginary part of susceptibility follows from its mathematical definition:

$$\mathrm{Im}\left(\chi_{\mu\mu}(\omega)\right) = \frac{\chi_{\mu\mu}(\omega) - \chi_{\mu\mu}^*(\omega)}{2i} \qquad (4.12)$$

and it reads:

$$\text{Im}\left(\chi_{\mu\mu}\left(\omega\right)\right) = \frac{1}{2\epsilon_0\hbar V} \int_{-\infty}^{\infty} dt e^{i\omega t} \left\langle \left[\hat{\Pi}_{\mu I}\left(t\right), \hat{\Pi}_{\mu I}\left(0\right)\right]\right\rangle. \tag{4.13}$$

In order to eliminate commutator in the last equation, one uses following identity:

$$e^{-\beta\hbar\omega} \int_{-\infty}^{\infty} dt e^{i\omega t} \left\langle \hat{\Pi}_{\mu I}\left(t\right) \hat{\Pi}_{\mu I}\left(0\right)\right\rangle = \tag{4.14}$$
$$= \int_{-\infty}^{\infty} dt e^{i\omega t} \left\langle \hat{\Pi}_{\mu I}\left(0\right) \hat{\Pi}_{\mu I}\left(t\right)\right\rangle,$$

which finally gives:

$$\text{Im}\left(\chi_{\mu\mu}\left(\omega\right)\right) = \frac{1 - e^{-\beta\hbar\omega}}{2\epsilon_0\hbar V} \int_{-\infty}^{\infty} dt e^{i\omega t} \left\langle \hat{\Pi}_{\mu I}\left(t\right) \hat{\Pi}_{\mu I}\left(0\right)\right\rangle. \tag{4.15}$$

Imaginary part of susceptibility can be used in order to provide absorption and gain lineshapes in active media. Let the μ-polarized radiation mode propagates through active medium with spatial exponential dependence of its intensity $I_\mu(z)$ which correspond to spatial differential equation

$$\alpha_\mu = -\frac{1}{I_\mu}\frac{dI_\mu}{dz} \tag{4.16}$$

where α_μ is absorption-gain coefficient depending on its sign. Complex susceptibility corresponds to complex refraction index via $n_C^2 = \left(\overline{n} + i\eta\right)^2 = 1 + \text{Re}\left\{\chi\right\} + i\text{Im}\left\{\chi\right\}$ and absorption coefficient is given as $\alpha = \frac{2\omega\eta}{c}$, i.e.

$$\alpha = \frac{\omega\text{Im}\left\{\chi\right\}}{\overline{n}c} \tag{4.17}$$

Therefore, absorption coefficient of the μ-polarized incident radiation is

given as:

$$\alpha_\mu(\omega) = \frac{\omega}{\epsilon_0 \overline{n} c} \frac{1 - e^{-\beta\hbar\omega}}{2\hbar V} \int_{-\infty}^{\infty} dt e^{i\omega t} \left\langle \hat{\Pi}_{\mu I}(t) \hat{\Pi}_{\mu I}(0) \right\rangle \qquad (4.18)$$

Specific configuration of interest is a single quantum dot. Quantum dot contains electrons and phonons and with electron-phonon interaction included, correlation function from the last equation becomes difficult to calculate. Electron-phonon coupling gives rise to homogeneous broadening to the absorption lineshape as indicated in many places in literature(for interband transitions see Refs. 140, 141, 142, 143, 144, 126, 145, 146, 147, whereas for intraband transitions see Refs. 148, 34, 56, 133, 61). Linewidth of such broadening defines coherence lifetime of induced polarized collective state of considered electron system. This spectral line consists of zero phonon line with linewidth less than 1 meV and very broad pedestal which is usually related to acoustic phonon induced decoherence [148, 34].

In order to study optical properties of ensembles of quantum dots it is sufficient to consider only pure electronic optical resonances as inhomogeneous broadening of the entire ensemble goes larger than phonon-induced homogeneous type of broadening. Therefore homogeneous broadening effect will not be considered in this thesis, but this is the starting point for its consideration. Lineshape broadening in such case comes only from the inhomogeneous type of broadening due to nonuniformity in the sizes of the quantum dots in an ensemble. Influence of inhomogeneous type of broadening will be considered in next section.

For a single quantum dot, dipole operator, i.e. μ-th Cartesian component

of it, can be written as:

$$\hat{\Pi}_\mu = -e \sum_{fi} \mathcal{R}^\mu_{fi} \hat{A}^\dagger_f \hat{A}_i, \tag{4.19}$$

where subscripts f and i count basis states of single quantum dot obtained by solving electronic structure eigenproblem and $\mathcal{R}^\mu_{fi} = \langle f | r_\mu | i \rangle$ is matrix element of the μ-th Cartesian component of the electron radius vector subject to further discussion in Sec. 4.5. Thus, one is interested in diagonal correlation function which can be expanded as:

$$\left\langle \hat{\Pi}_{\mu I}(t) \hat{\Pi}_{\mu I}(0) \right\rangle = e^2 \sum_{fimn} \mathcal{R}^\mu_{fi} \mathcal{R}^\mu_{mn} \langle \hat{A}^\dagger_{fI}(t) \hat{A}_{iI}(t) \hat{A}^\dagger_m \hat{A}_n \rangle. \tag{4.20}$$

By using the Wick's theorem [122] one can calculate thermodynamic average from the last equation:

$$\langle \hat{A}^\dagger_{fI}(t) \hat{A}_{iI}(t) \hat{A}^\dagger_m \hat{A}_n \rangle = e^{i\frac{E_f - E_i}{\hbar}t} \times \tag{4.21}$$
$$\times \left(\delta_{f,i} \delta_{m,n} n_f n_m + \delta_{f,n} \delta_{i,m} n_f (1 - n_m) \right),$$

where E_i and n_i are energy of the i-th electronic eigenstate and corresponding Fermi-Dirac distribution. In order to obtain absorption lineshape one has to consider only the term $\delta_{f,n} \delta_{i,m} n_f (1 - n_m)$ which contributes to the non-zero frequencies.

By putting (4.21) into expression for the correlation function (4.20) one obtains expression for the absorption lineshape for μ-polarized incident radiation:

$$\alpha_\mu(\omega) = \frac{\pi \omega e^2}{\epsilon_0 \overline{n} c} \frac{1 - e^{-\beta \hbar \omega}}{\hbar V} \sum_{fi} \left| \mathcal{R}^\mu_{fi} \right|^2 n_f (1 - n_i) \delta \left(\omega + \frac{E_f - E_i}{\hbar} \right) \tag{4.22}$$

Moving ω dependent factors into the sum one finally obtains:

$$\alpha_\mu(\omega) = \frac{\pi e^2}{\hbar^2 V \epsilon_0 \overline{n} c} \sum_{fi} (E_f - E_i) \left| \mathcal{R}_{fi}^\mu \right|^2 (n_i - n_f) \delta\left(\omega + \frac{E_f - E_i}{\hbar}\right) \quad (4.23)$$

4.4 Inhomogeneous Broadening and Cross Section

Realistic devices based on quantum dots contain many quantum dots with significant inhomogeneity in size distribution. Let the set of quantum dots considered contains N_{QD} quantum dots within the considered volume of the system V. Each quantum dot contributes equally to the absorption coefficient and the last expression for the absorption has to be multiplied by the number of quantum dots. Defining the density of quantum dots as $n_{QD} = \frac{N_{QD}}{V}$ and rescaling the argument of delta functions to energy units, one finally obtains:

$$\alpha_\mu(\omega) = \frac{2\pi e^2}{\hbar \epsilon_0 \overline{n} c} \sum_{f>i} (E_f - E_i) \left| \mathcal{R}_{fi}^\mu \right|^2 n_{QD} (n_i - n_f) \delta(\hbar\omega + E_f - E_i).$$

$$(4.24)$$

Note that the summation has changed from f, i to $f > i$ in order to present net absorption or emission (depending on the level of populations n_i and n_f) between every possible combination of states i and f without repetition. Multiplying factor 2 is added therefore.

As said earlier, the linewidth of the transition is entirely determined by the nonuniformity in the sizes of the quantum dots in an ensemble. These linewidths are of the order of at least several meV and are larger than the inherent homogeneous linewidths of a transition in a single dot. Therefore, in order to treat the inhomogeneous broadening one has to replace the delta

functions in (4.24) with a Gaussian, i.e.

$$\delta(x) \rightarrow g(x, 2\sigma) = \frac{1}{\sigma\sqrt{2\pi}} \exp\left(-\frac{x^2}{2\sigma^2}\right). \tag{4.25}$$

where linewidth σ depicts the inhomogeneity of the ensemble and can be used as fitting parameter.

The optical cross section of the $i \rightarrow f$ transition is the quantity proportional to the absorption due to the same transition, but does not depend on concentration of quantum dots n_{QD} and population difference of the optically active carriers $n_i - n_f$. The definition of the optical cross-section is given in connection to the absorption lineshape:

$$\alpha_\mu(\omega) = \sum_{f>i} n_{QD} (n_i - n_f) \sigma_{if}^\mu(\omega) \tag{4.26}$$

Cross section $\sigma_{if}^\mu(\omega)$ is very important quantity which quantifies strength of the optical transition regardless of the concentration of quantum dots and level of doping. Cross section of the $i \rightarrow f$ transition is:

$$\sigma_{if}^\mu(\omega) = \frac{2\pi e^2}{\hbar\epsilon_0\overline{n}c} (E_f - E_i) \left|\mathcal{R}_{fi}^\mu\right|^2 g(\hbar\omega + E_f - E_i). \tag{4.27}$$

4.5 Envelope Functions Matrix Elements

Matrix element $\mathcal{R}_{fi}^\mu = \langle f |\hat{r}_\mu| i \rangle$ plays crucial role in the expression for the absorption. The expression for the absorption was derived under the Göppert-Mayer gauge transformation and it was pointed out in Sec. 4.1 that the approach is gauge invariant. If one had used the Coulomb gauge, momentum matrix element instead of the coordinate matrix element would have occurred in he final expression. Therefore, there should be relation between

these two matrix elements in order to satisfy the gauge invariance. This relation will be demonstrated in what follows.

The following commutation relation holds for time independent Hamiltonian of the general form: $\hat{H} = \frac{\hat{p}^2}{2m_0} + \hat{V}(\boldsymbol{r})$ [149]:

$$\left[\hat{\boldsymbol{r}}, \hat{H}\right] = i\frac{\hbar}{m_0}\hat{\boldsymbol{p}} \tag{4.28}$$

one gets

$$\boldsymbol{\mathcal{P}}_{if} = -i\frac{m_0}{\hbar}\left(E_f - E_i\right)\boldsymbol{\mathcal{R}}_{if} \tag{4.29}$$

where $\mathcal{P}_{if}^{\mu} = \langle i\,|\hat{p}_{\mu}|\,f\rangle$. Therefore, matrix elements of the momentum and coordinate operators are proportional to each other. As shown in section 4.4, squared absolute values of these matrix elements determine gain and absorption between states $|i\rangle$ and $|f\rangle$. From now on, vector $\boldsymbol{\mathcal{R}}_{if}$ will be referred to as a "dipole coupling vector" between states $|i\rangle$ and $|f\rangle$. Thus, within the one band approximation for quantum dots, knowledge of dipole coupling vector provides us information on interaction between electron and electromagnetic radiation. It will be shown in subsequent chapters that it also provides information on matrix elements of interaction between electron and longitudinal optical phonon which establish a good basis for parallel incorporation of electron – phonon and electron – photon interaction in design of intraband laser and detector based on semiconductor quantum dots.

Further, one has to examine the recipe for calculation of the coordinate and momentum matrix element by using electronic structure formalisms derived in chapter 2.

The matrix element of the momentum and coordinate operators between

two states i and f whose envelope function representations are given as:

$$\Psi^{(i)}(\boldsymbol{r}) = \sum_n \psi_n^{(i)}(\boldsymbol{r}) u_{n0}(\boldsymbol{r}), \qquad (4.30a)$$

$$\Psi^{(f)}(\boldsymbol{r}) = \sum_m \psi_m^{(f)}(\boldsymbol{r}) u_{m0}(\boldsymbol{r}), \qquad (4.30b)$$

are then given by

$$\boldsymbol{\mathcal{P}}_{if} = \int \mathrm{d}^3\boldsymbol{r}\, \Psi^{(i)*}(\boldsymbol{r}) \hat{\boldsymbol{p}} \Psi^{(f)}(\boldsymbol{r}), \qquad (4.31a)$$

$$\boldsymbol{\mathcal{R}}_{if} = \int \mathrm{d}^3\boldsymbol{r}\, \Psi^{(i)*}(\boldsymbol{r}) \hat{\boldsymbol{r}} \Psi^{(f)}(\boldsymbol{r}), \qquad (4.31b)$$

leading to

$$\boldsymbol{\mathcal{P}}_{if} = \sum_{mn} \int \mathrm{d}^3\boldsymbol{r}\, \psi_n^{(i)*} u_n^* \left[u_m \hat{\boldsymbol{p}} \psi_m^{(f)} + \psi_m^{(f)} \hat{\boldsymbol{p}} u_m \right], \qquad (4.32a)$$

$$\boldsymbol{\mathcal{R}}_{if} = \sum_{mn} \int \mathrm{d}^3\boldsymbol{r}\, \psi_n^{(i)*} u_n^* \hat{\boldsymbol{r}} u_m \psi_m^{(f)}. \qquad (4.32b)$$

The slowly varying envelope functions $F(\boldsymbol{r})$ feel only the average value over the unit cell of Bloch functions that vary rapidly, which can mathematically be expressed as

$$\int \mathrm{d}^3\boldsymbol{r}\, F(\boldsymbol{r}) u(\boldsymbol{r}) = \int \mathrm{d}^3\boldsymbol{r}\, F(\boldsymbol{r}) \langle u(\boldsymbol{r}) \rangle, \qquad (4.33)$$

where $\langle u(\boldsymbol{r}) \rangle$ is the average value over unit cell of a rapidly varying function.

After exploiting this relation, and using the condition of orthonormality

of the Bloch functions, one arrives at

$$\boldsymbol{\mathcal{P}}_{if} = \sum_{mn} \int \mathrm{d}^3\boldsymbol{r}\, \psi_n^{(i)*} \left(\delta_{nm}\hat{\boldsymbol{p}} + \boldsymbol{p}_{nm} \right) \psi_m^{(f)}, \qquad (4.34a)$$

$$\boldsymbol{\mathcal{R}}_{if} = \sum_{n} \int \mathrm{d}^3\boldsymbol{r}\, \psi_n^{(i)*} \hat{\boldsymbol{r}} \psi_n^{(f)}, \qquad (4.34b)$$

where

$$\boldsymbol{p}_{mn} = \frac{1}{\Omega} \int u_m(\boldsymbol{r})^* \hat{\boldsymbol{p}} u_n(\boldsymbol{r}) \mathrm{d}^3\boldsymbol{r}, \qquad (4.35a)$$

$$\boldsymbol{r}_{mn} = \frac{1}{\Omega} \int u_m(\boldsymbol{r})^* \hat{\boldsymbol{r}} u_n(\boldsymbol{r}) \mathrm{d}^3\boldsymbol{r}, \qquad (4.35b)$$

In case of one band (conduction band) approximation equation (4.34) reduces to:

$$\boldsymbol{\mathcal{P}}_{if} = \int \mathrm{d}^3\boldsymbol{r}\, \psi^{(i)*} \hat{\boldsymbol{p}} \psi^{(f)}, \qquad (4.36a)$$

$$\boldsymbol{\mathcal{R}}_{if} = \int \mathrm{d}^3\boldsymbol{r}\, \psi^{(i)*} \hat{\boldsymbol{r}} \psi^{(f)}, \qquad (4.36b)$$

4.6   Optical Properties of Quantum Box

Electronic structure of two very simple models, so called quantum box and infinite quantum well, has been presented in section 2.2. In order to utilize expression (4.27), one needs to determine coordinate or momentum matrix elements by using results of the electronic structure calculations presented in section 2.2. Momentum matrix elements are easier for calculations.

To estimate absorption of light polarized to z direction, (growth direction), associated with unit vector **k** and a direction from symmetric xy plane, ("radial" or "in-plane" direction), lets say x direction associated with unit

vector $\mathbf{i}$, i.e. $\boldsymbol{\epsilon} = \epsilon_x \mathbf{i} + \epsilon_z \mathbf{k}$. After simple derivation expression, (4.36a) takes the form

$$\mathcal{P}_{if}^x = \begin{cases} -4i\hbar\frac{\phi_{if}^x}{a} & \text{for } \left(n_x^i - n_x^f\right) \text{ odd} \\ \\ 0 & \text{for } \left(n_x^i - n_x^f\right) \text{ even} \end{cases} \tag{4.37a}$$

$$\mathcal{P}_{if}^z = \begin{cases} -4i\hbar\frac{\phi_{if}^z}{d} & \text{for } \left(n_z^i - n_z^f\right) \text{ odd} \\ \\ 0 & \text{for } \left(n_z^i - n_z^f\right) \text{ even} \end{cases} \tag{4.37b}$$

where

$$\phi_{if}^x = \epsilon_x \delta_{n_y^i n_y^f} \delta_{n_z^i n_z^f} \frac{n_x^i n_x^f}{n_x^{f2} - n_x^{i2}}$$

$$\phi_{if}^z = \epsilon_z \delta_{n_x^i n_x^f} \delta_{n_y^i n_y^f} \frac{n_z^i n_z^f}{n_z^{f2} - n_z^{i2}}$$

All selection rules are included in the equations (4.37a) and (4.37b).

For infinite quantum well only nonzero matrix element for growth direction component of the incident radiation exists

$$p_{k_x,k_y,n,k_x',k_y',m}^z = \begin{cases} -4i\epsilon_z \frac{\hbar}{d}\delta_{k_x k_x'}\delta_{k_y k_y'}\frac{mn}{m^2-n^2} & \text{for } (m-n) \text{ odd} \\ \\ 0 & \text{for } (m-n) \text{ even} \end{cases} \tag{4.38}$$

This simple model accounting for optical resonances indicates that dominant optical transition in quantum dots is transition between s-like and p-like electronic state, i.e. between ground and first excited state. This is in agreement with the experiments [69, 71] where it was suggested that the dominant transition observed in the PL spectra of SAQDs is indeed

the transition between s-like and p-like states, which was based on numerical calculation of electronic states and optical matrix elements within the dipole approximation.

4.7 Absorption Spectra of Quantum Rods

Calculated electronic structure in Sec. 2.3 can be used to simulate the intraband absorption spectra of quantum rods. One needs to consider absorption independent from the concentration of the dots since such concentration is hard to estimate. Therefore, the quantity of interest which will be calculated is so called "temperature and Fermi level dependent total cross-section":

$$\sigma_{if}^{\mu}(\omega, T, E_F) = \sum_{f>i} (n_i - n_f)\, \sigma_{if}^{\mu}(\omega). \qquad (4.39)$$

The notation of the electronic structure used in Sec. 2.3 will be used. The optical transition selection rules allow only the transitions with $\Delta m_f = 0$ in the case of $z-$polarized (growth polarized) radiation and $|\Delta m_f| = 1$ for $x-$polarized (radially polarized) radiation.

Since temperature dependence has been taken into account, one has to consider the electron population of characteristic rod states which enter the expression for the total cross section as n_i and n_f.

The first dot state is the ground state for all examined heights of the rod. If one excludes extremely tall rods, e.g. the rod with height of 60 nm, then the following states are states from the first well subband (see Fig. 2.4). Due to continual nature of the subband, relatively large number of electrons can be placed in that subband. Furthermore, one can assume that number of electrons per one rod is small enough that only the ground dot state and the lowest subband states are significantly populated, i.e. Fermi level is placed

very close to the bottom of the first subband of the well. In this case the transitions from those states to higher excited states will mostly contribute to total absorption cross section of the rod.

As all states are twofold degenerate in orbital factor space with opposite values of good quantum number m_f (note that electron spin has been incorporated into these quantum number via total angular momentum), assumption of exclusive occupation of the ground state on $T = 0$ permits no more than 2 electrons per quantum dot. We choose to calculate the absorption for 1 electron per quantum post as such level of doping was readily achievable in SAQDs [61].

The temperatures were taken to be $1K$ and $77K$. The later allows thermal population of higher states according to Fermi-Dirac distribution. The inhomogeneity of the quantum rod ensemble was taken into account by assuming a Gaussian lineshape in (4.27) as suggested in (4.25) with a standard deviation σ equal to 10% of the transition energy i.e. $\sigma = 0.1 \, (E_f - E_i)$.

4.7.1 Absorption of growth polarized radiation

It is well known that growth polarized photons are more likely to be absorbed if such excitation changes parity of the function in that direction. This can be simply explained through the simple effective mass model described by equations (4.37b) and (4.38).

For example, according to (4.37b) it is expected that the first dominant matrix element for z-polarized radiation from the ground state with quantum numbers $n_x^f = 1$, $n_y^f = 1$, $n_z^f = 1$ or s-like state, is one with different parity in the quantum numbers $n_x^f = 1$, $n_y^f = 1$, $n_z^f = 2$ or p-like state. Such excited state would have one node in growth direction. Indeed, 8-band simulation gave quantitatively the same result. The final state for the first

dominant transition from the ground state (a dot state in this case) also has one node in growth direction (also a dot state). The same rule applies for transition between subbands of the well. For example, the first dominant matrix elements are from states with quantum number $n = 1$ with no nodes in growth direction to ones with $n = 2$ with one node in growth direction, see (4.38). As seen in Fig. 2.4, the dominant dipole matrix elements are mostly between states A with different parity index, e.g. between A_1 and A_2, and between subbands B and C or C and D.

The equation (4.37b) shows that an increase of the dot height decreases the momentum matrix element and increases corresponding cross section increment. As seen from equations (4.37a), (4.37b) and (4.38), components of momentum matrix elements depend only on the corresponding dimensions of the structures. The dimensions of quantum dot are fixed and only the growth direction dimension is varied, hence only variation of absorption properties of growth polarized radiation can be examined using the simple model. This simple model is also in agreement with the 8-band model simulation results.

To conclude, the leading transitions caused by absorption of the growth polarized incident radiation are from ground state to the p-like dot state and from the first subband to the next subband with different parity and its intensity decreases by increasing the height and destination state with the different parity.

The leading transitions are not entirely responsible for peaks of optical cross section at higher temperatures as other transitions from higher states in quantum dot can also significantly contribute. This contribution has low impact on the peaks positions of the total cross section for z-polarized radiation. That implies that dominant transitions from higher states have similar

transition energy to the as the dominant transition from the ground state. This is a direct consequence of the fact that all dominant transitions are between states of different parity, and the energy separation between any two dot or well states with different parity is approximately same. However, taller rods have smaller energy separation which reduces the energy of photons involved in the absorption. The conclusion is clear, tunability of the absorption of growth-polarized radiation would be possible by changing the height of the rod structure.

That completely explains the cross section calculated by using the Eq. (4.39) and presented on Figs. 4.1 and 4.2. For $T = 0K$ only transitions from
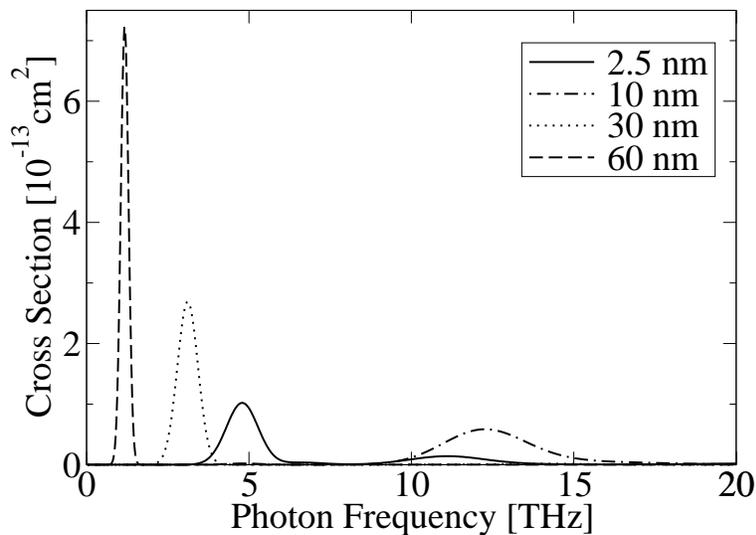
Figure 4.1: Cross Section for growth polarized radiation for $T = 0K$ and four different heights of the rod. Peaks have monotonic behavior in terms of rod heights, except for the shortest rod due to different nature of the dominant optical transition. The Figure taken from Ref. 3.

the dot bound state occurs (for maximum two electrons per dot) to the same type state with different parity. It has been argued in Sec. 2.3.2 that such dot state with different parity is p-like state, very likely positioned within the
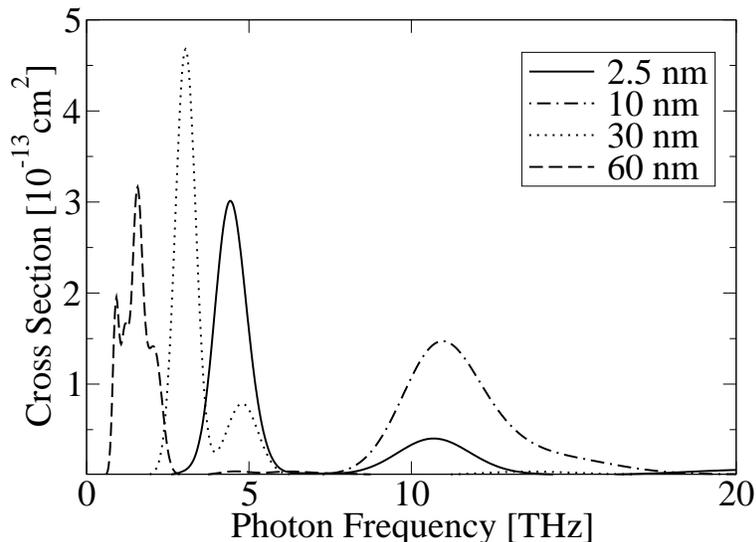
Figure 4.2: Cross Section for growth polarized radiation tailored by bound state to bound state transitions for $T = 77K$. The Figure taken from Ref. 4.

well continuum. Therefore, one can state that growth polarized radiation can effectively induce transitions to the well states due to expected strong coupling between p-like BIC and surrounding well subband continuum.

The monotonic behavior of the peaks of the absorption for taller rods is observed due to monotonic energy separation of the s-p transition. However for shorter rods, p-like state does not exist and dominant transition is bound-continuum like and due to such different nature of the transition the shortest rod does not obey regular monotonic behavior of higher rods.

At elevated temperature, i.e. $T = 77K$, an additional transition occurs from the first well subband but they are on similar energies as transitions from the bound state and are also shifted in the same manner. Therefore, Figs. 4.1 and 4.2 look similar to each other.

It is important to outline that inhomogeneous broadening of the transitions was taken as 10 percent of the energy separations of the transitions.

Because of this, absorption lineshapes due to lower energy transitions are more sharper and higher and this is not related to the oscillator strength of the transitions.

4.7.2   Absorption of in-plane polarized radiation

The important issue in quantum well intraband photodetectors is that there is no absorption for in-plane polarized radiation which can be quantitatively explained using Eq. (4.38). It is expected that quantum rods will have non-zero absorption for in-plane polarized radiation due to the dot presence.

According to Eq. (4.37a), (4.37b) and (4.38) only transitions from dot states can contribute significantly to absorption of radially polarized radiation. Hence, those transitions are restricted from states with quantum number $m_f = 1$ and $m_f = -1$ to higher states, in line with selection rules, because significantly populated dot states exist only for the $m_f = 1$ and $m_f = -1$ (see Fig. 2.4). Possible dot states with higher values of m_f are not observed in the simulation, and therefore absorption of radially polarized radiation, in this case, cannot be supported by dot-state to dot-state transitions.

This detailed examination of dominant momentum matrix elements in the structure shows that transitions between bound states in the dot and higher well states due to the absorption of in-plane polarized radiation, are the most prominent ones.

The restriction has been made to absorption from lower states and since transitions from the first subband are not allowed due to selection rules for the in-plane polarized radiation, all absorption comes from transition from the first bound state. The bound-to-subband absorption peak is tunable with dot height and results of calculation of the total cross section are pre-

sented in Figure 4.3. Absorption peaks of bound-to-subband transitions are
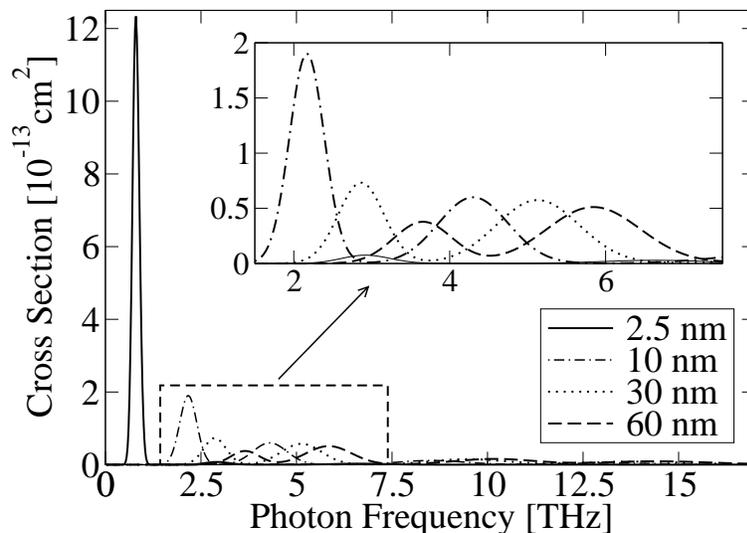
Figure 4.3: Cross Section for in-plane polarized radiation for $T = 0K$. The Figure taken from Ref. 4.

also tunable with rod height as for the growth-direction polarized radiation. Calculations show that corresponding momentum matrix elements are larger when increasing the dot height, opposite to the case of absorption of the growth direction polarized radiation.

This opposite direction of the tunability of absorption peaks for different polarized radiation creates an opportunity to engineer the structure with certain hight-to-diameter aspect ratio in order to obtain optimal functionality for both direction of incident radiation in the terahertz frequency range.

4.7.3 Optical Properties of the BIC

Intraband resonances of quantum rods were experimentally investigated in Ref. [101], where the rods were charged with several electrons, enough to completely fill the 3D confined states below the well barrier. Authors then

used growth-polarized radiation to excite electrons, and they recognized a clear difference between well and dot resonances. The leading rod resonance comes from transition from excited and fully charged rod states to unoccupied states higher in the conduction band. However, authors in Ref. [101] argued that electron-electron interaction in fully charged rods shifts the bound electronic states to higher energies. Detailed theoretical examination of that situation is required due to electron-electron interaction which is responsible for perforation of the 2-D electron gas, i.e. continuum. Nevertheless, the short lifetime of the BIC via fast scattering into the well subband was also indicated in Ref.[101]. It is intuitively clear that such fast scattering occurs due to the availability of the continuum of free states around the energy of the BIC.

Altogether, one can conclude that carriers from the bound state of the quantum rod can be efficiently scattered into the continuum of the well by strong optical resonance, i.e. ground state-BIC transition followed by efficient coupling between the BIC and surrounding continuum states. The similar effect, where strong optical resonance can trigger ionization from bound-like state to continuum state where carriers can freely move was explained in Ref. [150] for the case of 1-D supercrystal formed of the vertically stacked self-assembled quantum dots. Specifically, first supercrystal miniband occurs in the barrier gap and second one in the conduction band. Optical transitions between these two minibands are strong since those minibands were formed of s-like and p-like states respectively. Therefore, this structure, if constructed as a solar cell, exhibits increased efficiency due to strong transitions between first miniband buried in the barrier gap and second miniband buried within the conduction band continuum. In addition, strong optical transitions between below-the-barrier and above-the-barrier

(so called Bragg confined) bound states were observed experimentally in Ref. [109] in a Bragg-confined quantum well structure.

These exotic optical properties of the BIC could allow experimental observation of the BIC and associated effects. The simplest version of such an experiment is based on doped structures with up to one electron per rod. In such a case, intraband optical transitions at low temperatures are limited to the transitions from the ground state. One could measure the absorption of far-infrared light in such doped quantum rods at low temperatures for two linearly polarized directions of incident light. We have also shown in Ref. [4] that radially polarized light can excite the electron from the same ground dot state to the first well subband. This transition is not expected to be a single broadened line due to the continuum of the well subband, but resonances are expected to start at an energy corresponding to the bottom of the first subband of the well. If these resonances for the radially polarized radiation were at lower energy than the first resonance for the growth-polarized radiation, this would present a clear evidence that the excited bound state has a higher energy than the minimum of the well subband, proving the existence of BIC.

4.7.4   Polarization Independent THz Photodetector

Conclusions from previous sections are that dominant optical transitions from the ground state in quantum rods are to the first subband of the well. Growth polarized radiation induces such transition indirectly via p-like dot BIC state while radially polarized radiation induces such transitions directly to the same subband.

A possible application of these effects is construction of the polarization independent THz photodetector. If an electron, excited into the BIC,

efficiently scatters into the well subband, as indicated in Ref.[101], then a radially directed electric field can be used for efficient transport of carriers in the lateral direction. Strong optical resonance for the growth-polarized radiation is due to bound-to-bound transition and efficient transport can occur via radially free state channels around the excited bound state. On the other hand, for radially polarized incident radiation, carriers are excited directly into the well subband, from which they can be easily extracted by a lateral electric field. Therefore, strong resonance and efficient transport can be obtained for either polarization of the incident light, paving the way for polarization-independent terahertz detector. Such a detector is schematically depicted in Fig. 4.4. Contacts are positioned so to provide a lateral electric field. Upon absorption of the incident radiation the electron concentration in the well increases and leads to a photocurrent. However, strong reverse process was indicated in Ref. [100] that carriers in the conduction band of the well and bulk also efficiently scatter into the rod which can degrade the effect of detection. Therefore, this proposition for the efficient photodetector utilizing bound-to-BIC transition still needs to be carefully examined and some future work should be assigned to this issue.
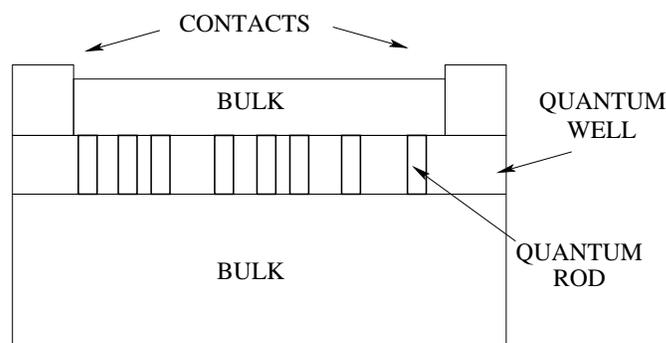
Figure 4.4: Illustration of the polarization-independent terahertz photodetector. In this geometry, the electric field due to the bias on contacts is in the lateral direction. The Figure taken from Ref. 3.

4.8 Intraband Laser based on SAQDs

It was pointed out in the Sec. 1.4.2 that SAQDs are in the research focus regarding the possible application as active media for intraband lasing. Brief overview of physical mechanisms regarding lasing was presented as well. The polaronic nature of carriers was explained in Sec. 3.1 involving s-like and p-like electronic bound states and their coupling to bulk phonons of polar type. The aim of this section is to examine optical properties of SAQDs based on the resonant s-p like transition which might be used for lasing in future designs of the QD intersublevel emitter as indicated in Chapter 1. Even if this is not true, consideration to this transition and the derived theory can be applied to other cases with a few modifications.

It has been demonstrated in Sec. 3.1.4 that the electron–phonon interaction remains the fundamental factor governing excited carrier non-radiative relaxation in QDs. Non-radiative relaxation reduces inversion population needed for lasing. On the other hand strong optical transition favors the lasing process. Therefore it would be very good to establish the connection between non-radiative relaxation mechanism and photon emitting mechanism based on s-p like optical transition.

The main aim of this work is to develop a simple model to establish a relationship between the radiative and the non-radiative transition strengths of carriers in QDs. The basis for it is, a similar physical electromagnetic interaction between electrons and phonons, and electrons and photons.

After establishing the connection between these relaxation mechanisms, the model will then be used to derive important conclusions on the geometrical and compositional optimization of QDs as possible active media.

4.8.1 The Relationship between Electron-Phonon and Electron-Photon Interaction

Since one is interested only in s-p like resonant coupling we introduce a reduction of the one-electron subspace into only two isolated states, performing lasing. Those electronic states will be further labeled with $|\psi_a\rangle$ and $|\psi_b\rangle$, or shortly $|a\rangle$ and $|b\rangle$, with energies E_a and E_b.

In this, two level system, the most important parameter regarding the electron-light interaction in dipole approximation is coordinate matrix element $\mathcal{R}_{\mathrm{ab}} = \int \mathrm{d}^3 r \psi^{(a)*}(r) \hat{r} \psi^{(b)}(r)$ or so called "dipole coupling vector". On the other hand, the same parameter for the Fröhlich interaction of the electron with the LO phonon mode with wavevector $\boldsymbol{k}$ is $\mathcal{H}_{\mathrm{ab}}^{\boldsymbol{k}} = \int \mathrm{d}^3 r \psi^{(a)*} \frac{e^{i\boldsymbol{k}\cdot\boldsymbol{r}}}{k} \psi^{(b)}$ and will be referred to as a "Fröhlich coupling function" (FCF) on wavevector $\boldsymbol{k}$. The main aim here is to find a relationship between the dipole coupling vector $\mathcal{R}_{\mathrm{ab}}$ and Fröhlich coupling function $\mathcal{H}_{\mathrm{ab}}^{\boldsymbol{k}}$.

In quantum dots, due to confinement, the Fröhlich coupling function falls rapidly to zero even for relatively small values of wavevector $\boldsymbol{k}$. It behaves as a distribution function with p-orbital-like shape with the maximum value in the limit $k \to 0$. With the aim of estimating this value, one has to expand the expression for the Fröhlich coupling function as:

$$
\begin{aligned}
\mathcal{H}_{\mathrm{ab}}^{\boldsymbol{k}} &= \int \mathrm{d}^3 r \psi^{(a)*} \frac{\cos \boldsymbol{k}\cdot\boldsymbol{r}}{k} \psi^{(b)} + i \int \mathrm{d}^3 r \psi^{(a)*} \frac{\sin \boldsymbol{k}\cdot\boldsymbol{r}}{k} \psi^{(b)} = \qquad (4.40)\\
&= \frac{1}{k} \int \mathrm{d}^3 r \psi^{(a)*} \psi^{(b)} + i\boldsymbol{e_k} \cdot \int \mathrm{d}^3 r \psi^{(a)*} \boldsymbol{r} \psi^{(b)} -\\
&\quad - \frac{k}{2} \int \mathrm{d}^3 r \psi^{(a)*} (\boldsymbol{e_k} \cdot \boldsymbol{r})^2 \psi^{(b)} - i\frac{k^2}{6} \int \mathrm{d}^3 r \psi^{(a)*} (\boldsymbol{e_k} \cdot \boldsymbol{r})^3 \psi^{(b)} + \cdots,
\end{aligned}
$$

where the second equation represents the Taylor series of sine and cosine functions, and $\boldsymbol{e_k} = \frac{\boldsymbol{k}}{k}$.

Given that electronic states $|\psi_a\rangle$ and $|\psi_b\rangle$ are states with a dominant optical transition, i.e. the intensity of the dipole coupling vector between these two states, $\mathcal{R}_{\text{ab}}$, is significant then, in most cases, one concludes that states $\psi^{(\text{a})}$ and $\psi^{(\text{b})}$ have well defined and opposite parity. Therefore, in such a case, the first term in equation (4.40) vanishes and one gets:

$$\mathcal{H}_{\text{ab}}^{\boldsymbol{k}} = i \left(\boldsymbol{e_k} \cdot \mathcal{R}_{\text{ab}} - \frac{k^2}{6} \int \mathrm{d}^3\boldsymbol{r}\psi^{(\text{a})*} \left(\boldsymbol{e_k} \cdot \boldsymbol{r} \right)^3 \psi^{(\text{b})} + \cdots \right). \qquad (4.41)$$

In the limit $k \to 0$ expression (4.41) becomes:

$$\mathcal{H}_{\text{ab}}^{\boldsymbol{k}} = \boldsymbol{e_k} \cdot \mathcal{R}_{\text{ab}}. \qquad (4.42)$$

Hence, the maximum at $k \to 0$ of the scalar field $\mathcal{H}_{\text{ab}}^{\boldsymbol{k}}$ is proportional to the intensity of the dipole coupling vector.
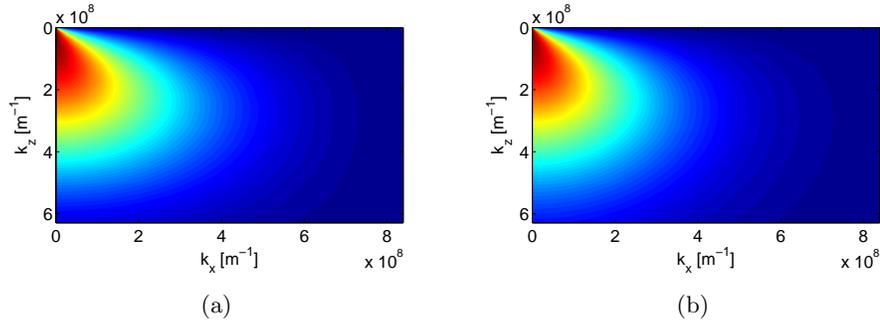
Figure 4.5: a) The Fröhlich coupling function for a hard-wall box calculated in the $k_x - k_z$ plane. The height of the dot is 20 nm and the square basis side is 15 nm and b) The Fröhlich coupling function modeled by a Gaussian with fitted linewidth inversely proportional to the dot dimensions of the hard walled QD. The whole Gaussian is multiplied by the cosine of the angle between $\boldsymbol{k}$ and k_z. Model function is approximately the same for long wavelengths where both functions have the most significant values. However, the difference increases by increasing the wavevector $\boldsymbol{k}$ where these functions have low values and therefore that domain is less important. The Figure taken from Ref. 5.

It should be pointed that the FCF is singular at $k = 0$, and also the vector $\boldsymbol{k}$ does not have a defined direction, and therefore the expression $\boldsymbol{e_k} \cdot \boldsymbol{\mathcal{R}}_{\mathrm{ab}}$ is not defined. However, the factor $\boldsymbol{e_k} \cdot \boldsymbol{\mathcal{R}}_{\mathrm{ab}}$ indicates that even for small k the distribution $\mathcal{H}_{\mathrm{ab}}^{\boldsymbol{k}}$ has a strongly anisotropic behavior. For $\boldsymbol{k}$ pointing in the direction of the dipole coupling vector, the FCF exhibits the weakest negative slope. This slope is increasing with increasing angle between $\boldsymbol{k}$ and the dipole coupling vector and decays rapidly to zero when $\boldsymbol{k}$ becomes almost perpendicular to the dipole coupling vector. In the limit where $\boldsymbol{k}$ is exactly perpendicular, the FCF is zero. All these features prove that the FCF has a p-orbital like shape. This was indeed expected, since the FCF is essentially a Fourier transform of an even function.

One can demonstrate these statements by taking a simple example of a hard-wall cuboid quantum dot where it is possible to calculate analytically $\mathcal{H}_{12}^{\boldsymbol{k}}$ between the ground and the first excited state. The results for the quantum box of height 20 nm and square basis side of 15 nm are presented in Fig. 4.5(a) in the $k_x - k_z$ plane without losing generality. The FCF behaves in the same way in the direction k_x as in k_y, for a square base case.

Therefore, we can model the Fröhlich coupling function by a bell-shaped distribution function, with the maximal value at $k \to 0$ proportional to the intensity of the dipole coupling vector and multiplied by the $\frac{k_i}{k}$, where i denotes the direction of the dipole coupling vector. This model gives:

$$\left| \mathcal{H}_{\mathrm{ab}}^{\boldsymbol{k}} \right| = |\boldsymbol{\mathcal{R}}_{\mathrm{ab}}| \, \frac{k_z}{\sqrt{k_x^2 + k_y^2 + k_z^2}} \mathcal{I}\left(\boldsymbol{k}\right), \qquad (4.43)$$

where $\mathcal{I}\left(\boldsymbol{k}\right)$ is the anisotropic distribution function with maximum $\mathcal{I}\left(0\right) = 1$. Therefore, we have parametrized the FCF via two factors. One is the dipole coupling vector $\boldsymbol{\mathcal{R}}_{\mathrm{ab}}$ which is a well known spectroscopic quantity,

and the second is the distribution function with the property $\mathcal{I}(0) = 1$. All details of the quantum dot are hidden in the width and lineshape of this function. It has been shown in Eq. (3.32) that the most important quantity regarding non-radiative relaxation is the Fröhlich coupling constant (3.25) which is in fact the integral over FCF. This is why the exact lineshape has a limited significance. On the other hand, we will show that widths of the distribution functions are closely related to the size of the quantum dot in the corresponding direction.

4.8.2 Influence of QD Geometry and Composition

In the following a quantitative description of the influence of the QD confinement on the value of FCF consisted of two factors distribution function and dipole coupling vector is given. Consider first the distribution function. Anisotropy of this function stems from the dimensional anisotropy of the dot. Thus, for anisotropic QDs the linewidth of such a distribution function varies with the direction in $\boldsymbol{k}$-space.

The Fröhlich coupling function can be thought of as a Fourier transform of the product of wave functions in the ground and excited state divided by k. By varying the dot dimensions we can shrink or expand the envelope wave functions. This can be modeled by:

$$\psi(x, y, z) \rightarrow \sqrt{\alpha_x \alpha_y \alpha_z} \psi(\alpha_x x, \alpha_y y, \alpha_z z) \tag{4.44}$$

Using these scaled wave functions in the Fröhlich coupling function, and taking a particular direction, e. g. "x"-direction, (i.e. setting $k_y = k_z = 0$)

one concludes that the FCF has the behavior:

$$\mathcal{H}_{\mathrm{ab}}\left(k_x, 0, 0\right) \rightarrow \frac{1}{\alpha_x} \mathcal{H}_{\mathrm{ab}}\left(\frac{k_x}{\alpha_x}, 0, 0\right) \tag{4.45}$$

However, the prefactor $\frac{1}{\alpha_x}$ is already included in the scaling of the dipole coupling vector, and therefore only the scaling of the distribution function width has to be considered further. By increasing the dot size in the chosen direction one can decrease the distribution function width in that direction. However, this trend remains up to some minimal, critical size in a particular direction. Beyond this point, the envelope wave function does not shrink any further, but instead starts leaking outside the dot. In the hard-wall example, it is possible to use a Gaussian without a normalization pre-factor as a distribution function. The results of such a model are presented in Fig. 4.5(a). The width of the Gaussian is inversely proportional to the dot extension in the corresponding direction. The modeling by the Gaussian curve is also the exact solution for a parabolic QD (See Appendix of Ref. [60]).

For calculations with better accuracy one uses an 8-band $\boldsymbol{k} \cdot \boldsymbol{p}$ method with strain effects included (see Sec. 2.1.2) to calculate the Fröhlich coupling function and demonstrate its dependence on the dot size. In Figs. 4.6(a) and 4.6(b), the calculated FCF for lens shaped dots of height 8nm, indium content 1 and radius 22 nm are presented. The second dot is twice as high, 16nm, and one notes that FCF has accordingly shrunk twofold in this direction. The In content in the QD also affects the width of the distribution function. By decreasing the In content, the QD potential well as well as the confinement is decreased. The wave functions then expand and the FCF consequently shrinks, and so does the distribution function. This is demonstrated in Figs. 4.7(a) and 4.7(b), where two geometrically identical
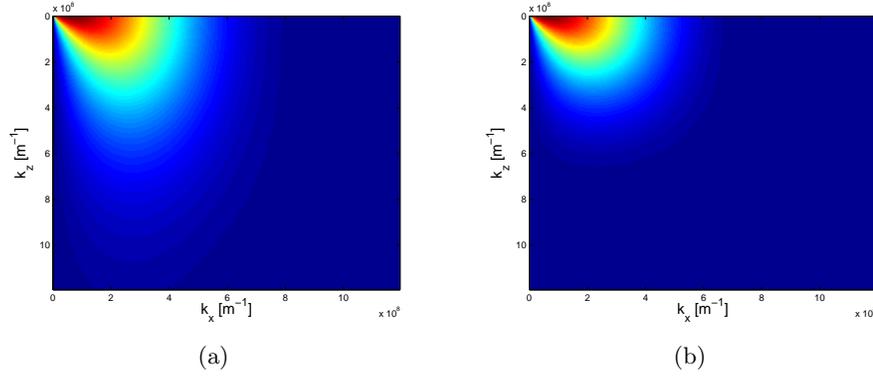
Figure 4.6: FCF for two different lens shaped cylindrically symmetric QDs calculated in the $k_x - k_z$ plane by the 8-band $\boldsymbol{k} \cdot \boldsymbol{p}$ method with strain effects included. Indium content in both dots is 1, radius is 22 nm and their height is a) 8 nm and b) 16 nm. The Figure taken from Ref. 3.

QDs (cylinder shaped) have different In content, of 1 and 0.6 respectively. We note that FCF in Fig. 4.7(b) is slightly narrower than that in Fig. 4.7(a). It is expected that the maximal possible width of the distribution function in terms of QD depth occurs for the hard-wall QD, since it has infinite potential well. The opposite limit occurs in bulk, where the width is zero, i.e. the wave function is a pure plane wave. It is difficult to predict a more accurate dependence of the width of the distribution function, but a monotonic behavior is expected between these two limits.

In summary, four parameters have been introduced: $\alpha_x, \alpha_y, \alpha_z$ and σ. The first three parameters measure the relative QD extension in a specified direction, and the parameter σ is an increasing function of the In content in QD. By varying these geometrical parameters the distribution function evolves as:

$$\mathcal{I}\left(k_x, k_y, k_z\right) \rightarrow \mathcal{I}\left(\frac{\alpha_x}{\sigma} k_x, \frac{\alpha_y}{\sigma} k_y, \frac{\alpha_z}{\sigma} k_z\right) \tag{4.46}$$

(a) (b)
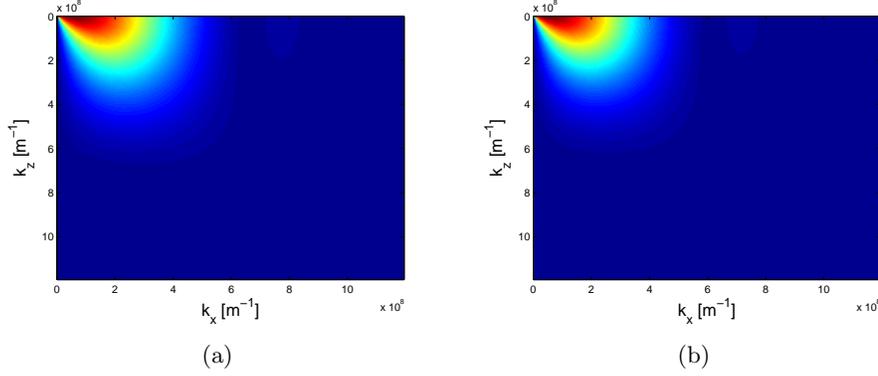
Figure 4.7: a) FCF for two different cylinder shaped QDs calculated in the $k_x - k_z$ plane by the 8-band $\boldsymbol{k} \cdot \boldsymbol{p}$ method with strain effects included. Indium content in dots is a) 1 and b) 0.6, and their radius and height are 22 nm and 12 nm, respectively, in both cases. The Figure taken from Ref. 5.

and consequently the coupling integral constant evolves as:

$$S \to \int \mathrm{d}^3 \boldsymbol{k} \frac{k_z^2}{k_x^2 + k_y^2 + k_z^2} \mathcal{I}\left(\frac{\alpha_x}{\sigma} k_x, \frac{\alpha_y}{\sigma} k_y, \frac{\alpha_z}{\sigma} k_z\right) \tag{4.47}$$

which gives:

$$S \to \frac{\sigma^3}{\alpha_x \alpha_y \alpha_z} \int \mathrm{d}^3 \boldsymbol{k} \frac{k_z^2}{\left(\frac{\alpha_z}{\alpha_x}\right)^2 k_x^2 + \left(\frac{\alpha_z}{\alpha_y}\right)^2 k_y^2 + k_z^2} \mathcal{I}\left(\boldsymbol{k}\right) = \frac{\sigma^3}{\alpha_x \alpha_y \alpha_z} S' \tag{4.48}$$

Eq. (4.48) describes the variation of the coupling integral constant in terms of quantum dot geometric and composition parameters. The largest contribution comes from the pre-factor. Coupling integral constant S is slightly different from S', i.e. it differs only by the "cosine part". In the case of an isotropic enlargement of the QD size, the "cosine part" in the integrals remains unchanged and therefore so do the constants S and S'.

4.8.3   Light Absorption and Stimulated Emission

The polaron ground state is $|1\rangle$ with the dominant component being the electron ground state. In the case of $\delta_- < 0$, the first excited polaron state is $|2\rangle$. As expected, the dominant component of that state is the first excited electron state, which enables efficient optical excitation of that polaron state from the ground state. Therefore, when dealing with optical excitation, we will omit the polaronic nature of the carriers in QDs and will derive expressions for the quantities of interest with pure electronic notation. Later, we will only replace the electronic notation with the corresponding polaronic notation. Let the system be described semiclassically, with particular interest in estimating the transition rate between the lower state $|a\rangle$ with energy E_a and the higher state $|b\rangle$ with energy E_b. Within this semiclassical approach, Fermi's Golden rule transition rate can be used to find the coefficients of absorption and stimulated emission gain in the active medium. The optical cross section gives the absorption line and gain when multiplied by the population difference. With the "$-e\hat{r} \cdot \boldsymbol{E}$" interaction the expression for optical cross-section reads [151]:

$$\sigma_{ab}^{\varepsilon}(\omega) = \frac{4\pi |e|^2 \omega}{\overline{n}\varepsilon_0 c m_0^2} \, |\boldsymbol{\mathcal{R}}_{ab} \cdot \boldsymbol{\varepsilon}|^2 \, g\left(E_b - E_a \mp \hbar\omega\right), \qquad (4.49)$$

where $g\left(E_b - E_a \mp \hbar\omega\right)$ is the normalized distribution function (e.g. Gaussian profile), recovering the inhomogeneous broadening due to the size inhomogeneity of the quantum dot ensemble and $\boldsymbol{\varepsilon}$ is the light polarization unit vector. Constants e, m_0, $\overline{n}$ and c are electron charge and mass, refractive index of the quantum dot and speed of light. The sign "$-$" corresponds to absorption and "$+$" to emission.

4.8.4 Lasing Efficiency

In order to consider a transition as a possible lasing transition, both the radiative and non-radiative lifetimes are important. The longer the non-radiative lifetime, the higher is the likelyhood of photon emission. Thus, we define a figure of merit for such a transition as the ratio of the optical cross-section and the non-radiative transition rate for the light polarized along the dipole coupling vector $K_{\mathrm{ab}}(\omega) = \frac{\sigma_{\mathrm{ab}}(\omega)}{\Gamma(E_i)}$. By using the equations (4.27) and (3.32) the lasing figure of merit becomes:

$$K_{\mathrm{ab}}(\omega) = \frac{64\pi^4 g(E_i \mp \hbar\omega)}{\overline{n}\varepsilon_0 c m_0^2 \hbar^2 \omega_{\mathrm{LO}} \left(\frac{1}{\epsilon_\infty} - \frac{1}{\epsilon_{st}}\right)} \frac{\delta_-^2}{S(E_i)} \frac{E_i}{\Gamma_{\mathrm{ph}}} \qquad (4.50)$$

The inhomogeneous broadening $g(E_i \mp \hbar\omega)$ clearly affects this laser efficiency coefficient, via the optical cross section. Increasing the inhomogeneous broadening width will decrease the laser efficiency for a specific frequency of light.

The ratio $\frac{E_i}{\Gamma_{\mathrm{ph}}}$ is proportional to $\frac{1}{E_i^n}$, where n is an integer depending on the active decaying channel. A detailed discussion on this subject is presented in [133], but general conclusion is that a decrease of polaron s-p like splitting E_i will lead to improved lasing efficiency.

Dot enlargement and a reduced In content also lead to a decrease of the quantity S, as explained in the previous section. Furthermore, the squared detuning δ_-^2 then increases and leads to improved lasing efficiency.

It is clear now that novel post-fabrication techniques such as rapid thermal annealing [18], or quantum rod elongation [1, 21] could produce structures with higher lasing efficiency coefficient. One can enlarge the dot, or reduce the In content by using those techniques. In Ref. 61, it has been demonstrated that the non-radiative polaron lifetime is increased by rapid

thermal annealing. However, we have shown here that this does not affect adversely the radiative lifetime, thus increasing the overall figure of merit 4.50.

In summary, the relationship between two entities has been established. One is electron-phonon interaction responsible for non-radiative lifetime and dipole matrix element responsible for the cross-section of the optical transition. Both, non-radiative lifetime and the cross-section of the optical transition are very important quantities for lasing and can be related by using the established relationship. The relationship is based on the fact that dipole matrix element is proportional to both electron-phonon interaction in QDs and to the optical cross-section of the optical transition. This relationship can be exploited in many ways. The proper figure of merit, defined as the ratio of the optical cross-section and the non-radiative transition rate can be then analyzed without knowing the value of dipole coupling vector and thus avoiding the more microscopic approach. The another way for this relation to be exploited is to test the proposed theory of non-radiative decaying of the excited polarons via anharmonicity driven scattering by measuring the strength of luminescence and extracting the value of dipole coupling vector from it. Then the value of dipole coupling vector can be used in order to estimate the strength of the electron-phonon coupling directly.

Chapter 5

Transport Properties of CQD supercrystals

The significance of the potential applications of CQD supercrystals together with state of the art experimental achievements have been elaborated in Chapter 1. The scope of this chapter is to build a model of CQD supercrystal and to study transport properties of such system with the emphasis on the electron–phonon interaction.

The model of CQD supercrystal is readily accepted in tight binding spirit [152, 92, 31, 85]. This means that electrons are localized in each dot, but may hop to adjacent dots under applied electric field. The other possibility is that electron cloud of each site is significantly spread around adjacent sites giving rise to the band-like conductivity due to supercrystal periodicity as reported in Refs. 7, 6, 86.

In order to study effect of electron–phonon interaction on transport properties one has to assume that carrier population in the considered system is very low in order to remove effects of electron–electron interaction and one has to obtain all modes in single quantum dot contributing significantly

to electron–phonon coupling as done in Sec. 3.2. Transport properties for low carrier concetrations can be studied experimentally as well [6, 7] which justifies theoretical approach for low carrier concentrations.

Electron-phonon coupling strengths seem strong according to the data presented in Tabs. 3.1 and 3.2. Among other mechanisms, electron–phonon coupling may be the main mechanism which enhances hopping between different sites, but at the same time prevents band-like conduction. However, this expectation has to be proven within the detailed theoretical consideration and that is the main aim of this chapter.

Outline of this chapter is the following. Firstly, linear response theory of electron conductance due to applied external electric field is presented. Then the many-body model of CQD supercrystal is introduced and an approximate diagonalization formalism within the framework of variational polaron theory is performed. Such an approach treats equally all possible cases of input parameters of the model and provides the nature of coupling in the model. Finally, armed with optimal representation of the model, mobilities of carriers in CQD supercrystals are readily obtained and nature of charge transport is discussed.

Accurate calculation and qualitative examination of carrier mobilities in CQD supercrystals made of polar compounds is the main contribution of this chapter. It gives readily experimentally measurable temperature vs mobility curve. Applied approximations to the model are justified from the experimental point of view, such as low carrier concentration approximation. Therefore, obtained results can be compared to available experimental data on the issue and it is done so in this chapter.

5.1 Hamiltonian of Interaction

Experimentally, charge transport is studied by applying an AC electric field to the sample, inducing the currents. The applied electric field determines the vector magnetic potential in the Coulomb gauge and without external charges ($\phi = 0$):

$$\boldsymbol{A}(t) = \frac{i}{\omega}\boldsymbol{E}_0 e^{i\boldsymbol{q}\cdot\boldsymbol{r} - i\omega t}. \tag{5.1}$$

The microscopic one-electron Hamiltonian of interaction of electrons with electromagnetic field [134, 153] for the case $\phi = 0$ in Coulomb gauge is obtained from Eq. (4.1) and it reads

$$\hat{H} = \frac{(\hat{\boldsymbol{p}} + e_0\boldsymbol{A})^2}{2m_0} + V_0(\boldsymbol{r}). \tag{5.2}$$

Interaction Hamiltonian is defined as

$$\hat{H}' = \frac{(\hat{\boldsymbol{p}} + e_0\boldsymbol{A})^2}{2m_0} - \frac{\hat{\boldsymbol{p}}^2}{2m_0}. \tag{5.3}$$

The main interest will be in the linear response to external electromagnetic field, therefore the terms quadratic in $\boldsymbol{A}$ will be neglected. Applied electric field is usually of low frequency and can be considered as a constant in space over the studied sample in a certain moment of time. This mean that only the case $q = 0$ is relevant and interaction Hamiltonian becomes

$$\hat{H}'(t) = \frac{ie_0}{\omega m_0}\hat{\boldsymbol{p}} \cdot \boldsymbol{E}_0 e^{-i\omega t}. \tag{5.4}$$

The derived Hamiltonian of interaction can be given in terms of the

many body current operator:

$$\hat{\boldsymbol{J}} = -\frac{e_0}{m_0} \sum_n \hat{\boldsymbol{p}}_n, \tag{5.5}$$

where summation goes over all carrier particles in the considered system. The interaction Hamiltonian is then:

$$\hat{H}'(t) = \frac{i}{\omega} \hat{\boldsymbol{J}} \cdot \boldsymbol{E}_0 \mathrm{e}^{-i\omega t}. \tag{5.6}$$

Current operator is difficult to handle directly in the Fock space and it would be easier if one relates the current operator to the dipole operator which is much easier to handle. Defining the many body dipole operator as

$$\hat{\boldsymbol{\Pi}} = -e_0 \sum_n \hat{\boldsymbol{r}}_n, \tag{5.7}$$

and taking into account that $\left[\hat{r}_i, \hat{H}\right] = \frac{i\hbar}{m_0}\hat{p}_i$ where i denotes Cartesian component, the current operator is given as:

$$\hat{\boldsymbol{J}} = \frac{1}{i\hbar} \left[\hat{\boldsymbol{\Pi}}, \hat{H}\right]. \tag{5.8}$$

5.2   Kubo Formula for DC mobility

The electrical conductivity is the physical quantity which linearly relates external applied electric field with frequency ω to the induced density current. The conductivity tensor $\sigma_{\nu,\mu}(\omega)$ is defined as the ratio of the ν-th Cartesian component of the induced density current $\delta\left(\hat{j}_\nu\right)$ and μ-th Cartesian component of the applied electric field of frequency ω which induces the mentioned

current density:

$$\delta \left(\hat{j}_\nu \right) = \sum_\mu \sigma_{\nu\mu} \left(\omega \right) E_{0\mu} \mathrm{e}^{-i\omega t}. \tag{5.9}$$

The exact relation between coordinate dependent density current operator and current operator is given as $\hat{\boldsymbol{J}} = \int \mathrm{d}^3\boldsymbol{r}\,\hat{\boldsymbol{j}}\left(\boldsymbol{r}\right)$. Since one is interested in the averaged conductivity of the entire considered system one can neglect spatial dependence of the density current operator and use the following relation: $\hat{\boldsymbol{j}} = \frac{\hat{\boldsymbol{J}}}{V}$.

The mobility of the carrier in the considered system is then given as

$$\mu_{\nu\mu} = \lim_{\omega \to 0} \frac{\mathrm{Re}\left(\sigma_{\nu\mu}\left(\omega\right)\right)}{n_e e_0}, \tag{5.10}$$

where $n_e = \frac{N_c}{V}$ is electron concentration and N_c is number of all electrons in our system of volume V. The mobility is central quantity of interest as it gives the pure transport response of carriers independent of their concentration.

Conductivity tensor can be obtained from Kubo formula (4.3) for the current operator and interaction Hamiltonian (5.6):

$$\delta \left(\hat{J}_\nu \right) = -\frac{1}{\hbar\omega} \sum_\mu E_{0\mu} \mathrm{e}^{-i\omega t} \times \tag{5.11}$$

$$\times \int_{-\infty}^t dt' \mathrm{e}^{i\omega(t-t')} \left\langle \left[\hat{J}_{\mu I}\left(t'\right), \hat{J}_{\nu I}\left(t\right) \right] \right\rangle,$$

and it reads:

$$\sigma_{\nu\mu}\left(\omega\right) = \frac{1}{\hbar\omega V} \int_{-\infty}^t dt' \mathrm{e}^{i\omega(t-t')} \left\langle \left[\hat{J}_{\nu I}\left(t\right), \hat{J}_{\mu I}\left(t'\right) \right] \right\rangle. \tag{5.12}$$

Again, as in Sec. 4.3, one is interested in the component of the response in the same direction as an applied electromagnetic field. By following the

analog prescription as in Sec. 4.3 mobility defined as in Eq. (5.10) becomes:

$$\mu_{\mu\mu} = \frac{\beta}{2N_c e_0} \int_{-\infty}^{\infty} dt e^{i\omega t} \left\langle \hat{J}_{\mu I}(t) \hat{J}_{\mu I}(0) \right\rangle. \qquad (5.13)$$

5.3 The Model of CQD Supercrystal

The main aim is to calculate the mobility of the carriers in CQD supercrystals which has to be appropriately modeled. Even though current technology does not support fabrication of ideal superlattices [2, 32], and even though the lattices reported are of hexagonal type, an ideal cubic lattice of CQDs with lattice constant C will be considered. The reason of choosing the cubic type of the lattice is that it allows relatively simple theoretical treatment especially when it comes to the calculation of the free energy of the electron-phonon system (which will be done later). Also, the main interest is to study transport properties influenced by electron-phonon interaction and it is expected that qualitatively same conclusions follow for any type of the lattice. Each CQD is assumed to have the shape of a sphere with radius a in the 2.0-4.0 nm range [2, 85] that provides three dimensional confinement for electrons with infinitely high potential barrier(due to embedding insulating matrix). The interdot spacing of $d = 1$ nm is assumed, which gives $C = 2a + d$ (see 5.1). The electronic structure of a single CQD was considered within the effective mass approximation in Chapter 2. The energy separation between s-like ground and p-like first excited state in the conduction band is above 200 meV for all realistic values of dot radius a of order of few nanometers. Therefore one assumes that transport at low carrier concentrations, where the effects of charging [85, 92, 154, 152] are negligible, occurs only through ground s-like states, since these are the only ones that are significantly populated. Within the effective mass approxima-
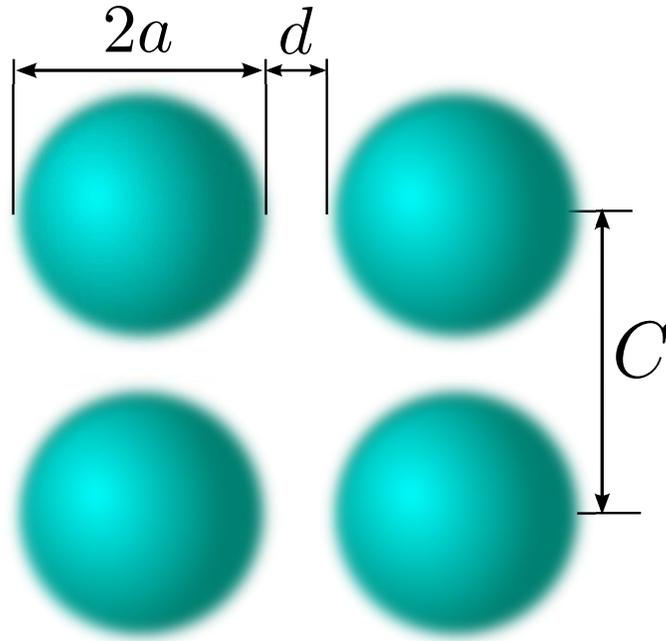
Figure 5.1: 2D sketch of a colloidal nanocrystal solid with nanocrystal radius a, interdot spacing d and lattice constant C.

tion, the s-like wave function of the ground state is given in Eq. (2.35) and it reads

$$\psi\left(\boldsymbol{r}\right) = \sqrt{\frac{1}{2\pi a^3 j_1^2\left(\alpha_{00}\right)}} j_0\left(\frac{\alpha_{00}}{a}r\right) \tag{5.14}$$

where j_n is the spherical Bessel function of order n and α_{00} is the first zero of j_0.

The electronic coupling between ground states of neighboring CQDs depends on various factors, such as the dot size, the interdot spacing, the type of ligands at the surface of the dots, as well as on the linker molecules that can be used to increase the coupling between the dots [155, 156, 82, 157, 158, 159]. Recent ab-initio calculations [155] have shown that electronic coupling in CdSe CQDs linked with Sn_2S_6 molecule strongly depends on the dot size and the type of molecule attachment and takes the values below 10 meV

for dots with the radius above 2 nm. Since the electronic coupling between the dots is the parameter that depends on many different factors and since it can be engineered, it will be used as an input fitting parameter in the presented theory and will be discussed accordingly.

The relevant phonon modes within the single CQD have been obtained in Sec. 3.2 and listed in in Tabs. 3.1 and. 3.2. A limited number of phonon modes with the strongest coupling to electrons will be included by choosing the modes with the largest ratio of electron–phonon coupling G_f and phonon energy $\hbar\Omega_f$. Confined LO phonon modes at energies of 24 meV are responsible for strongest electron–phonon coupling constants of the order of $(30 - 40)$ meV. These values are significantly larger than typical electronic transfer integrals [154] which gives a first indication that electron–phonon interaction is so strong that it entirely defines a picture of transport. Having the importance of the values of electron–LO phonon coupling constants in mind, one has to check that they are reasonable by also computing them using the bulk phonon model and taking the standard expression for Fröhlich coupling. The root of the sum of all electron–LO phonon coupling constants squared is in the range $(46 - 66)$ meV within the bulk phonon model, and in the $(31 - 44)$ meV range within the confined phonon model for the value of radius in the $(4.0 - 2.0)$ nm range. Similarity of these values suggests that the values of electron–LO phonon coupling constants obtained from the used model are in accordance with expectations.

With the obtained phonon modes, frequencies and coupling strengths, one can construct the Hamiltonian of an infinite three dimensional CQD supercrystal:

$$\hat{H} = \hat{H}_{\text{e}} + \hat{H}_{\text{ph}} + \hat{H}_{\text{e-ph}}, \tag{5.15}$$

where

$$\hat{H}_{\text{e}} = \sum_{\boldsymbol{RS}} J_{\boldsymbol{R-S}} \hat{A}_{\boldsymbol{R}}^{\dagger} \hat{A}_{\boldsymbol{S}}, \tag{5.16}$$

$$\hat{H}_{\text{ph}} = \hbar \sum_{\boldsymbol{R},f} \Omega_f \hat{B}_{\boldsymbol{R},f}^{\dagger} \hat{B}_{\boldsymbol{R},f}, \tag{5.17}$$

$$\hat{H}_{\text{e-ph}} = \sum_{\boldsymbol{R},f} G_f \hat{A}_{\boldsymbol{R}}^{\dagger} \hat{A}_{\boldsymbol{R}} \left(\hat{B}_{\boldsymbol{R},f}^{\dagger} + \hat{B}_{\boldsymbol{R},f} \right). \tag{5.18}$$

In the previous equations $\hat{A}_{\boldsymbol{R}}^{\dagger}$ and $\hat{A}_{\boldsymbol{R}}$ are the creation and annihilation operators for an electron in CQD at site $\boldsymbol{R}$, $\hat{B}_{\boldsymbol{R},f}^{\dagger}$ and $\hat{B}_{\boldsymbol{R},f}$ are the corresponding operators for a phonon mode f in CQD at the same site, while $J_{\boldsymbol{R-S}}$ is electronic coupling (electronic transfer integral) between the ground states of CQDs at sites $\boldsymbol{R}$ and $\boldsymbol{S}$. Only the coupling between nearest neighbors is included because electronic coupling between more remote neighbors is negligibly small as discussed in Ref. [92].

Now, it is possible to express the current and dipole operators defined in Eqs. (5.7) and (5.5). Coordinate matrix elements between adjacent site wavefunctions can be neglected and within such approximation the dipole operator takes the form: $\hat{\boldsymbol{\Pi}} = e_0 \sum_{\boldsymbol{R}} \boldsymbol{R} \hat{A}_{\boldsymbol{R}}^{\dagger} \hat{A}_{\boldsymbol{R}}.$ and $\boldsymbol{J}$ is just a current operator. By using the identity (5.8), one obtains the current operator in the tight binding representation: $\hat{\boldsymbol{J}} = \frac{e_0}{i\hbar} \sum_{\boldsymbol{R},\boldsymbol{S}} (\boldsymbol{R} - \boldsymbol{S}) E_{\boldsymbol{R-S}} \hat{A}_{\boldsymbol{R}}^{\dagger} \hat{A}_{\boldsymbol{S}}.$

5.4 Variational Polaron Theory

The indicated strong electron–phonon interaction in Hamiltonian (5.15) means that any direct perturbative approach for such system does not hold. Instead, changing of the eigenbasis of the electron–phonon Hilbert space by some unitary transformation is needed where the new basis would provide a good starting point for not just the perturbative approach but for even the

approximate diagonalization of the problem. For example, small polaron transformation when applied to independent boson model [122] exactly diagonalize the given model. The presented model in Eq. (5.15) is similar, but more complex than that of independent boson model and small polaron transformation could be used only for the case of strong coupling [160]. Therefore, a proper formalism has to be introduced which accounts for different possible input parameters of the Hamiltonian (5.15) such as electron–phonon coupling form factors and transfer integrals. Such a formalism should be able to answer the question whether electrons and phonons are in strong, weak or intermediate coupling regime and should provide starting basis in the electron–phonon Hilbert space which can be considered as an approximate diagonalization of the initial model (5.15).

5.4.1   Merrifield's Unitary Transformation

To establish the nature of charge carriers described by (5.15) and their transport regime, one could follow the variational polaron approach of Refs. 161, 160. The main idea in such an approach is to apply the Merrifield's unitary transformation of the Hamiltonian $\hat{H}(\boldsymbol{D}) = \hat{U}^{-1}(\boldsymbol{D})\hat{H}\hat{U}(\boldsymbol{D})$, where unitary transformation is given as

$$\hat{U}(\boldsymbol{D}) = e^{\sum_{\boldsymbol{R}} \hat{A}_{\boldsymbol{R}}^{\dagger} \hat{A}_{\boldsymbol{R}} \sum_{\boldsymbol{S},f} D_{\boldsymbol{S},f} \left(\hat{B}_{\boldsymbol{R}+\boldsymbol{S},f} - \hat{B}_{\boldsymbol{R}+\boldsymbol{S},f}^{\dagger} \right)}. \tag{5.19}$$

The coefficients $D_{\boldsymbol{S},f}$ in the unitary transformation are obtained from the condition that Bogoliubov upper bound on the free energy of the Hamiltonian $\hat{H}(\boldsymbol{D})$ is minimal [160] which is equivalent to the variational principle as explained in later paragraphs. A single variational parameter is determined by superlattice site index $\boldsymbol{S}$ and particular phonon index f. This

doesn't mean that variational parameters are assigned to each phonon mode, but polaron assigned to each lattice excitation is "dressed" by all phonon modes by the strength valued by parameter $D_{\boldsymbol{S},f}$. In numerical calculations only finite number of the coefficients $D_{\boldsymbol{S},f}$ are used. The coefficients $D_{\boldsymbol{S}=0,f}$ are expected to have the largest values and the values of other coefficients $D_{\boldsymbol{S}\neq0,f}$ are expected to decrease by increasing the $\boldsymbol{S}$. Eventually, the value of variational coefficients can be approximated as zero for sufficiently large $\boldsymbol{S}$. It is easy to show that standard small polaron transformation [122, 160] is a special case of the Merrifield's transformation (this will be elaborated in more detail later). Thus, the Merrifield's transformation can be considered as a generalization of the small polaron transformation.

Firstly, one has to explicitly derive the transformed Hamiltonian. In order to do so, one has to introduce a Wannierized Bloch basis defined with:

$$\hat{A}_{\boldsymbol{R}} = \frac{1}{\sqrt{N}} \sum_{\boldsymbol{k}} \hat{A}_{\boldsymbol{k}} \mathrm{e}^{-i\boldsymbol{k}\cdot\boldsymbol{R}} \tag{5.20}$$

$$\hat{A}_{\boldsymbol{k}} = \frac{1}{\sqrt{N}} \sum_{\boldsymbol{R}} \hat{A}_{\boldsymbol{R}} \mathrm{e}^{i\boldsymbol{k}\cdot\boldsymbol{R}},$$

and "phonon dressing" operators:

$$\hat{\Theta}_{\boldsymbol{R}}(\boldsymbol{D}) = \mathrm{e}^{\sum_{\boldsymbol{S},f} D_{\boldsymbol{S}-\boldsymbol{R},f}\left(\hat{B}_{\boldsymbol{S},f}-\hat{B}^{\dagger}_{\boldsymbol{S},f}\right)}. \tag{5.21}$$

The transformed Hamiltonian is then of the form

$$\hat{H}(\boldsymbol{D}) = \hat{H}_0(\boldsymbol{D}) + \hat{V}(\boldsymbol{D}), \tag{5.22}$$

where term $\hat{H}_0\left(\boldsymbol{D}\right)$ describes noninteracting fermions and bosons:

$$\hat{H}_0\left(\boldsymbol{D}\right) = \sum_{\boldsymbol{k}} \bar{E}_{\boldsymbol{k}}\left(\boldsymbol{D}\right) \hat{A}_{\boldsymbol{k}}^{\dagger} \hat{A}_{\boldsymbol{k}} + \hbar \sum_{\boldsymbol{R},f} \Omega_f \hat{B}_{\boldsymbol{R},f}^{\dagger} \hat{B}_{\boldsymbol{R},f}, \qquad (5.23)$$

where the following quantities have been introduced:

$$\bar{E}_{\boldsymbol{k}}\left(\boldsymbol{D}\right) = E_0 + \sum_{\boldsymbol{R}^+} J_{\boldsymbol{R}}\left(\boldsymbol{D}\right) \cos\left(\boldsymbol{k} \cdot \boldsymbol{R}\right) + E'\left(\boldsymbol{D}\right), \qquad (5.24)$$

$$J_{\boldsymbol{R}}\left(\boldsymbol{D}\right) = 2E_{\boldsymbol{R}} \mathrm{e}^{-\frac{1}{2}\sum_{\boldsymbol{R}',f}\left(\boldsymbol{D}_{\boldsymbol{R}'}-\boldsymbol{D}_{\boldsymbol{R}'-\boldsymbol{R}}\right)^2 \coth\frac{\beta\hbar\Omega_f}{2}}, \qquad (5.25)$$

and

$$E'\left(\boldsymbol{D}\right) = \sum_f \left(\sum_{\boldsymbol{R}} \hbar\Omega_f D_{\boldsymbol{R},f}^2 - 2G_f D_{0,f} \right). \qquad (5.26)$$

The second term $\hat{V}\left(\boldsymbol{D}\right)$ contains the interaction between fermions and bosons as a perturbation if the $D_{\boldsymbol{S},f}$ coefficients are chosen appropriately. This interaction term consists of two readily distinguishable terms:

$$\hat{V}\left(\boldsymbol{D}\right) = \hat{V}_1\left(\boldsymbol{D}\right) + \hat{V}_2\left(\boldsymbol{D}\right). \qquad (5.27)$$

The first interaction term is given as

$$\hat{V}_1\left(\boldsymbol{D}\right) = \frac{1}{N} \sum_{\boldsymbol{k},\boldsymbol{q}} \hat{A}_{\boldsymbol{k}+\boldsymbol{q}}^{\dagger} \hat{A}_{\boldsymbol{k}} \sum_f \Phi_{f,\boldsymbol{q}}\left(\boldsymbol{D}\right) \left(\hat{B}_{-\boldsymbol{q},f}^{\dagger} + \hat{B}_{\boldsymbol{q},f} \right), \qquad (5.28)$$

where

$$\hat{B}_{\boldsymbol{q},f} = \sum_{\boldsymbol{R}} \mathrm{e}^{i\boldsymbol{q}\cdot\boldsymbol{R}} \hat{B}_{\boldsymbol{R},f}, \qquad (5.29)$$

and

$$\Phi_{f,\boldsymbol{q}}\left(\boldsymbol{D}\right) = G_f - \hbar\Omega_f \sum_{\boldsymbol{S}} D_{\boldsymbol{S},f} \mathrm{e}^{-i\boldsymbol{q}\cdot\boldsymbol{S}}. \qquad (5.30)$$

The second interaction term is given as

$$\hat{V}_2\left(\boldsymbol{D}\right) = \sum_{\boldsymbol{k},\boldsymbol{q}} \hat{F}_{\boldsymbol{k},\boldsymbol{q}}\left(\boldsymbol{D}\right) \hat{A}_{\boldsymbol{k}}^{\dagger} \hat{A}_{\boldsymbol{q}}, \tag{5.31}$$

where

$$\hat{F}_{\boldsymbol{k},\boldsymbol{q}}\left(\boldsymbol{D}\right) = \frac{1}{N} \sum_{\boldsymbol{R},\boldsymbol{S}} E_{\boldsymbol{R}-\boldsymbol{S}} \mathrm{e}^{i(\boldsymbol{k}\cdot\boldsymbol{R}-\boldsymbol{q}\cdot\boldsymbol{S})} \times \tag{5.32}$$
$$\times \left(\hat{\Theta}_{\boldsymbol{R}}^{\dagger}\left(\boldsymbol{D}\right) \hat{\Theta}_{\boldsymbol{S}}\left(\boldsymbol{D}\right) - \left\langle \hat{\Theta}_{\boldsymbol{R}}^{\dagger}\left(\boldsymbol{D}\right) \hat{\Theta}_{\boldsymbol{S}}\left(\boldsymbol{D}\right) \right\rangle_{\mathrm{ph}} \right).$$

The average over the product of phonon dressing operators is

$$\left\langle \hat{\Theta}_{\boldsymbol{R}}^{\dagger}\left(\boldsymbol{D}\right) \hat{\Theta}_{\boldsymbol{S}}\left(\boldsymbol{D}\right) \right\rangle_{\mathrm{ph}} = \tag{5.33}$$
$$= \mathrm{e}^{-\frac{1}{2}\sum_{\boldsymbol{R}',f}\left(\boldsymbol{D}_{\boldsymbol{R}'-\boldsymbol{R}}-\boldsymbol{D}_{\boldsymbol{R}'-\boldsymbol{S}}\right)^2 \coth\frac{\beta\hbar\Omega_f}{2}}.$$

5.4.2 Variational Principle

The choice of the variational coefficients takes place through variational principle. The free energy of the system described by the full Hamiltonian should not differ significantly from the free energy described by the transformed non-interacting Hamiltonian $\hat{H}_0\left(\boldsymbol{D}\right)$. Therefore, the theory is based on the assumption that transformed Hamiltonian without perturbation (5.23) defines the approximate ground state, i.e. statistical operator of such ground state is:

$$\hat{\rho}_0\left(\boldsymbol{D}\right) = \frac{\mathrm{e}^{-\beta\hat{H}_0(\boldsymbol{D})}}{\mathrm{Tr}\left(\mathrm{e}^{-\beta\hat{H}_0(\boldsymbol{D})}\right)}. \tag{5.34}$$

It is important to emphasize that fermionic part of the non-interacting transformed Hamiltonian includes phonon parameters from the starting model

Hamiltonian and therefore it introduces polaronic features into the formalism even without the interaction part.

The free energy of the system is invariant under unitary transformation and Gibbs-Bogoliubov inequality for free energy holds for any such transformed Hamiltonian and for any trial statistical operator ρ_t:

$$F = -k_B T \ln \text{Tr} \left(e^{-\beta \hat{H}} \right) = \tag{5.35}$$
$$= -k_B T \ln \text{Tr} \left(e^{-\beta \hat{H}(\boldsymbol{D})} \right) \leq$$
$$\leq \text{Tr} \left(\hat{\rho}_t \hat{H} \left(\boldsymbol{D} \right) \right) + k_B T \text{Tr} \left(\rho_t \ln \rho_t \right).$$

Setting the trial approximate solution of a transformed Hamiltonian in the form of $\hat{\rho}_0 \left(\boldsymbol{D} \right)$ and taking into account that the interaction term in (5.22) has the property:

$$\text{Tr} \left(\hat{\rho}_0 \left(\boldsymbol{D} \right) \hat{V} \left(\boldsymbol{D} \right) \right) = 0, \tag{5.36}$$

the inequality (5.35) becomes:

$$F = -k_B T \ln \text{Tr} \left(e^{-\beta \hat{H}(\boldsymbol{D})} \right) \leq \tag{5.37}$$
$$\leq -k_B T \ln \text{Tr} \left(e^{-\beta \hat{H}_0(\boldsymbol{D})} \right).$$

This inequality provides the basis for the optimization of parameters $\boldsymbol{D}$ by minimizing the right-hand side of (5.37) which presents the upper bound of free energy of the considered Hamitlonian. By using this procedure, one obtains the optimal unitary transformation, for which we assumed in advance, it will give optimal separation between interacting and non-interacting term, so the whole problem can be treated perturbatively. Also, such an optimization process gives the optimal separable statistical operator $\hat{\rho}_0 \left(\boldsymbol{D}_{\text{opt}} \right)$ which will be only used in order to obtain thermodynamic averages.

There is no certain physical argument that this formalism can enable a perturbative approach for all possible input parameters of the model and that thermodynamical averages can be taken approximately with the respect to the $\hat{\rho}_0\left(\boldsymbol{D}_{\mathrm{opt}}\right)$. However, if it is possible to treat the problem perturbatively, the formalism presented should be correct in finding the optimal transformation which enables a perturbative approach.

5.4.3 Equations for Variational Parameters

This section deals with the procedure of solving the system of equations for the variational parameters set up by minimizing the right-hand side of (5.37). One considers cuboid superlattice in the nearest neighbor approximation. By putting the transformed Hamiltonian (5.23) into inequality (5.37) and exploiting the fact that $\mathrm{Tr}\left(\hat{\rho}_0\left(\boldsymbol{D}\right)\hat{V}\left(\boldsymbol{D}\right)\right)=0$, one gets the inequality for relevant fermionic factor of free energy:

$$F \leq -k_B T \ln \sum_{\boldsymbol{k}} \left(\mathrm{e}^{-\beta \bar{E}_{\boldsymbol{k}}(\boldsymbol{D})}\right). \tag{5.38}$$

The reason why only the electron factor of free energy is observed is that variational parameters only appear in transformed electron energy bands. By puting the expression (5.24) into the (5.38) one gets

$$F \leq E_0 + E'\left(\boldsymbol{D}\right) - \tag{5.39}$$
$$- k_B T \ln \left(\frac{V}{8\pi^3}\int_{FBZ}\mathrm{d}^3\boldsymbol{k}\,\mathrm{e}^{-\beta\sum_{\boldsymbol{R}+}J_{\boldsymbol{R}}(\boldsymbol{D})\cos\left(\boldsymbol{k}\cdot\boldsymbol{R}\right)}\right).$$

In the case of cubic superlattice, the first Brillouin zone extends between $-\frac{\pi}{C_x}<k_x<\frac{\pi}{C_x}$, $-\frac{\pi}{C_y}<k_y<\frac{\pi}{C_y}$ and $-\frac{\pi}{C_z}<k_z<\frac{\pi}{C_z}$. Summation over positive lattice vectors in (5.39) can be approximated with the three nearest neighbor terms in all three Cartesian directions. Taking into the account the

integral representation of modified Bessel function $I_0\left(z\right) = \frac{1}{\pi}\int_0^\pi \mathrm{e}^{\pm z\cos\theta}\mathrm{d}\theta$ one gets

$$F \leq E_0 + E' - \tag{5.40}$$

$$- k_B T \ln\left(N I_0\left(\beta J_{\boldsymbol{C}_x}\right) I_0\left(\beta J_{\boldsymbol{C}_y}\right) I_0\left(\beta J_{\boldsymbol{C}_z}\right)\right).$$

One further declares $E_0 = 0$ and omits the $\ln N$ term which finally gives the function to be minimized:

$$F_u\left(\boldsymbol{D}\right) = E' - k_B T \ln\left(I_0\left(\beta J_{\boldsymbol{C}_x}\right) I_0\left(\beta J_{\boldsymbol{C}_y}\right) I_0\left(\beta J_{\boldsymbol{C}_z}\right)\right). \tag{5.41}$$

Setting the extrema condition for each variational parameter and taking into account that for cubic lattice $J_e = J_{\boldsymbol{C}_x} = J_{\boldsymbol{C}_y} = J_{\boldsymbol{C}_z}$, one obtains the system of equations:

$$\frac{\partial F_u}{\partial D_{\boldsymbol{R},f}} = 0 = 2D_{\boldsymbol{R},f}\hbar\Omega_f - 2G_f\delta_{0,\boldsymbol{R}} + \tag{5.42}$$

$$+ J_e \frac{I_1\left(\beta J_e\right)}{I_0\left(\beta J_e\right)} \coth\frac{\beta\hbar\Omega_f}{2}(6D_{\boldsymbol{R},f} - D_{\boldsymbol{R}-\boldsymbol{C}_x,f} - D_{\boldsymbol{R}+\boldsymbol{C}_x,f} -$$

$$- D_{\boldsymbol{R}-\boldsymbol{C}_y,f} - D_{\boldsymbol{R}+\boldsymbol{C}_y,f} - D_{\boldsymbol{R}+\boldsymbol{C}_z,f} - D_{\boldsymbol{R}+\boldsymbol{C}_z,f}).$$

By solving this system of equations, one obtains the optimal parameters $\boldsymbol{D}_{opt}$ which further define the optimal unitary transformation of presented model. Having found the optimal transformation, further examination of the system is now possible.

5.4.4 Polarons in CQD Supercrystals

The coefficients $D_{\boldsymbol{S},f}$ quantify the degree of dressing of an electron at site $\boldsymbol{R}$ by phonon of mode f at site $\boldsymbol{R}+\boldsymbol{S}$. In the case of strong electron–phonon

interaction, the electrons are dressed by phonons from the same site and these coefficients take the form $D_{\boldsymbol{S},f} = \delta_{\boldsymbol{S},0}\frac{G_f}{\hbar\Omega_f}$. On the other hand, for a weak electron–phonon interaction, these coefficients have smaller values but their range is much longer and phonons from many different sites participate in dressing the electron. Therefore, one can in principle establish that the charge carrier is a small polaron if the dependence of $D_{\boldsymbol{S},f}$ on $\boldsymbol{S}$ is strongly peaked at $\boldsymbol{S} = 0$.

It is however more convenient to have a single number which describes whether the carriers are small polarons or not. The electron–phonon interaction also leads to renormalization of the band dispersion from the $E_{\mathbf{k}} = \sum_{\mathbf{R}} J_{\mathbf{R}}\mathrm{e}^{i\mathbf{k}\cdot\mathbf{R}}$ to the $E_{\mathbf{k}}(\mathbf{D}) = \sum_{\mathbf{R}} J_{\mathbf{R}}(\mathbf{D})\,\mathrm{e}^{i\mathbf{k}\cdot\mathbf{R}} + E'(\mathbf{D})$ dependence, where

$$J_{\boldsymbol{R}}(\boldsymbol{D}) = J_{\boldsymbol{R}}\mathrm{e}^{-\frac{1}{2}\sum_{\boldsymbol{R}',f}\left(D_{\boldsymbol{R}'}-D_{\boldsymbol{R}'-\boldsymbol{R}}\right)^2\coth\left(\frac{\beta\hbar\Omega_f}{2}\right)}, \tag{5.43}$$

with $\beta = 1/(k_{\mathrm{B}}T)$, where T is the temperature. Term $E'(\boldsymbol{D})$ does not depend on the wavevector $\boldsymbol{k}$ and can be further omitted from discussion. Therefore, the electron–phonon interaction leads to the reduction of the bandwidth by a factor of $\kappa = J_{\boldsymbol{R}}(\boldsymbol{D})/J_{\mathbf{R}}$ (In the case of nearest neighbor approximation κ is unambiguously defined). If the carriers are small polarons, then the condition $\kappa \ll 1$ is satisfied[160]. In Fig. 5.2 values of variational parameters averaged over all phonon modes in terms of integer lattice site and for several values of parameter κ are presented. For maximal value of $\kappa \approx 1$, variational parameters exhibit significant values for relatively far sites. With decreasing κ, the central coefficient becomes larger, but the coefficients far from central site decrease. Eventually, for $\kappa \approx 0$, parameters are strongly peaked at $\boldsymbol{S} = 0$ and formation of small polaron takes place. Consequently, one introduces the criterion $\kappa < 0.05$ which can be used as a threshold beyond which the small polaron formation takes place as indicated

in Fig. 5.2.
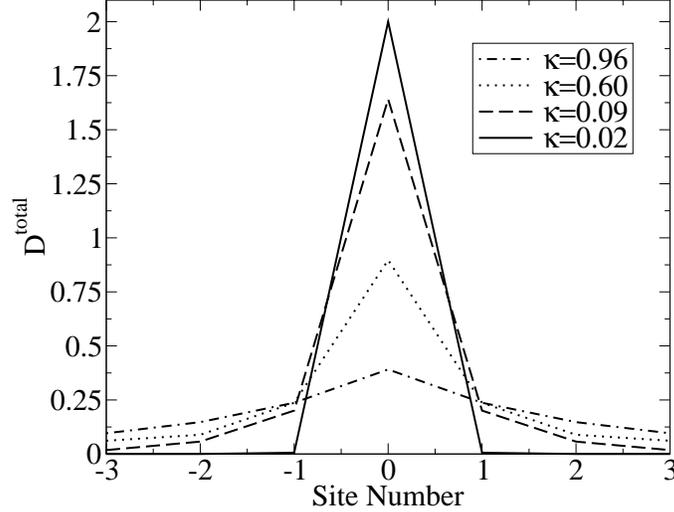
Figure 5.2: $D_{\boldsymbol{R}}^{\text{total}} = \sqrt{\sum_f D_{\boldsymbol{R},f}^2}$ for 1D lattice model for the several values of parameter κ. Phonon spectrum is taken from Tabs. 3.1 and 3.2. The value of $\kappa=0.96$ corresponds to the $J=$-40 meV and $T=$4 K, $\kappa=0.60$ corresponds to the $J=$-20 meV and $T=$83 K, $\kappa=0.02$ corresponds to the $J=$-2.5 meV and $T=$4 K and $\kappa=0.09$ corresponds to the $J=$-7 meV and $T=$4 K.

In Fig. 5.3 one presents for the several different values of dot radius the region of (J,T) parameters for which the condition $\kappa < 0.05$ is satisfied. Negative values for transfer integrals J are adopted so the corresponding Bloch energies have the minimum for $\boldsymbol{k} = 0$ according to Eq. (5.24). These results unambiguously demonstrate that at room temperature the charge carriers in NSs are small polarons for all realistic values of electronic coupling and dot dimensions. As seen from Fig. 5.3, electronic coupling of at least 15-30 meV would be required to break the small polaron at room temperature, a value much larger then theoretical [155] and experimental [7, 156] estimates of electronic coupling both less then 10 meV.
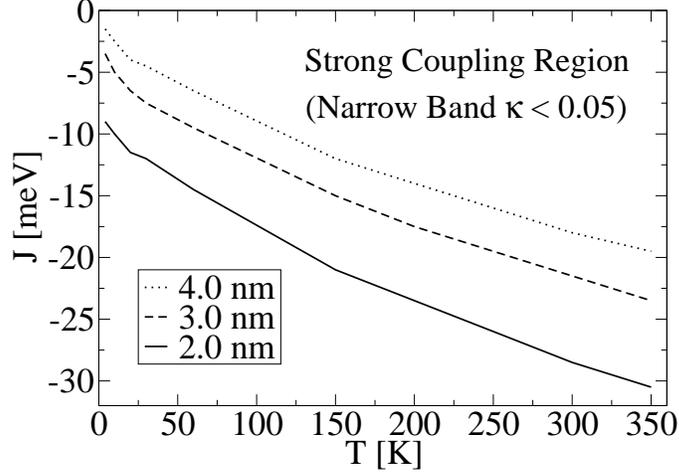
Figure 5.3: J vs T diagram demonstrating the areas of strong and weak coupling regimes. The limiting curve has been chosen so the parameter $\kappa = \mathrm{e}^{-\frac{1}{2}\sum_{\boldsymbol{R'},f}\left(\boldsymbol{D}_{\boldsymbol{R'}}-\boldsymbol{D}_{\boldsymbol{R'}-\boldsymbol{C}_x}\right)^2 \coth \frac{\beta\hbar\Omega_f}{2}} < 0.05$. Strong coupling regime occurs in the upper right region for increasing temperature and electronic coupling.

5.5   Mobility of Polarons in CQD Supercrystals

In this section, the expression for mobility (5.13) will be used together with variational polaron theory in order to obtain mobilities of polarons in CQD supercrystals. One is interested only in mobility of carrier in the same direction as the direction of applied electric field, i.e. subscript pair ν, μ of the mobility in Eq. (5.13) changes for example to x, x. Unitary transformation does not change thermodynamic average in the equation for mobility (5.13) and transformed version of it reads as

$$\mu_{xx} = \frac{1}{2e_0 N_c}\beta \int_{-\infty}^{\infty} \times \tag{5.44}$$
$$\times \mathrm{Tr}\left(\hat{\rho}\left(\boldsymbol{D}\right)\mathrm{e}^{i\frac{\hat{H}(\boldsymbol{D})}{\hbar}t}\hat{J}_x\left(\boldsymbol{D}\right)\mathrm{e}^{-i\frac{\hat{H}(\boldsymbol{D})}{\hbar}t}\hat{J}_x\left(\boldsymbol{D}\right)\right)dt$$

The current operator in transformed coordinates and in superlattice basis reads:

$$\hat{J}_x\left(\boldsymbol{D}\right) = \sum_{\boldsymbol{R},\boldsymbol{S}} \sum_{\boldsymbol{k},\boldsymbol{q}} J^{\boldsymbol{R},\boldsymbol{S}}_{\boldsymbol{k},\boldsymbol{q},x} \hat{A}^\dagger_{\boldsymbol{k}} \hat{A}_{\boldsymbol{q}} \hat{\Theta}^\dagger_{\boldsymbol{R}}\left(\boldsymbol{D}\right) \hat{\Theta}_{\boldsymbol{S}}\left(\boldsymbol{D}\right) \tag{5.45}$$

where

$$J^{\boldsymbol{R},\boldsymbol{S}}_{\boldsymbol{k},\boldsymbol{q},x} = \frac{e_0}{iN\hbar}\left(R_x - S_x\right) E_{\boldsymbol{R}-\boldsymbol{S}} \mathrm{e}^{i(\boldsymbol{k}\cdot\boldsymbol{R}-\boldsymbol{q}\cdot\boldsymbol{S})} \tag{5.46}$$

One further switches to the interaction picture with the respect to the operator $\hat{H}_0\left(\boldsymbol{D}\right)$. This will be denoted with index I, e.g. $\hat{A}_{\boldsymbol{q},I}\left(t\right) = \mathrm{e}^{i\frac{\hat{H}_0(\boldsymbol{D})}{\hbar}t}\hat{A}_{\boldsymbol{q}}\mathrm{e}^{-i\frac{\hat{H}_0(\boldsymbol{D})}{\hbar}t}$ This still leaves the S-matrix in a product under trace for the current operator:

$$\hat{S}\left(\boldsymbol{D},t\right) = \mathrm{e}^{i\frac{\hat{H}_0(\boldsymbol{D})}{\hbar}t}\mathrm{e}^{-i\frac{\hat{H}(\boldsymbol{D})}{\hbar}t} \tag{5.47}$$

The S-matrix obeys dynamical equation:

$$i\hbar\frac{\mathrm{d}\hat{S}\left(\boldsymbol{D},t\right)}{\mathrm{d}t} = \hat{V}_I\left(t'\right)\hat{S}\left(\boldsymbol{D},t\right) \tag{5.48}$$

which expansion in Dyson series gives

$$\hat{S}\left(\boldsymbol{D},t\right) = \hat{I} + \sum_{n=1}^{\infty}\frac{\left(-\frac{i}{\hbar}\right)^n}{n!}\int_0^t\ldots\int_0^t\times \tag{5.49}$$
$$T\left[\hat{V}_I\left(t_1\right)\ldots\hat{V}_I\left(t_n\right)\right]dt_1\ldots dt_n$$

Putting the expression for the current operator into Eq. (5.44), and expanding the S-operator one gets:

$$\mu_{xy} = \mu^{(0)}_{xy} + \mu^{(1)}_{xy} + \ldots \tag{5.50}$$

where

$$\mu_{xy}^{(0)} = \frac{\beta}{2e_0 N_c} \sum_{\boldsymbol{R},\boldsymbol{S}} \sum_{\boldsymbol{k},\boldsymbol{q}} \sum_{\boldsymbol{R'},\boldsymbol{S'}} \sum_{\boldsymbol{k'},\boldsymbol{q'}} \left(J_{\boldsymbol{k},\boldsymbol{q},x}^{\boldsymbol{R},\boldsymbol{S}} J_{\boldsymbol{k'},\boldsymbol{q'},y}^{\boldsymbol{R'},\boldsymbol{S'}} \int_{-\infty}^{\infty} dt \times \right. \tag{5.51}$$

$$\times \mathrm{Tr}\Big(\hat{\rho}(\boldsymbol{D}) \, \hat{A}_{\boldsymbol{k}I}^{\dagger}(t) \, \hat{A}_{\boldsymbol{q}I}(t) \, \hat{\Theta}_{\boldsymbol{R}I}^{\dagger}(\boldsymbol{D},t) \, \hat{\Theta}_{\boldsymbol{S}I}(\boldsymbol{D},t) \times$$

$$\left. \times \hat{A}_{\boldsymbol{k'}}^{\dagger} \hat{A}_{\boldsymbol{q'}} \hat{\Theta}_{\boldsymbol{R'}}^{\dagger}(\boldsymbol{D}) \, \hat{\Theta}_{\boldsymbol{S'}}(\boldsymbol{D}) \Big) \right)$$

$$\mu_{xy}^{(1)} = \frac{-i\beta}{2\hbar e_0 N_c} \sum_{\boldsymbol{R},\boldsymbol{S}} \sum_{\boldsymbol{k},\boldsymbol{q}} \sum_{\boldsymbol{R'},\boldsymbol{S'}} \sum_{\boldsymbol{k'},\boldsymbol{q'}} \left(J_{\boldsymbol{k},\boldsymbol{q},x}^{\boldsymbol{R},\boldsymbol{S}} J_{\boldsymbol{k'},\boldsymbol{q'},y}^{\boldsymbol{R'},\boldsymbol{S'}} \int_{-\infty}^{\infty} dt \int_{0}^{t} dt' \times \right. \tag{5.52}$$

$$\times \mathrm{Tr}\Big(\hat{\rho}(\boldsymbol{D}) \left[\hat{V}_I(t'), \hat{A}_{\boldsymbol{k}I}^{\dagger}(t) \, \hat{A}_{\boldsymbol{q}I}(t) \, \hat{\Theta}_{\boldsymbol{R}I}^{\dagger}(\boldsymbol{D},t) \, \hat{\Theta}_{\boldsymbol{S}I}(\boldsymbol{D},t) \right] \times$$

$$\left. \times \hat{A}_{\boldsymbol{k'}}^{\dagger} \hat{A}_{\boldsymbol{q'}} \hat{\Theta}_{\boldsymbol{R'}}^{\dagger}(\boldsymbol{D}) \, \hat{\Theta}_{\boldsymbol{S'}}(\boldsymbol{D}) \Big) \right)$$

$$\vdots$$

So far, the only two approximations in this model come from linear response theory represented by Kubo formula and the model itself. These cumbersome expressions for zeroth and first order mobility can be significantly simplified analytically if certain additional approximations are introduced. Before introducing these approximations one can analytically write explicit evolutions of the operators of interest since the evolution of those operators in the interaction picture is given by the disentangled zeroth order Hamiltonian:

$$\hat{A}_{\boldsymbol{k}I}^{\dagger}(t) = \hat{A}_{\boldsymbol{k}}^{\dagger} \mathrm{e}^{i\frac{\bar{E}_{\boldsymbol{k}}(\boldsymbol{D})}{\hbar}t} \tag{5.53}$$

$$\hat{A}_{\boldsymbol{k}I}(t) = \hat{A}_{\boldsymbol{k}} \mathrm{e}^{-i\frac{\bar{E}_{\boldsymbol{k}}(\boldsymbol{D})}{\hbar}t}$$

$$\hat{\Theta}_{\boldsymbol{R}I}^{\dagger}(\boldsymbol{D},t) = \mathrm{e}^{-\sum_{\boldsymbol{S},f} D_{\boldsymbol{S}-\boldsymbol{R},f}\left(\hat{B}_{\boldsymbol{S},f} \mathrm{e}^{-i\Omega_f t} - \hat{B}_{\boldsymbol{S},f}^{\dagger} \mathrm{e}^{i\Omega_f t} \right)}$$

$$\hat{\Theta}_{\boldsymbol{R}I}(\boldsymbol{D},t) = \mathrm{e}^{\sum_{\boldsymbol{S},f} D_{\boldsymbol{S}-\boldsymbol{R},f}\left(\hat{B}_{\boldsymbol{S},f} \mathrm{e}^{-i\Omega_f t} - \hat{B}_{\boldsymbol{S},f}^{\dagger} \mathrm{e}^{i\Omega_f t} \right)}$$

These analytical expressions will be used together with few approximations

to simplify the expressions for mobility.

5.5.1   Zeroth Order for Mobility

The first required approximation is truncation of expansion in Eq. (5.50). In this chapter the expression for the zeroth order mobility will be derived. Truncation will be performed later on according to estimated values of higher orders of mobility and their importance. Thermodynamical averaging in Eqs. (5.51) is defined with respect to the full transformed Hamiltonian (5.22). The great advantage of variational polaron theory is that disentangled statistical operator is introduced as an approximate solution and optimization is performed after. Argumented with this, it is possible to introduce the following approximation:

$$\mathrm{Tr}\left(\hat{\rho}\left(\boldsymbol{D}\right)\cdots\right) \approx \mathrm{Tr}\left(\hat{\rho}_0\left(\boldsymbol{D}\right)\cdots\right) = \langle\cdots\rangle_0,$$

where shorthand notation for averaging according to approximated disentangled statistical operator is introduced.

Since the statistical operator is disentangled, averaging of the product of fermionic and bosonic operators equals the product of averaged fermionic and bosonic operators separately. Averaging of fermionic operators is performed by using the Wick's theorem [122]:

$$\langle\hat{A}^{\dagger}_{\boldsymbol{k}I}\left(t\right)\hat{A}_{\boldsymbol{q}I}\left(t\right)\hat{A}^{\dagger}_{\boldsymbol{k'}}\hat{A}_{\boldsymbol{q'}}\rangle_0 = \mathrm{e}^{i\frac{\bar{E}_{\boldsymbol{k}}(\boldsymbol{D})-\bar{E}_{\boldsymbol{q}}(\boldsymbol{D})}{\hbar}t}\times \qquad (5.54)$$

$$\times\left(\delta_{\boldsymbol{k},\boldsymbol{q}}\delta_{\boldsymbol{k'},\boldsymbol{q'}}n_{\boldsymbol{k}}n_{\boldsymbol{k'}} + \delta_{\boldsymbol{k},\boldsymbol{q'}}\delta_{\boldsymbol{k'},\boldsymbol{q}}n_{\boldsymbol{k}}\left(1-n_{\boldsymbol{k'}}\right)\right).$$

Averaging of bosonic operators is performed by using the Feynman disen-

tangling theorem as described in Ref. 122:

$$\langle\hat{\Theta}^{\dagger}_{\boldsymbol{R}I}\left(\boldsymbol{D},t\right)\hat{\Theta}_{\boldsymbol{S}I}\left(\boldsymbol{D},t\right)\hat{\Theta}^{\dagger}_{\boldsymbol{R}'}\left(\boldsymbol{D}\right)\hat{\Theta}_{\boldsymbol{S}'}\left(\boldsymbol{D}\right)\rangle_0 = \tag{5.55}$$

$$= \Theta^0_{\boldsymbol{R}-\boldsymbol{S},\boldsymbol{R}'-\boldsymbol{S}'}\left(\boldsymbol{D}\right)\Theta_{\boldsymbol{R}-\boldsymbol{S},\boldsymbol{R}'-\boldsymbol{S}',\boldsymbol{R}-\boldsymbol{R}'}\left(\boldsymbol{D},t\right),$$

where (with new indices $\boldsymbol{R}-\boldsymbol{S}=\boldsymbol{X}$, $\boldsymbol{R}'-\boldsymbol{S}'=\boldsymbol{Y}$, $\boldsymbol{R}-\boldsymbol{R}'=\boldsymbol{Z}$) :

$$\Theta^0_{\boldsymbol{X},\boldsymbol{Y}}\left(\boldsymbol{D}\right) = \exp\Bigg[-\sum_f\left(N_f+\frac{1}{2}\right)\times \tag{5.56}$$

$$\times\sum_{\boldsymbol{U}}\left((D_{\boldsymbol{U},f}-D_{\boldsymbol{U}+\boldsymbol{X},f})^2+(D_{\boldsymbol{U},f}-D_{\boldsymbol{U}+\boldsymbol{Y},f})^2\right)\Bigg],$$

$$\Theta_{\boldsymbol{X},\boldsymbol{Y},\boldsymbol{Z}}\left(\boldsymbol{D},t\right) = \exp\Bigg[-\sum_f\left((N_f+1)\,\mathrm{e}^{-i\Omega_f t}+N_f\mathrm{e}^{i\Omega_f t}\right)\times$$

$$\times\sum_{\boldsymbol{U}}(D_{\boldsymbol{U},f}-D_{\boldsymbol{U}+\boldsymbol{X},f})(D_{\boldsymbol{U}+\boldsymbol{Z},f}-D_{\boldsymbol{U}+\boldsymbol{Z}+\boldsymbol{Y},f})\Bigg].$$

After performed averaging, one applies the low-carrier concentration approximation, i.e. one takes only terms linear in carrier concentrations from Eq. (5.54). By putting that together with Eq. (5.55) back to Eq. (5.51) and retaining new dummy variables $\boldsymbol{X}$, $\boldsymbol{Y}$ and $\boldsymbol{Z}$ one obtains the expression for zeroth order mobility:

$$\mu^{(0)}_{xx} = \frac{-\beta e_0}{2\hbar^2 N_c N}\sum_{\boldsymbol{R},\boldsymbol{X},\boldsymbol{Y}}\sum_{\boldsymbol{k},\boldsymbol{q}}\Bigg(E_{\boldsymbol{X}}E_{\boldsymbol{Y}}X_x Y_x\times \tag{5.57}$$

$$\times\,\mathrm{e}^{-i(\boldsymbol{k}\cdot\boldsymbol{Y}+\boldsymbol{q}\cdot\boldsymbol{X})}n_{\boldsymbol{k}}\left(1-n_{\boldsymbol{q}}\right)\int_{-\infty}^{\infty}dt\mathrm{e}^{i\frac{\bar{E}_{\boldsymbol{k}}(\boldsymbol{D})-\bar{E}_{\boldsymbol{q}}(\boldsymbol{D})}{\hbar}t}\times$$

$$\frac{1}{N}\sum_{\boldsymbol{Z}}\mathrm{e}^{i(\boldsymbol{k}-\boldsymbol{q})\cdot\boldsymbol{Z}}\Theta^0_{\boldsymbol{X},\boldsymbol{Y}}\left(\boldsymbol{D}\right)\Theta_{\boldsymbol{X},\boldsymbol{Y},\boldsymbol{Z}}\left(\boldsymbol{D},t\right)\Bigg).$$

It is important to remark that only the nearest neighbor $E_{\boldsymbol{X}}$ and $E_{\boldsymbol{Y}}$ are relevant, thus the summation over $\boldsymbol{X}$ and $\boldsymbol{Y}$ is finite. In order to divide contributions to mobility coming from phonon assisted hopping and band-

like structure, the following splitting is introduced:

$$\Theta^0_{\boldsymbol{X},\boldsymbol{Y}}(\boldsymbol{D})\,\Theta_{\boldsymbol{X},\boldsymbol{Y},\boldsymbol{Z}}(\boldsymbol{D},t) = \Theta^0_{\boldsymbol{X},\boldsymbol{Y}}(\boldsymbol{D}) + \tag{5.58}$$

$$\Theta^0_{\boldsymbol{X},\boldsymbol{Y}}(\boldsymbol{D})\,(\Theta_{\boldsymbol{X},\boldsymbol{Y},\boldsymbol{Z}}(\boldsymbol{D},t) - 1)$$

Due to low concentration carrier approximation one can write:

$$n_{\boldsymbol{k}}\,(1 - n_{\boldsymbol{q}}) \approx n_{\boldsymbol{k}} \approx e^{-\beta(E_{\boldsymbol{k}} - E_f)}, \tag{5.59}$$

and thus

$$N_c = \sum_{\boldsymbol{k}} n_{\boldsymbol{k}} = \frac{V}{8\pi^3}\int d^3\boldsymbol{k}\,e^{-\beta(E_{\boldsymbol{k}} - E_f)}. \tag{5.60}$$

The term $\Theta^0_{\boldsymbol{X},\boldsymbol{Y}}(\boldsymbol{D})$ gives rise to the coherent mobility. After exploiting the relation $\sum_{\boldsymbol{Z}} e^{-i(\boldsymbol{k}-\boldsymbol{q})\cdot\boldsymbol{Z}} = N\delta_{\boldsymbol{k},\boldsymbol{q}}$, the expression for the coherent part of mobility reads:

$$\mu^{\mathrm{coh},(0)}_{xx} = \frac{1}{N_c}\sum_{\boldsymbol{k}} n_{\boldsymbol{k}}\mu'_{\boldsymbol{k}}(\boldsymbol{D}) \approx \tag{5.61}$$

$$\approx \frac{\int d^3\boldsymbol{k}\,e^{-\beta E_{\boldsymbol{k}}}\mu'_{\boldsymbol{k}}(\boldsymbol{D})}{\int d^3\boldsymbol{k}\,e^{-\beta E_{\boldsymbol{k}}}},$$

where

$$\mu'_{\boldsymbol{k}}(\boldsymbol{D}) = \frac{-\beta e_0}{2\hbar^2}\int_{-\infty}^{\infty} e^{-\frac{t^2}{\tau_e^2}}\,dt\times \tag{5.62}$$

$$\times \sum_{\boldsymbol{X},\boldsymbol{Y}} X_x Y_x E_{\boldsymbol{X}} E_{\boldsymbol{Y}} e^{-i\boldsymbol{k}(\boldsymbol{X}+\boldsymbol{Y})}, \Theta^0_{\boldsymbol{X},\boldsymbol{Y}}(\boldsymbol{D})$$

and τ_e is phenomenologically introduced finite carrier lifetime due to crystal disorder, defects and impurities. Exploiting the nearest-neighbor approxi-

mation with spatially isotropic transfer integral

$$E_{\boldsymbol{U}} = E_1 \left(\delta_{\boldsymbol{U},\boldsymbol{C}_x} + \delta_{\boldsymbol{U},\boldsymbol{C}_y} + \delta_{\boldsymbol{U},\boldsymbol{C}_z} \right), \tag{5.63}$$

one obtains

$$\mu'_{\boldsymbol{k}} \left(\boldsymbol{D} \right) = -\frac{2\beta e_0}{2\hbar^2} \tau_e \sqrt{\pi} C_x^2 E_1^2 \times \tag{5.64}$$
$$\times \left(\cos \left(2k_x C_x \right) \Theta^0_{\boldsymbol{C}_x,\boldsymbol{C}_x} \left(\boldsymbol{D} \right) - \Theta^0_{-\boldsymbol{C}_x,\boldsymbol{C}_x} \left(\boldsymbol{D} \right) \right).$$

Without the phenomenological carrier damping, the time integral gives infinite mobility (regardless of phonon coherence) as was expected for coherent part. We will see that incoherent part gives also infinite mobility due to the time integral, but only in the case of perfectly coherent phonons. Infinity of the incoherent part is of lower level then the infinity of coherent part. Also, if one introduces the phonon damping(e.g. due to anharmonicity) the incoherent part of the mobility becomes finite, while coherent part remains infinite. Of course, both coherent and incoherent part become finite if one introduces damping for crystal Bloch states (e.g. due to crystal disorder, defects or impurities).

The term $\Theta^0_{\boldsymbol{X},\boldsymbol{Y}} \left(\boldsymbol{D} \right) \left(\Theta_{\boldsymbol{X},\boldsymbol{Y},\boldsymbol{Z}} \left(\boldsymbol{D}, t \right) - 1 \right)$ gives rise to the incoherent part of mobility. This term is periodic in time, takes values up to 1, never goes under the negative value of its positive maximum(this means that certainly it doesn't go under -1, but in practice it takes values slightly under zero) and it is significantly-valued only for near neighbor $\boldsymbol{Z}$-sites(it has been already argued that only near-neighbor $\boldsymbol{X}$ and $\boldsymbol{Y}$ are relevant). For far-neighbor $\boldsymbol{Z}$-sites this function oscillates around zero with very low amplitude (regardless of coupling strength) and can be neglected in the summation over $\boldsymbol{Z}$. Therefore, summation over $\boldsymbol{Z}$-sites will be finite in all regimes. However,

there is significant difference on the behavior of this function for various types of the regimes(for near-neighbor $\boldsymbol{Z}$-sites). In strong coupling regime this functions is predominantly close to zero at all times, except for certain points in time where it is narrowly peaked to the value of 1 or some negative value greater than -1. These narrow peaks appear periodically. In weak coupling regime this function is plane-wave like, oscillating around the zero. The time integral gives rise to the Fourier transform of this function:

$$\Xi_{\boldsymbol{X},\boldsymbol{Y},\boldsymbol{Z}}\left(\boldsymbol{D},\omega_{\boldsymbol{k},\boldsymbol{q}}\right) = \tag{5.65}$$
$$\int_{-\infty}^{\infty} dt e^{i\frac{\bar{E}_{\boldsymbol{k}}(\boldsymbol{D})-\bar{E}_{\boldsymbol{q}}(\boldsymbol{D})}{\hbar}t}\Theta_{\boldsymbol{X},\boldsymbol{Y}}^{0}\left(\boldsymbol{D}\right)\left(\Theta_{\boldsymbol{X},\boldsymbol{Y},\boldsymbol{Z}}\left(\boldsymbol{D},t\right)-1\right).$$

If we do not introduce any phenomenological damping to the phonon modes, then periodicity is not destroyed and Fourier transforms of these functions will be consisted of delta functions. Incoherent part of the mobility finally takes the form:

$$\mu_{xx}^{\text{inc},(0)} = \frac{1}{N_c N}\sum_{\boldsymbol{k},\boldsymbol{q}} n_{\boldsymbol{k}}\left(1-n_{\boldsymbol{q}}\right)\mu_{\boldsymbol{k},\boldsymbol{q}}'' \approx \tag{5.66}$$
$$\approx \frac{V_{\text{cell}}}{8\pi^3}\frac{\int \mathrm{d}^3\boldsymbol{k} e^{-\beta E_{\boldsymbol{k}}}\int \mathrm{d}^3\boldsymbol{q}\mu_{\boldsymbol{k},\boldsymbol{q}}''}{\int \mathrm{d}^3\boldsymbol{k} e^{-\beta E_{\boldsymbol{k}}}},$$

where

$$\mu_{\boldsymbol{k},\boldsymbol{q}}'' = \frac{-\beta e_0}{2\hbar^2}\sum_{\boldsymbol{X},\boldsymbol{Y}}\left(E_{\boldsymbol{X}}E_{\boldsymbol{Y}}X_x Y_x e^{-i(\boldsymbol{k}\cdot\boldsymbol{Y}+\boldsymbol{q}\cdot\boldsymbol{X})}\times \tag{5.67}\right.$$
$$\left.\sum_{\boldsymbol{Z}} e^{-i(\boldsymbol{k}-\boldsymbol{q})\cdot\boldsymbol{Z}}\Xi_{\boldsymbol{X},\boldsymbol{Y},\boldsymbol{Z}}\left(\boldsymbol{D},\omega_{\boldsymbol{k},\boldsymbol{q}}\right)\right).$$

5.5.2 Strong Coupling Limit and Generalized Marcus Formula

Charge transport due to the hopping mechanism, together with the localized electron–phonon interaction has already been studied in the literature(see Refs. 162, 163). The calculation of mobility in such cases was studied within the framework of Marcus theory. The mobility is given by Einstein's relation $\mu = \beta D e$, where D is the diffusion constant. The diffusion constant can be expressed in terms of the small polaron hopping rate W between two neighboring dots as $D = W C^2$ (C is distance two neighboring sites). Within the Marcus theory, small polaron hopping rate is given as

$$W = \frac{J^2}{\hbar} \sqrt{\frac{\beta \pi}{\lambda}} \mathrm{e}^{-\beta \lambda / 4}, \tag{5.68}$$

where $\lambda = 2 \sum_f \frac{G_f^2}{\hbar \Omega_f}$ is the reorganization energy. Marcus theory is valid only in the high-temperature limit $\beta \hbar \Omega_f \ll 1$. There is also generalization of the Marcus theory which goes beyond the limit $\beta \hbar \Omega_f \ll 1$. The so called generalized Marcus formula was used in Refs. 162, 163 and it reads

$$W = \frac{J^2}{\hbar^2} \int_{-\infty}^{\infty} \mathrm{d}t \exp \left\{ -2 \sum_f \frac{G_f^2}{\left(\hbar \Omega_f\right)^2} \times \right.$$
$$\left. \times \left[(2N_f + 1) - (N_f + 1)\, \mathrm{e}^{-i\Omega_f t} - N_f \mathrm{e}^{i\Omega_f t} \right] \right\}. \tag{5.69}$$

In the high-temperature limit $\beta \hbar \Omega_f \ll 1$ generalized Marcus formula reduces to well known Marcus formula.

For electron–phonon coupling strengths given in Tabs. 3.1 and 3.2 the high-temperature limit condition is not satisfied and therefore one should use Eq. (5.72) instead of the simpler Eq. (5.68). Eq. (5.72) can alternatively be obtained by applying presented Kubo's linear response theory to

transformed Hamiltonian and taking the limit of strong electron–phonon coupling. Therefore, this is a full quantum mechanical formula for charge carrier mobility. The rest of this subsection will be dedicated to derivation of equivalence of the presented theory in the strong coupling limit and generalized Marcus formula (5.69).

In strong coupling limit one assumes the situation where $D_{\boldsymbol{S},f} = \delta_{\boldsymbol{S},0}\frac{G_f}{\hbar\Omega_f}$. In such limit, following identities and approximation are valid:

$$\Theta^0_{\boldsymbol{X},\boldsymbol{Y}}(\boldsymbol{D}) = \mathrm{e}^{-2\sum_f (2N_f+1)\left(\frac{G_f}{\hbar\Omega_f}\right)^2}, \tag{5.70}$$

with the property that $\Theta^0_{\boldsymbol{X},\boldsymbol{Y}}(\boldsymbol{D}) \ll 1$, and

$$\Theta^0_{\boldsymbol{X},\boldsymbol{Y}}(\boldsymbol{D})\,\Theta_{\boldsymbol{X},\boldsymbol{Y},\boldsymbol{Z}}(\boldsymbol{D},t) \approx \mathrm{e}^{-2\sum_f \left(\frac{G_f}{\hbar\Omega_f}\right)^2 (2N_f+1)} \times \tag{5.71}$$

$$\times\,\mathrm{e}^{2\sum_f \left(\frac{G_f}{\hbar\Omega_f}\right)^2 \left((2N_f+1)\cos\left(\Omega_f t\right)+i\sin\left(\Omega_f t\right)\right)} \delta_{\boldsymbol{X},-\boldsymbol{Y}}\delta_{\boldsymbol{X},\boldsymbol{Z}}.$$

Additionally, band narrowing in strong coupling is extreme and thus $\mathrm{e}^{i\frac{\bar{E}_{\boldsymbol{k}}(\boldsymbol{D})-\bar{E}_{\boldsymbol{q}}(\boldsymbol{D})}{\hbar}t} \approx 1$. Taking into account equation (5.60) and $\sum_{\boldsymbol{q}} 1 = N$ expression for hopping mobility (5.66) in strong coupling regime becomes

$$\mu_{xx}^{\mathrm{inc},(0)} = \frac{-\beta e_0 E_1^2 C^2}{\hbar^2} \int_{-\infty}^{\infty} \mathrm{d}t\, \exp\left\{-2\sum_f \frac{G_f^2}{\left(\hbar\Omega_f\right)^2} \times \right.$$

$$\left. \times \left[(2N_f+1) - (N_f+1)\,\mathrm{e}^{-i\Omega_f t} - N_f \mathrm{e}^{i\Omega_f t}\right]\right\}. \tag{5.72}$$

which is the same as introduced generalized Marcus formula.

5.5.3   Small Polaron Mobility in CQD Supercrystals

It has been shown that CQD supercrystals are in the small polaron regime for the wide range of input temperature and transfer integrals. In such a regime, phenomenological damping parameters τ_e and τ_{ph} are of little importance since their values are smaller then the period of peak appearance in the integral function of time in Eq. (5.72)(this is what justifies the short time approximation introduced in Refs. 162, 163). It is now possible to calculate the charge carrier mobility when the system is in the small polaron regime. The calculated temperature dependence of the mobility for several dot sizes and electronic coupling parameters is presented in Fig. 5.4. In all of these cases the small polaron condition is satisfied, as can be seen from Fig. 5.3. It was found that in the range of temperatures around room temperature the mobility decreases with increasing temperature for all the investigated dot dimensions. Such a temperature dependence was, in several previous works[86, 6, 7], considered to be a signature of band transport. Here, it was demonstrated that this type of temperature dependence is present also in small polaron transport. Therefore, the "band-like" temperature dependence of the mobility cannot be considered as a proof of band transport. In fact, it has been shown that electron–phonon interaction in CdSe dots is sufficiently strong for the formation of small polarons whose mobility decreases with increasing temperature.

One can also examine how the strength of the electron–phonon coupling influences the mobility. By increasing the dot size, the strength of the electron–phonon coupling decreases(see Tabs. 3.1 and 3.2) and the mobility increases as presented in Fig. 5.4. This is an expected behavior for the small polaron regime because weaker electron–phonon coupling leads to a polaron that is less strongly bound and, therefore, it can hop to a neighboring dot
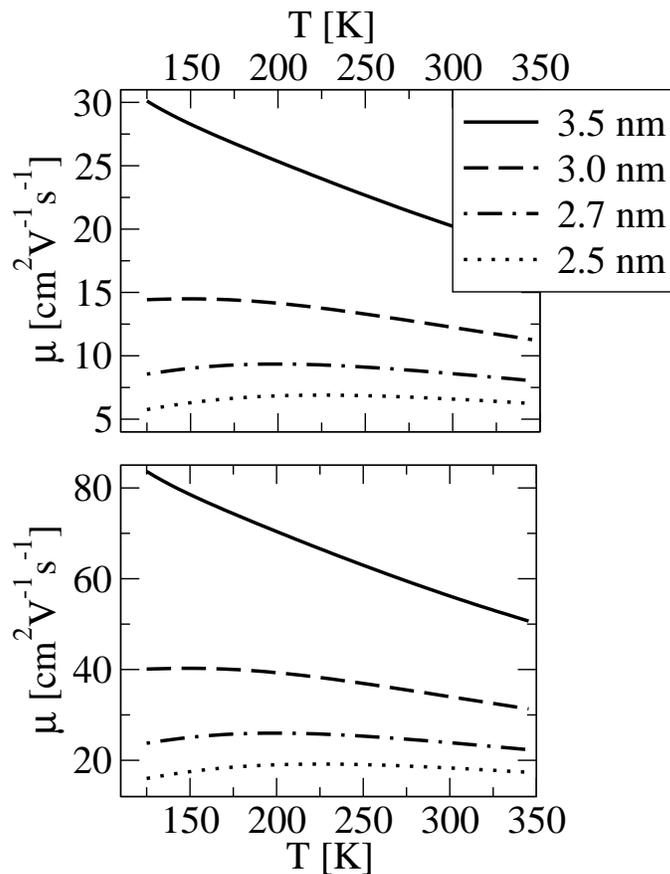
Figure 5.4: Mobility vs temperature plot for various dot sizes and two different values of electronic coupling between the dots (6 meV for upper and 10 meV for lower plot). These curves resemble those found in experiment [6, 7]

more easily. An increase of mobility with an increase in dot dimensions has been observed in several experiments [164, 156]. In the small polaron regime, the mobility has quadratic dependence on electronic coupling J, which is direct consequence of Eq. (5.72).

In Ref. 7 the mobilities of the order of $(20-30)\,\mathrm{cm}^2/\mathrm{Vs}$ were measured in the linear regime in field-effect transistors with CdSe NSs. These mobilities gradually increase, exhibit a peak and then gradually decrease with increasing the temperature. The similar behavior in the simulation presented for

dots whose radius is below 3.0 nm is obtained – the peak of mobility moves from 230 K for the dot with radius 2.5 nm to 140 K for the dot with radius of 3.0 nm. One should still note that the comparison of presented theoretical results with these experiments should be taken with caution due to the effects of disorder and traps which are present in experiment. Again, despite the relatively large values of mobility, for these parameters the electrical transport takes place by small polaron hopping.

In summary in this chapter, a model has been developed which describes the electronic transport at low carrier concentration in ideal NSs. Elastic and dielectric continuum models were used to obtain phonon spectra and the strength of their coupling to electrons. Variational polaron theory was then used to establish the nature of charge carriers. Hopping rates and carrier mobility were evaluated using the approach that fully takes into account the quantum mechanical nature of phonons and their interaction with electrons.

Conditions have been identified for the strong coupling regime where band narrowing is so strong that small polaron formation takes place. Based on this and the calculated mobilities one concludes that recently fabricated NSs do not exhibit band transport but instead reside in the strong electron–phonon coupling regime where localized carriers exhibit hopping transport. In such a transport regime, the mobility also decreases by increasing the temperature.

While the study in this chapter was focused on idealized CQD supercrystals without disorder or traps, the main conclusion that the presence of band transport is highly unlikely in CQD supercrystals can be extended to realistic structures, because it is well understood that disorder and traps act detrimentally on the possibility of band transport.

Chapter 6

Concluding Remarks and Future Works

The work presented in this thesis regards the intraband physics of quantum dot nanostructures with the strong accent on applications. Chap. 1 was devoted to justification of theoretical approach in intraband engineering. The key requirement for engineering is the ability to control geometrical and compositional parameters of semiconductor quantum dots. Therefore, state of the art technological advancement in the field of nanofabrications of 3D confining nanostructures such as quantum dot elongation or CQD supercrystals was presented in introduction section of the thesis. Possible applications were briefly summarized and great pragmatic importance of such engineering was elaborated.

The most important issue in the physics of all semiconductor nanostructures is the description of their intrinsic properties. The majority of experiments conducted on semiconductor nanostructures and consequent applications are based on the interaction of the free carriers of charge and external electromagnetic field. The external electromagnetic field needs to

165

considered within the two different types of experiments. The first type are spectroscopic experiments where external electromagnetic field in the form of radiation is being absorbed or emitted by the object of study and consequent quantum dynamical movement of carriers follows. The second type are transport experiments, where usually a low frequency electric field is applied upon samples inducing the transport of carriers. It is obvious that both type of experiments lead to appropriate optoelectronic applications as explained in Chap. 1.

Therefore, physics of carriers in nanostructures and their response to external electromagnetic field is of great importance to this scientific field. It is intuitively very clear that free electrons from conduction band in semiconductor bulk materials play central role in the formation of carriers in nanostructures. Hence, in order to start a description of carriers inside these nanostructures one has to answer the question "What happens to electrons from the conduction band when they find themselves inside the heterostructure?". Thus, electronic structure calculation methods which have been proven to be very reliable in description of semiconductor nanostructures were elaborated in Chap. 2. 8 band $\boldsymbol{k} \cdot \boldsymbol{p}$ model was firstly introduced accounting for influence of conduction and valence band on carriers. This is very important when it comes to the study of excitons, but in intraband physics it turns out that electrons are not that much influenced by valence bands. For example, electronic features of quantum rods obtained by 8 band $\boldsymbol{k} \cdot \boldsymbol{p}$ model does not differ that much from the same features obtained by one band effective mass method. Therefore, for the rest of the thesis, effective mass model is solely applied.

The analysis of bound states in the continuum in quantum rods is the main contribution in the second chapter. It was demonstrated that such

an exotic state may have applications in design of polarization independent terahertz detectors. Also, bound state in continuum coupled to surrounding continuum can be seen as experimental realization of Fano-Anderson model, one of the rare exactly solvable many body Hamiltonians [122]. The future work left on this issue should be exact examination of the proposed polarization independent terahertz detector. This should be done from the application point of view by calculating characterization properties of such device such as mobility of carriers, quantum efficiency, dark current, etc... However, some fundamental aspects of the condensed matter physics can be studied as well. For example, one can construct effective Fano-Anderson Hamiltonian [122]. Coupling between the BIC and the surrounding continuum states occurs via phonons and one should develop pure electron Hamiltonian with effective constants of coupling between electronic states due to phonons. Since Fano-Anderson Hamiltonian is exactly solvable, one can then exactly calculate physical properties of such system. By comparing the experimental values of these physical properties with theoretically obtained values one can then study the correctness of the effective coupling constants due to phonons. This is very important issue in the condensed matter physics since it enables treatment of the complex electron-phonon polaron system in a pure electron space via effective coupling constants.

Beside electrons, vibrations of lattice are also present in all condensed matter systems and they play crucial role in physics of QD structures. The theoretical treatment of vibrational properties of QDs was given in Chap. 3. Second quantization of vibrational modes gives rise to phonons. Electrons and phonons are thus crucial particles in any condensed matter system defining its optoelectronic properties. Electron-phonon interaction plays very important role and casts phonons into physical consideration of carriers

in condensed matter systems. The strong electron-LO phonon interaction changes the carrier picture of just pure electron to polarons. Polaron states were introduced in Chaps. 3 and 5 and it was demonstrated that polarons gives rise to many interesting phenomena observed in the experiment such as finite carrier lifetime in SAQDs or band-narrowing and hopping transport in CQD supercrystals. Also, it was pointed out that anharmonicity of vibrational model may drive many effects via polaronic carriers such as relaxation of excited polaron in SAQDs or possible inhibition of hopping transport in CQD supercrystal.

Optical properties of SAQDs were studied in Chap. 4. The huge amount of spectroscopic data on the issue exists in the literature. The reason for that is possible application of SAQDs in novel intraband lasers. Such expectations are based on theoretical prediction that system with peaked density of states would perform better in lasing. However, peaked density of states means stronger confinement of carriers increasing the electron–phonon interaction and decreasing mobility of the carriers. Increased electron–phonon interaction leads to formation of polarons which coherence and lifetimes are greatly affected by lattice anharmonicity. These discoveries cast a doubt on QDs as possible active medium of intraband lasers. However, anharmonicity driven relaxation of polarons is newly proposed concept and additional modeling and intrinsic relations are needed in order to achieve satisfactory level of certainty in the theory. The main contribution in Chap. 4 is establishment of relationship between electron–phonon and electron–photon interaction in SAQDs. Such relationship when combined with proper theoretical description of non-radiative relaxation processes triggered by phonons gives the connection between readily measurable radiative and non-radiative lifetimes and opens new possibilities in testing the theoretical models explaining rela-

tively short carrier lifetimes observed in experiments. However, many effects such as thermal backfilling or problem of non-existing efficient extraction of carriers from lower lasing level are still present as the significant obstacles for intraband lasing in SAQDs. The future work should address this issue. Also, derived connection between electron-phonon and electron-photon coupling in quantum dots should be used in order to further experimentally test the accepted theory that non radiative transitions in quantum rods follow by anharmonicity driven polaron relaxation.

Transport properties of CQD supercrystals were studied in Chap. 5. Transport was considered within the tight-binding model with local electron-phonon interaction. Again, concept of polarons was introduced and its influence on the nature of transport demonstrated. Electron–phonon interaction creates polarons strongly bounded to quantum dots, i.e. stronger than pure electrons. This causes band narrowing and reduces the possibility of achievement of band-like transport in CQD supercrystals. If achieved, band-like transport could increase mobilities of carriers sufficiently in order to apply CQD supercrystal in optoelectronic devices such as photodetectors, solar cells or even FETs. Such situation could trigger strong technological advancements since technology of CQD fabrication stands as relatively cheap. The main contribution of this chapter is to build-up of accurate quantum mechanical approach in carrier transport which enables clear insight in the role of vibrations in the transport properties. Such an insight is very important because technology allows precise engineering of various parameters inside the CQD supercrystals. It can give prospectives and guidance to the scientists involved in fabrication of these structures. The model developed can be extended in order to study CQD supercrystals built of non-polar semiconductors such as silicon. Electron-phonon interaction is expected to

be much weaker due to absence of the polar type of coupling between optical phonons and electrons. However, for such case introduced generalized Marcus formula is not correct approach since the formation of small polarons does not occur easily as in the polar CQD supercrystals. Therefore, accurate formalism should be developed for such structures. It is expected that small polarons would not form that easily due to much weaker electron-phonon interaction and that bandlike transport is more likely to occur.

Bibliography

[1] Li, L. *et al.* Controlling the aspect ratio of quantum dots: From columnar dots to quantum dots. *IEEE J. Sel. Top. Quant.* **14**, 1204–1213 (2008).

[2] Talapin, D. V., Lee, J.-S., Kovalenko, M. V. & Shevchenko, E. V. Prospects of colloidal nanocrystals for electronic and optoelectronic applications. *Chem. Rev.* **110**, 389–458 (2010).

[3] Prodanović, N., Milanović, V., Ikonić, Z., Indjin, D. & Harrison, P. Bound states in continuum: Quantum dots in a quantum well. *Phys. Lett. A* **377**, 2177 – 2181 (2013).

[4] Prodanović, N., Vukmirović, N., Indjin, D., Ikonić, Z. & Harrison, P. Electronic states and intraband terahertz optical transitions in InGaAs quantum rods. *J. Appl. Phys.* **111**, 073110 (2012).

[5] Prodanović, N., Ikonić, Z., Indjin, D. & Harrison, P. Relationship between electron-LO phonon and electron-light interaction in quantum dots. *Phys. Rev. B* **85**, 195435 (2012).

[6] Lee, J.-S., Kovalenko, M. V., Huang, J., Chung, D. S. & Talapin, D. V. Band-like transport, high electron mobility and high photoconductivity in all-inorganic nanocrystal arrays. *Nat. Nanotechnol.* **6**, 348 (2011).

[7] Choi, J.-H. *et al.* Bandlike transport in strongly coupled and doped quantum dot solids: A route to high-performance thin-film electronics. *Nano Lett.* **12**, 2631–2638 (2012).

[8] Stangl, J., Holý, V. & Bauer, G. Structural properties of self-organized semiconductor nanostructures. *Rev. Mod. Phys.* **76**, 725–783 (2004).

[9] Petroff, P. M. & DenBaars, S. P. MBE and MOCVD growth and properties of self-assembling quantum dot arrays in III-V semiconductor structures. *Synth. Met.* **15**, 15–21 (1994).

[10] Bimberg, D., Grundmann, M. & Ledentsov, N. N. *Quantum dot heterostructures* (John Wiley, Chichester, 1990).

[11] Alivisatos, A. P. Semiconductor clusters, nanocrystals, and quantum dots. *Science* **271**, 933–938 (1996).

[12] Leite, E. R. & Ribeiro, C. *Crystallization and Growth of Colloidal Nanocrystals* (Springer Briefs in Materials, 2011).

[13] Reimann, S. M. & Manninen, M. Electronic structure of quantum dots. *Rev. Mod. Phys.* **74**, 1283–1342 (2002).

[14] van der Wiel, W. G. *et al.* Electron transport through double quantum dots. *Rev. Mod. Phys.* **75**, 1–22 (2003).

[15] Loss, D. & DiVincenzo, D. P. Quantum computation with quantum dots. *Phys. Rev. A* **57**, 120–126 (1998).

[16] Koppens, F. H. L. *et al.* Driven coherent oscillations of a single electron spin in a quantum dot. *Nat.* **442**, 766–771 (2006).

[17] Petta, J. R. *et al.* Coherent manipulation of coupled electron spins in semiconductor quantum dots. *Science* **309**, 2180–2184 (2005).

[18] Fafard, S. *et al.* Manipulating the energy levels of semiconductor quantum dots. *Phys. Rev. B* **59**, 15368–15373 (1999).

[19] Fafard, S. & Allen, C. N. Intermixing in quantum-dot ensembles with sharp adjustable shells. *Appl. Phys. Lett.* **75**, 2374–2376 (1999).

[20] Zibik, E. A. *et al.* Effects of alloy intermixing on the lateral confinement potential in InAs/GaAs self-assembled quantum dots probed by intersublevel absorption spectroscopy. *Appl. Phys. Lett.* **90**, 163107 (2007).

[21] He, J. *et al.* Growth, structural, and optical properties of self-assembled (In,Ga)As quantum posts on gaas. *Nano Lett.* **7**, 802–806 (2007).

[22] Motyka, M. *et al.* Optical and electronic properties of GaAs-based structures with columnar quantum dots. *Appl. Phys. Lett.* **90**, 181933 (2007).

[23] Li, L. H., Patriarche, G., Linfield, E. H., Khanna, S. P. & Davies, A. G. Effects of using As_2 and As_4 on the optical properties of InGaAs quantum rods grown by molecular beam epitaxy. *J. Appl. Phys.* **108**, 103522 (2010).

[24] Nedzinskas, R. *et al.* Photoreflectance and photoluminescence studies of epitaxial InGaAs quantum rods grown with As_2 and As_4 sources. *J. Appl. Phys.* **109**, 123526 (2011).

[25] Lorke, A., Luyken, R. J., Garcia, J. M. & Petroff, P. M. Growth and electronic properties of self-organized quantum rings. *Jap. J. Appl. Phys.* **40**, 1857–1859 (2001).

[26] Granados, D. & García, J. M. In(Ga)As self-assembled quantum ring formation by molecular beam epitaxy. *Appl. Phys. Lett.* **82**, 2401–2403 (2003).

[27] Bhowmick, S. *et al.* High-performance quantum ring detector for the 1–3 terahertz range. *Appl. Phys. Lett.* **96**, 231103 (2010).

[28] García, J. M., Mankad, T., Holtz, P. O., Wellman, P. J. & Petroff, P. M. Electronic states tuning of InAs self-assembled quantum dots. *Appl. Phys. Lett.* **72**, 3172–3174 (1998).

[29] Peng, X., Schlamp, M. C., Kadavanich, A. V. & Alivisatos, A. P. Epitaxial growth of highly luminescent CdSe/CdS core/shell nanocrystals with photostability and electronic accessibility. *J. Am. Chem. Soc.* **119**, 7019–7029 (1997).

[30] Murray, C. B., Kagan, C. R. & Bawendi, M. G. Self-organization of CdSe nanocrystallites into three-dimensional quantum dot superlattices. *Science* **270**, 1335–1338 (1995).

[31] Roest, A. L., Kelly, J. J. & Vanmaekelbergh, D. Coulomb blockade of electron transport in a ZnO quantum-dot solid. *Appl. Phys. Lett.* **83**, 5530–5532 (2003).

[32] Guyot-Sionnest, P. Electrical transport in colloidal quantum dot films. *J. Phys. Chem. Lett.* **3**, 1169–1175 (2012).

[33] Verzelen, O., Ferreira, R. & Bastard, G. Polaron lifetime and energy relaxation in semiconductor quantum dots. *Phys. Rev. B* **62**, R4809–R4812 (2000).

[34] Ferreira, R. *et al.* Decoherence effects in the intraband and interband optical transitions in InAs/GaAs quantum dots. *J. Appl. Phys.* **105**, 122412 (2009).

[35] Kouwenhoven, L. P., Austing, D. G. & Tarucha, S. Few-electron quantum dots. *Rep. Prog. Phys.* **64**, 701–736 (2001).

[36] Reithmaier, J. P. *et al.* Strong coupling in a single quantum dot-semiconductor microcavity. *Nat.* **432**, 197–200 (2004).

[37] Zrenner, A. *et al.* Coherent properties of a two-level system based on a quantum-dot photodiode. *Nature* **418**, 612–614 (2002).

[38] Ledentsov, N. N. *et al.* Quantum-dot heterostructure lasers. *IEEE J. Sel. Top. Quant.* **6**, 439–451 (2000).

[39] Bimberg, D. & Ledentsov, N. Quantum dots: lasers and amplifiers. *J. Phys.: Condens. Matter* **15**, 1063–1076 (2003).

[40] Arakawa, Y. & Sakaki, H. Multidimensional quantum well laser and temperature dependence of its threshold current. *Appl. Phys. Lett.* **40**, 939–941 (1982).

[41] Asada, M., Miyamoto, Y. & Suematsu, Y. Gain and the threshold of three-dimensional quantum-box lasers. *IEEE J. Quantum. Elect.* **22**, 1915–1921 (1986).

[42] Wade, A. *et al.* Magnetic-field-assisted terahertz quantum cascade laser operating up to 225 K. *Nat. Photonics* **3**, 41–45 (2009).

[43] Kirstaedter, N. *et al.* Low-threshold, large T_0 injection-laser emission from (InGa)As quantum dots. *Electron. Lett.* **30**, 1416–1417 (1994).

[44] Bhattacharya, P., Ghosh, S. & Stiff-Roberts, A. D. Quantum dot opto-electronic devices. *Ann Rev. Mat. Res.* **34**, 1–40 (2004).

[45] Santori, C., Pelton, M., Solomon, G. S., Dale, Y. & Yamamoto, Y. Triggered single photons from a quantum dot. *Phys. Rev. Lett.* **86**, 1502–1505 (2001).

[46] Harrison, P. *Quantum Wells, Wires and Dots, 2nd edition* (John Wiley and Sons Ltd., Chichester, England, 2005).

[47] Davies, J. H. *The Physics of Low-Dimensional Semiconductors* (Cambridge University Press, 1998).

[48] ed., R. P. *Intersubband Transitions In Quantum Structures* (McGraw-Hill Professional, 2006).

[49] Gmachl, C., Capasso, F., Sivco, D. L. & Cho, A. Y. Recent progress in quantum cascade lasers and applications. *Rep. Prog. Phys.* **64**, 1533–1601 (2001).

[50] Pickwell, E. & Wallace, V. P. Biomedical applications of terahertz technology. *J. Phys. D-Appl. Phys.* **39**, 301–310 (2006).

[51] Pan, D. *et al.* Normal incident infrared absorption from InGaAs/GaAs quantum dot superlattice. *Electron. Lett.* **32**, 1726–1727 (1996).

[52] Faist, J. *Quantum Cascade Lasers* (Oxford University Press, USA, 2013).

[53] Scalari, G. *et al.* Terahertz Emission from Quantum Cascade Lasers in the Quantum Hall Regime: Evidence for Many Body Resonances and Localization Effects. *Phys. Rev. Lett.* **93**, 237403 (2004).

[54] Bockelman, U. & Bastard, G. Phonon scattering and energy relaxation in two-, one-, and zero-dimensional electron gases. *Phys. Rev. B* **42**, 8947–8951 (1990).

[55] Sauvage, S. *et al.* Long Polaron Lifetime in InAs/GaAs Self-Assembled Quantum Dots. *Phys. Rev. Lett.* **88**, 177402 (2002).

[56] Zibik, E. A. *et al.* Intraband relaxation via polaron decay in InAs self-assembled quantum dots. *Phys. Rev. B* **70**, 161305 (2004).

[57] Hameau, S. *et al.* Strong electron-phonon coupling regime in quantum dots: Evidence for everlasting resonant polarons. *Phys. Rev. Lett.* **83**, 4152–4155 (1999).

[58] Hameau, S. *et al.* Far-infrared magnetospectroscopy of polaron states in self-assembled InAs/GaAs quantum dots. *Phys. Rev. B* **65**, 085316–085319 (2002).

[59] Vukmirović, N., Ikonić, Z., Indjin, D. & Harrison, P. Quantum transport in semiconductor quantum dot superlattices: Electron-phonon resonances and polaron effects. *Phys. Rev. B* **76**, 245313 (2007).

[60] Stauber, T., Zimmermann, R. & Castella, H. Electron-phonon interaction in quantum dots: A solvable model. *Phys. Rev. B* **62**, 7336–7343 (2000).

[61] Zibik, E. A. *et al.* Long lifetimes of quantum-dot intersublevel transitions in the terahertz range. *Nat. Mater.* **8**, 803–807 (2009).

[62] Li, X.-Q., Nakayama, H. & Arakawa, Y. Phonon bottleneck in quantum dots: Role of lifetime of the confined optical phonons. *Phys. Rev. B* **59**, 5069–5073 (1999).

[63] Urayama, J., Norris, T. B., Singh, J. & Bhattacharya, P. Observation of Phonon Bottleneck in Quantum Dot Electronic Relaxation. *Phys. Rev. Lett.* **86**, 4930–4933 (2001).

[64] Hsu, C.-F., O, J.-S., Zory, P. & Botez, D. Intersubband Quantum-Box Semiconductor Lasers. *IEEE J. Sel. Top. Quant.* **6**, 491–503 (2000).

[65] Hsu, C.-F., O, J.-S., Zory, P. & Botez, D. Intersubband quantum-box semiconductor lasers. *IEEE J. Sel. Top. Quant.* **6**, 491 –503 (2000).

[66] Apalkov, V. M. & Chakraborty, T. Luminescence spectra of a quantum-dot cascade laser. *Appl. Phys. Lett.* **78**, 1820–1822 (2001).

[67] Vukmirović, N., Indjin, D., Ikonić, Z. & Harrison, P. Electron transport and terahertz gain in quantum-dot cascades. *IEEE Photonic. Tech. L.* **20**, 129–131 (2008).

[68] Dmitriev, I. A. & Suris, R. A. Quantum cascade lasers based on quantum dot superlattice. *phys. stat. sol. (a)* **202**, 987–991 (2005).

[69] Ulbrich, N. *et al.* Midinfrared intraband electroluminescence from AlInAs quantum dots. *Appl. Phys. Lett.* **83**, 1530–1532 (2003).

[70] Anders, S. *et al.* Electroluminescence of a quantum dot cascade structure. *Appl. Phys. Lett.* **82**, 3862–3864 (2003).

[71] Fischer, C., Bhattacharya, P. & Yu, P.-C. Intersublevel electroluminescence from In0.4Ga0.6As/GaAs quantum dots in quantum cascade heterostructure with GaAsN/GaAs superlattice. *Electron. Lett.* **39**, 1537 – 1538 (2003).

[72] Fischer, C. H., Bhattacharya, P. & YU, P. C. Intersublevel electroluminescence from $In_{0.4}Ga_{0.6}As$/GaAs quantum dots in quantum cascade heterostructure with GaAsN/GaAs superlattice. *Electron. Lett.* **39**, 1537–1538 (2003).

[73] Wasserman, D., Ribaudo, T., Lyon, S. A., Lyo, S. K. & Shaner, E. A. Room temperature midinfrared electroluminescence from InAs quantum dots. *Appl. Phys. Lett.* **94**, 061101 (2009).

[74] Kershaw, S. V., M., H., Rogach, A. L. & A., K. Development of IR-emitting colloidal IIVI quantum-dot materials. *IEEE J. Sel. Top. Quant.* **6**, 534 (2000).

[75] Colvin, V. L., Schlamp, M. C. & Alivisatos, A. P. Light-emitting diodes made from cadmium selenide nanocrystals and a semiconducting polymer. *Nat.* **370**, 354 (1994).

[76] Caruge, J.-M., Halpert, J. E., Bulović, V. & Bawendi, M. G. NiO as an inorganic hole-transporting layer in quantum-dot light-emitting devices. *Nano Lett.* **6**, 2991–2994 (2006). PMID: 17163746, http://pubs.acs.org/doi/pdf/10.1021/nl0623208.

[77] Sargent, E. H. Solar cells, photodetectors, and optical sources from infrared colloidal quantum dots. *Adv. Mater.* **20**, 3958–3964 (2008).

[78] Sargent, E. H. Infrared photovoltaics made by solution processing. *Nat. Photonics* **3**, 329 (2009).

[79] Beard, M. & Ellingson, R. Multiple exciton generation in semiconductor nanocrystals: Toward efficient solar energy conversion. *Las. Photonic. Rev.* **2**, 377–399 (2008).

[80] Boer, E. A. *et al.* Charging of single Si nanocrystals by atomic force microscopy. *Appl. Phys. Lett.* **78**, 3133–3135 (2001).

[81] Kim, H., Cho, K., Kim, D.-W., Lee, H.-R. & Kim, S. Bottom- and top-gate field-effect thin-film transistors with p channels of sintered HgTe nanocrystals. *Appl. Phys. Lett.* **89**, – (2006).

[82] Talapin, D. V. & Murray, C. B. PbSe nanocrystal solids for n- and p-channel thin film field-effect transistors. *Science* **310**, 86–89 (2005).

[83] Yu, D., Wang, C., Wehrenberg, B. L. & Guyot-Sionnest, P. Variable range hopping conduction in semiconductor nanocrystal solids. *Phys. Rev. Lett.* **92**, 216802 (2004).

[84] Mott, N. F. & Davis, E. A. *Electronic Processes in Non-Crystalline Materials, 2nd ed.* (Clarendon Press (Oxford), 1979).

[85] Skinner, B., Chen, T. & Shklovskii, B. I. Theory of hopping conduction in arrays of doped semiconductor nanocrystals. *Phys. Rev. B* **85**, 205316 (2012).

[86] Talgorn, E. *et al.* Unity quantum yield of photogenerated charges and band-like transport in quantum-dot solids. *Nat. Nanotechnol.* **6**, 733 (2011).

[87] Stier, O., Grundmann, M. & Bimberg, D. Electronic and optical properties of strained quantum dots modeled by 8-band $k \cdot p$ theory. *Phys. Rev. B* **59**, 5688–5701 (1999).

[88] Jiang, H. & Singh, J. Strain distribution and electronic spectra of InAs/GaAs self-assembled dots: An eight-band study. *Phys. Rev. B* **56**, 4696–4701 (1997).

[89] Pryor, C. Eight-band calculations of strained InAs/GaAs quantum dots compared with one-, four-, and six-band approximations. *Phys. Rev. B* **57**, 7190–7195 (1998).

[90] Bahder, T. B. Eight-band $k \cdot p$ model of strained zinc-blende crystals. *Phys. Rev. B* **41**, 11992–12001 (1990).

[91] Tomić, S., Sunderland, A. G. & Bush, I. J. Parallel multi-band $k \cdot p$ code for electronic structure of zinc blend semiconductor quantum dots. *J. Mater. Chem.* **16**, 1963–1972 (2006).

[92] Lepage, H., Kaminski-Cachopo, A., Poncet, A. & le Carval, G. Simulation of electronic transport in silicon nanocrystal solids. *J. Phys. Chem. C* **116**, 10873–10880 (2012).

[93] Vukmirović, N. *Physics of Intraband Quantum Dot Optoelectronic Devices*. Ph.D. thesis, University of Leeds, UK (2007).

[94] Voon, L. Y., Car, L. & Willatzen, M. *The $\boldsymbol{k} \cdot \boldsymbol{p}$ Method* (Springer, 2009).

[95] Burt, M. G. The justification for applying the effective-mass approximation to microstructures. *J. Phys.: Condens. Matter* **4**, 6651–6690 (1992).

[96] Jogai, B. Three-dimensional strain field calculations in coupled InAs/GaAs quantum dots. *J. Appl. Phys.* **88**, 5050–5055 (2000).

[97] Bir, G. L. & Pikus, G. E. *Symmetry and Strain-Induced Effects in Semiconductors* (John Wiley & Sons, 1974).

[98] Löwdin, P. O. A note on the quantum-mechanical perturbation theory. *J. Chem. Phys.* **19**, 1396–1401 (1951).

[99] Nedzinskas, R. *et al.* Electronic structure and optical anisotropy of InGaAs quantum rods studied by photoreflectance and photoluminescence. *phys. stat. sol. (c)* **9**, 1640–1642 (2012).

[100] Stehr, D. *et al.* Ultrafast carrier capture in InGaAs quantum posts. *Appl. Phys. Lett.* **95**, 251105 (2009).

[101] Morris, C. M. *et al.* Terahertz ionization of highly charged quantum posts in a perforated electron gas. *Nano Lett.* **12**, 1115–1120 (2012).

[102] Saito, T., Ebe, H., Arakawa, Y., Kakitsuka, T. & Sugawara, M. Optical polarization in columnar InAs/GaAs quantum dots: 8-band $k \cdot p$ calculations. *Phys. Rev. B* **77**, 195318 (2008).

[103] Andrzejewski, J., Sęk, G., O'Reilly, E., Fiore, A. & Misiewicz, J. Design of columnar quantum dots for polarization-independent emission using 8–band kp method. *J. Phys. Chem. Solids* **245**, 012038 (2010).

[104] J, D. A. *The Finite Element Method* (Clarendon Press, Oxford, 1980).

[105] Vukmirović, N. *et al.* Intraband absorption in InAs/GaAs quantum dot infrared photodetectors - effective mass versus $k \cdot p$ modelling. *Semicond. Sci. Technol.* **21**, 1098–1104 (2006).

[106] Vukmirović, N., Indjin, D., Ikonić, Z. & Harrison, P. Origin of detection wavelength tuning in quantum dots-in-a-well infrared photodetectors. *Appl. Phys. Lett.* **88**, 251107 (2006).

[107] von Neumann, J. & Wigner, E. *Phys. Z.* **30**, 465 (1929).

[108] Stillinger, F. H. & Herrick, D. R. Bound states in the continuum. *Phys. Rev. A* **11**, 446–454 (1975).

[109] Capasso, F. *et al.* Observation of an electronic bound state above a potential well. *Nat.* **358**, 565 (1992).

[110] Cederbaum, L. S., Friedman, R. S., Ryaboy, V. M. & Moiseyev, N. Conical intersections and bound molecular states embedded in the continuum. *Phys. Rev. Lett.* **90**, 013001 (2003).

[111] Nakamura, H., Hatano, N., Garmon, S. & Petrosky, T. Quasibound states in the continuum in a two channel quantum wire with an adatom. *Phys. Rev. Lett.* **99**, 210404 (2007).

[112] Moiseyev, N. Suppression of Feshbach resonance widths in two-dimensional waveguides and quantum dots: A lower bound for the number of bound states in the continuum. *Phys. Rev. Lett.* **102**, 167404 (2009).

[113] Petrović, J. S., Milanović, V. & Ikonić, Z. Bound states in continuum of complex potentials generated by supersymmetric quantum mechanics. *Phys. Lett. A* **300**, 595 – 602 (2002).

[114] Sadreev, A. F., Bulgakov, E. N. & Rotter, I. Bound states in the continuum in open quantum billiards with a variable shape. *Phys. Rev. B* **73**, 235342 (2006).

[115] Molina, M. I., Miroshnichenko, A. E. & Kivshar, Y. S. Surface bound states in the continuum. *Phys. Rev. Lett.* **108**, 070401 (2012).

[116] Hsueh, W., Chen, C. & Chang, C. Bound states in the continuum in quasiperiodic systems. *Phys. Lett. A* **374**, 4804 – 4807 (2010).

[117] Marinica, D. C., Borisov, A. G. & Shabanov, S. V. Bound states in the continuum in photonics. *Phys. Rev. Lett.* **100**, 183902 (2008).

[118] Plotnik, Y. *et al.* Experimental observation of optical bound states in the continuum. *Phys. Rev. Lett.* **107**, 183901 (2011).

[119] Prodanović, N., Milanović, V. & Radovanović, J. Photonic crystals with bound states in continuum and their realization by an advanced digital grading method. *J. Phys. A-Math. Gen.* **42**, 415304 (2009).

[120] Robnik, M. A simple separable Hamitlonian having bound-states in the continuum. *J. Phys. A-Math. Gen.* **19**, 3845–3848 (1986).

[121] Ashcroft, N. W. & Mermin, N. D. *Solid State Physics* (Saunders College Publishing, 1976).

[122] Mahan, G. *Many-Particle Physics* (Kluwer Academic, 2000).

[123] Stroscio, M. A. *Phonons in Nanostructures* (Cambridge University Press, 2004).

[124] Takagahara, T. Electron-phonon interactions in semiconductor nanocrystals. *J. Lumines.* **70**, 129–143 (1996).

[125] Inoshita, T. & Sakaki, H. Density of states and phonon-induced relaxation of electrons in semiconductor quantum dots. *Phys. Rev. B* **56**, R4355–R4358 (1997).

[126] Stauber, T. & Zimmermann, R. Optical absorption in quantum dots: Coupling to longitudinal optical phonons treated exactly. *Phys. Rev. B* **73**, 115303 (2006).

[127] Klemens, P. G. Anharmonic decay of optical phonons. *Phys. Rev.* **148**, 845–848 (1966).

[128] Usher, S. & Srivastava, G. P. Theoretical study of the anharmonic decay of nonequilibrium LO phonons in semiconductor structures. *Phys. Rev. B* **50**, 14179–14186 (1994).

[129] Barman, S. & Srivastava, G. P. Long-wavelength nonequilibrium optical phonon dynamics in cubic and hexagonal semiconductors. *Phys. Rev. B* **69**, 235208 (2004).

[130] Vallée, F. & Bogani, F. Coherent time-resolved investigation of LO-phonon dynamics in GaAs. *Phys. Rev. B* **43**, 12049–12052 (1991).

[131] Ridley, B. K. The LO phonon lifetime in GaN. *J. Phys.: Condens. Matter* **8**, L511 (1996).

[132] Srivastava, G. P. *The Physics of Phonons* (Hilger, Bristol, 1999).

[133] Grange, T., Ferreira, R. & Bastard, G. Polaron relaxation in self-assembled quantum dots: Breakdown of the semiclassical model. *Phys. Rev. B* **76**, 241304 (2007).

[134] Jackson, J. D. *Classical Electrodynamics* (John Wiley & Sons, 1999).

[135] Wendler, L. Electronphonon interaction in dielectric bilayer systems. effect of the electronic polarizability. *phys. stat. sol. (b)* **129**, 513–530 (1985).

[136] Klein, M. C., Hache, F., Ricard, D. & Flytzanis, C. Size dependence of electron-phonon coupling in semiconductor nanospheres: The case of CdSe. *Phys. Rev. B* **42**, 11123–11132 (1990).

[137] Licari, J. J. & Evrard, R. Electron-phonon interaction in a dielectric slab: Effect of the electronic polarizability. *Phys. Rev. B* **15**, 2254–2264 (1977).

[138] Mori, N. & Ando, T. Electron ˘ optical-phonon interaction in single and double heterostructures. *Phys. Rev. B* **40**, 6175–6188 (1989).

[139] Rickaysen, G. *Green's Functions and Condensed Matter* (Academic Press Limited, London, 1980).

[140] Besombes, L., Kheng, K., Marsal, L. & Mariette, H. Acoustic phonon broadening mechanism in single quantum dot emission. *Phys. Rev. B* **63**, 155307 (2001).

[141] Borri, P. *et al.* Ultralong dephasing time in InGaAs quantum dots. *Phys. Rev. Lett.* **87**, 157401 (2001).

[142] Uskov, A. V., Jauho, A.-P., Tromborg, B., Mørk, J. & Lang, R. Dephasing times in quantum dots due to elastic lo phonon-carrier collisions. *Phys. Rev. Lett.* **85**, 1516–1519 (2000).

[143] Muljarov, E. A. & Zimmermann, R. Dephasing in quantum dots: Quadratic coupling to acoustic phonons. *Phys. Rev. Lett.* **93**, 237401 (2004).

[144] Muljarov, E. A., Takagahara, T. & Zimmermann, R. Phonon-induced exciton dephasing in quantum dot molecules. *Phys. Rev. Lett.* **95**, 177405 (2005).

[145] Muljarov, E. A. & Zimmermann, R. Exciton dephasing in quantum dots due to lo-phonon coupling: An exactly solvable model. *Phys. Rev. Lett.* **98**, 187401 (2007).

[146] Machnikowski, P. Change of decoherence scenario and appearance of localization due to reservoir anharmonicity. *Phys. Rev. Lett.* **96**, 140405 (2006).

[147] Takagahara, T. Theory of exciton dephasing in semiconductor quantum dots. *Phys. Rev. B* **60**, 2638–2652 (1999).

[148] Zibik, E. A. *et al.* Intersublevel polaron dephasing in self-assembled quantum dots. *Phys. Rev. B* **77**, 041307 (2008).

[149] Herbut, F. *Quantum Mechanics (in Serbian)* (University of Belgrade, 1980).

[150] Tomić, S. Intermediate-band solar cells: Influence of band formation on dynamical processes in InAs/GaAs quantum dot arrays. *Phys. Rev. B* **82**, 195321 (2010).

[151] Lamb, W. E., Schlicher, R. R. & Scully, M. O. Matter-field interaction in atomic physics and quantum optics. *Phys. Rev. A* **36**, 2763–2772 (1987).

[152] Chandler, R. E., Houtepen, A. J., Nelson, J. & Vanmaekelbergh, D. Electron transport in quantum dot solids: Monte Carlo simulations of the effects of shell filling, Coulomb repulsions, and site disorder. *Phys. Rev. B* **75**, 085325 (2007).

[153] Ikonić, Z. & Milanović, V. *Semiconductor Quantum Microstructures (in Serbian)* (University of Belgrade, 1997).

[154] van de Lagemaat, J. Einstein relation for electron diffusion on arrays of weakly coupled quantum dots. *Phys. Rev. B* **72**, 235319 (2005).

[155] Chu, I.-H., Radulaski, M., Vukmirović, N., Cheng, H.-P. & Wang, L.-W. Charge transport in a quantum dot supercrystal. *J. Phys. Chem. C* **115**, 21409–21415 (2011).

[156] Liu, Y. *et al.* Dependence of carrier mobility on nanocrystal size and ligand length in PbSe nanocrystal solids. *Nano Lett.* **10**, 1960–1969 (2010).

[157] Fafarman, A. T. *et al.* Thiocyanate-capped nanocrystal colloids: Vibrational reporter of surface chemistry and solution-based route to enhanced coupling in nanocrystal solids. *J. Am. Chem. Soc.* **133**, 15753–15761 (2011).

[158] Kovalenko, M. V., Scheele, M. & Talapin, D. V. Colloidal nanocrystals with molecular metal chalcogenide surface ligands. *Science* **324**, 1417–1420 (2009).

[159] Tang, J. *et al.* Colloidal-quantum-dot photovoltaics using atomic-ligand passivation. *Nat. Mater.* **10**, 765 (2011).

[160] Cheng, Y.-C. & Silbey, R. J. A unified theory for charge-carrier transport in organic crystals. *J. Chem. Phys.* **128**, 114713 (2008).

[161] Yarkoni, D. R. & Silbey, R. J. Variational approach to exciton transport in molecular crystals. *J. Chem. Phys.* **67**, 5818 (1977).

[162] Lin, S. H. *et al.* Ultrafast dynamics and spectroscopy of bacterial photosynthetic reaction centers. *Adv. Chem. Phys.* **121**, 1 (2002).

[163] Nan, G., Yang, X., Wang, L., Shuai, Z. & Zhao, Y. Nuclear tunneling effects of charge transport in rubrene, tetracene, and pentacene. *Phys. Rev. B* **79**, 115203 (2009).

[164] Kang, M. S., Sahu, A., Norris, D. J. & Frisbie, C. D. Size-dependent electrical transport in CdSe nanocrystal thin films. *Nano Lett.* **10**, 3727–3732 (2010).